

EFFECT OF HUMPS ON THE STABILITY OF BOUNDARY LAYERS OVER AN AIRFOIL

by

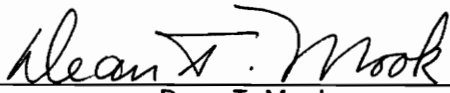
Hasan T. Abu Khajeel

Thesis submitted to the Faculty of the
Virginia Polytechnic Institute and State University
in partial fulfillment of the requirements for the degree of
Master of Science
in
Engineering Mechanics

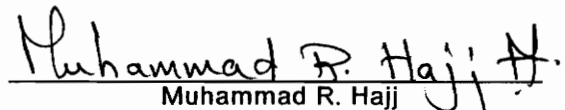
APPROVED:



Ali H. Nayfeh, Chairman



Dean T. Mook



Muhammad R. Hajj

May 1993

Blacksburg, Virginia

LD
S655
V855
1993

A'28

C.2

C.2

EFFECT OF HUMPS ON THE STABILITY OF BOUNDARY LAYERS OVER AN AIRFOIL

by

Hasan T. Abu Khajeel

Ali H. Nayfeh, Chairman

Engineering Mechanics

(ABSTRACT)

The effect of humps on the stability of subsonic boundary layers over an airfoil is investigated. The mean flow is calculated by using an interacting boundary-layer solver which accounts for strong viscous/inviscid interaction and separation bubbles. The code is capable of solving compressible as well as incompressible flows. Then, the two-dimensional mean flow is fed into a stability program which is capable of doing two-and three-dimensional analysis. The output of this stability program is the growth rates which are integrated along a prescribed path to yield the amplification factor (i.e., N-factor), which is used to predict transition from laminar to turbulent flow. The analysis is performed for different heights and locations of the hump and for different Mach numbers. The results show that compressibility stabilizes the flow and that the most dangerous frequency decreases as the Mach number increases for a fixed location of the hump. Also this most dangerous frequency decreases as the hump is moved downstream. Moreover, the amplification factor increases as the hump height increases and as the hump is moved downstream.

The influence of suction and heat-transfer strips on controlling the destabilizing influence of the hump is investigated. The results show that cooling and suction strips stabilize the flow and therefore delay transition from laminar to turbulent flow. Moreover, a heating strip destabilizes the flow in the presence of a hump. Applying suction through multiple strips can be as effective as continuous suction. Also the total flow rate required using multiple strips is less than that required using a single strip. We optimize the locations of these strips for a certain hump location. Moreover, cooling through multiple strips is as effective as cooling through a single strip. We optimize the locations and levels of these cooling strips for a certain hump location.

Acknowledgements

All gratitude is due to the Creator of this universe, All-Mighty Allah, for all that I have gained and accomplished in this life.

I would like to express my gratitude and my sincere appreciation to my advisor, Dr. Ali H. Nayfeh, for his teaching, guidance, continuous support, contributions, valuable advice, and patience throughout this work. Thanks are also due to my committee members: Drs. Dean T. Mook, Saad A. Ragab, and Muhammad R. Hajj for their encouragement and explanations. I am also grateful to Sally Shrader for her helping in typing the equations and making the corrections needed. I appreciate the companionship of my colleagues of the Nonlinear Mechanics Group, especially Dr. Marwan Bikdash.

I wish to express my warmest appreciation and gratitude to my parents, brothers, and sisters for their support, constant encouragement, and many sacrifices throughout my graduate school.

Finally, I would like to thank everyone whom I might have missed. This has been a fruitful experience in my life and if I had the option of doing it all over again I would not hesitate!

Table of Contents

1. Introduction 1

2. Problem Formulation 8

2.1 Boundary-Layer Formulation 9

2.2 Inviscid Flow 12

2.3 Viscosity 14

2.4 Initial Conditions 15

2.5 Levy-Lees Variables 15

2.6 Boundary-Layer Parameters 22

2.7 Interacting Law 23

2.8 Boundary Conditions 35

2.9 Stability Problem 39

3. Results and Discussion 44

3.1 Clean Airfoil 46

3.2 Influence of the Hump 47

 3.2.1 Mean-Flow Characteristics 47

 3.2.2 Stability Characteristics 48

3.2.2.1 Location L1	49
3.2.2.2 Location L2	50
3.2.2.3 Location L3	51
3.3 Boundary-Layer Control with Suction	51
3.4 Boundary-Layer Control with Heat Transfer	55
4. Conclusions and Recommendations	58
4.1 Conclusions	58
4.2 Recommendations	59
5. References	61
Tables and Figures	67

List of Illustrations

Figure 1.	EQH1260 airfoil	73
Figure 2.	Pressure distributions for the EQH1260 airfoil calculated by using an Euler code	74
Figure 3.	Shape of the considered cubic hump located at L3	75
Figure 4.	Variation of the N-factor with streamwise position for the clean airfoil when $M = 0.14$ for several frequencies	76
Figure 5.	Variation of the N-factor with streamwise position for the clean airfoil when $M = 0.50$ for several frequencies	77
Figure 6.	Variation of the N-factor with streamwise position for the clean airfoil when $M = 0.65$ for several frequencies	78
Figure 7.	Variation of the displacement thickness with streamwise position for the clean airfoil at three Mach numbers	79
Figure 8.	Variation of the skin-friction coefficient with streamwise position for humps # 3,4,5 located at L1 when $M = 0.14$	80
Figure 9.	Variation of the skin-friction coefficient with streamwise position for humps # 3,4,5 located at L1 when $M = 0.50$	81
Figure 10.	Variation of the skin-friction coefficient with streamwise position for humps # 3,4,5 located at L1 when $M = 0.65$	82
Figure 11.	Variation of the skin-friction coefficient with streamwise position for humps # 3,4,5 located at L2 when $M = 0.50$	83
Figure 12.	Variation of the skin-friction coefficient with streamwise position for humps # 3,4,5 located at L3 when $M = 0.50$	84
Figure 13.	Variation of the skin-friction coefficient with streamwise position for the clean airfoil and hump # 5 located at L1	85
Figure 14.	Variation of the N-factor for the most dangerous frequency with streamwise position for hump # 3 located at L1 and all three Mach numbers	86
Figure 15.	Variation of the N-factor for the most dangerous frequency with streamwise position for hump # 4 located at L1 and all three Mach numbers	87

Figure 16.	Variation of the N-factor for the most dangerous frequency with streamwise position for hump # 5 located at L1 and all three Mach numbers	88
Figure 17.	Variation of the N-factor for the most dangerous frequency with streamwise position when $M=0.14$ for seven heights at location L1	89
Figure 18.	Variation of the N-factor for the most dangerous frequency with streamwise position when $M=0.50$ for seven heights at location L1	90
Figure 19.	Variation of the N-factor for the most dangerous frequency with streamwise position when $M=0.65$ for six heights at location L1	91
Figure 20.	Variation of the N-factor for the most dangerous frequency with streamwise position for hump # 3 located at L2 and all three Mach numbers	92
Figure 21.	Variation of the N-factor for the most dangerous frequency with streamwise position for hump # 4 located at L2 and all three Mach numbers	93
Figure 22.	Variation of the N-factor for the most dangerous frequency with streamwise position for hump # 5 located at L2 and all three Mach numbers	94
Figure 23.	Variation of the N-factor for the most dangerous frequency with streamwise position for hump # 3 located at L3 and all three Mach numbers	95
Figure 24.	Variation of the N-factor for the most dangerous frequency with streamwise position for hump # 4 located at L3 and all three Mach numbers	96
Figure 25.	Variation of the N-factor for the most dangerous frequency with streamwise position for hump # 5 located at L3 and all three Mach numbers	97
Figure 26.	Variation of the N-factor with streamwise position for several frequencies with suction for hump # 5 located at L3 when $M = 0.14$	98
Figure 27.	Variation of the N-factor for the most dangerous frequency with streamwise position for three suction location when $M = 0.14$	99
Figure 28.	Influence of a suction strip on the variation of the N-factor for the most dangerous frequency with streamwise position for three suction levels when $M = 0.14$	100
Figure 29.	Variation of the N-factor for the most dangerous frequency with streamwise position for different locations of a suction strip of width 0.08	101
Figure 30.	Variation of the N-factor for the most dangerous frequency with streamwise position for two-suction-strip configurations and different suction levels	102
Figure 31.	Variation of the N-factor with streamwise position for several frequencies with cooling for hump # 5 located at L3 when $M = 0.14$	103
Figure 32.	Variation of the N-factor for the most dangerous frequency with streamwise position for three cooling-strip locations when $M = 0.14$	104
Figure 33.	Variation of the N-factor for the most dangerous frequency with streamwise position for three cooling levels when $M = 0.14$	105

Figure 34. Variation the of N-factor with streamwise position for the most dangerous frequency and five two-cooling-strip configurations	106
Figure 35. Variation of the N-factor for the most dangerous frequency with streamwise position for hump # 5 located at L3 and two heating strips	107

List of Tables

Table 1.	Variation of the most dangerous frequency with Mach number and hump location for all considered humps	68
Table 2.	Transition location (i.e., $N = 9$) for different hump heights and different Mach numbers at location L1	69
Table 3.	Transition location (i.e., $N = 9$) for different hump heights and different Mach numbers at location L2	70
Table 4.	Transition location (i.e., $N = 9$) for different hump heights and different Mach numbers at location L3	71

1. Introduction

The design of laminar-flow wings involves the control of disturbances within the boundary layer in order to delay transition to a location significantly downstream on the chord with a minimum compromise of the other factors that affect the aerodynamic or structural efficiency of the wing. Significant chordwise extents of laminar flow can be achieved by the selection of a wing shape that yields the proper pressure distribution with the minimum value being as close as possible to the trailing edge, because transition occurs before or at the location of minimum pressure. Therefore, recent progress in aerodynamics research has led to the design of airfoils and bodies with considerable extents of laminar boundary-layer flow. Passive methods have been proposed for stabilizing the laminar flow. They include application of suction and/or heating or cooling through the surface. The suction and heating can be continuous or through discrete strips.

Granting that extensive laminar flow can actually be attained, however, the first requisite is that the surface should be extremely smooth as not to disturb the stability of the boundary layer. Even a small degree of surface roughness may produce premature transition to turbulent flow. Generally speaking, the presence of roughness favors transition in the sense that, under otherwise identical conditions, transition occurs at a lower Reynolds number on a rough wall than on a smooth wall. The presence of a roughness element gives rise to

additional disturbances in the laminar stream which must be added to those generated by the turbulence already present in the boundary layer.

The preceding considerations show complete agreement with experiments. When the roughness elements are very large, transition will occur at the location of the roughness. Earlier papers, namely those by Schiller [1], Tani, Hama, and Mituisi [2], Goldstein [3], and Fage and Preston [4], assumed that the point of transition is located at the positions of roughness elements when they are large, or that their presence has no influence at all when they are small. However, the empirical correlations of Fage [26] has shown that the point of transition moves continuously upstream as the height of the roughness element is increased until it ultimately reaches the position of the roughness element. These results are confirmed by the theoretical calculations of Masad and Nayfeh [47]. It is therefore of great importance to provide an approximate estimate of the maximum degree of surface roughness that can be tolerated without affecting transition.

The air flow over conventional aircraft wings is turbulent almost from the leading edge. By reshaping the wing and increasing the smoothness of its surface, the air flows uniformly along the wing skin without turbulence. Such a laminar flow could reduce the total drag of the aircraft by as much as 15%. This implies a saving in fuel consumption, which translates into a 2 to 3% decrease in Direct Operating Costs (DOC) [5]. The dramatic reduction in fuel consumption means a comparable cut-back in pollutive emissions and the environmental impact of air transportation.

The performance of Natural Laminar Flow (NLF) airfoils is strongly dependent on the location of transition, which may be strongly influenced by surface imperfections. Although modern technology can provide smooth surfaces that are suitable for Laminar Flow Control (LFC) and NLF, manufacturing tolerance criteria are needed for other unavoidable surface imperfections. These imperfections are in the forms of waviness and bulges, steps and gaps at junctions, and three-dimensional roughness elements, such as flush head slots and incorrectly installed flush rivets [6-9]. Other kinds of roughness elements include dust particles, snow, and drizzle rain. Other unavoidable discontinuities arise from the installation

of leading-edge panels on wings, nacelles, and empennage surfaces and the installation of access panels, doors, and windows on fuselage noses and engine nacelles [6-9]. Since discontinuities cannot be avoided, a manufacturing guide is needed for their tolerances so that laminar flow can be maintained. The mechanisms by which these imperfections cause transition include laminar separation (hence shear-layer instability), amplification of Tollmien-Schlichting waves, amplification of cross-flow vorticity, Görtler instability, and interaction between two or more of these mechanisms [10-22].

Walker and Greening [23] performed wind-tunnel experiments to determine the effect of two-dimensional smooth bulges and hollows on the transition of the flow over a flat plate. They used surface tubes to determine the location of transition from laminar to turbulent flow. Their bulges and hollows were mounted on one side of a smooth flat aluminum plate having an elliptic leading edge. Hislop [24] carried out similar experiments for narrow spanwise surface ridge corrugations on a flat plate. Walker and Cox [25] performed wind-tunnel experiments to study the effect of spanwise corrugations on an airfoil. These experiments were made for three forms of narrow corrugations (flat, arch, and wire) situated in the laminar boundary layer of a large symmetric airfoil (EQH1260 section) mounted at a zero angle of attack.

Fage [26] collected the three previous works [23-25] and established criteria for the critical heights of these imperfections that cause transition from laminar to turbulent flow. He found that the flow conditions near a corrugation that affect transition are associated with a separation of the laminar boundary layer from its surface. The criteria of Fage for steps and gaps did not include the effects of the shapes of these imperfections. However, the flight experiments of Holmes, Obara, Martin, and Domack [8] demonstrate the strong influence of the shapes of steps on the transition location and hence on the allowable heights of such imperfections. They found out that by rounding a forward-facing step, the critical Reynolds number increases from 1800 to 2700.

Carmichael, Whites, and Pfenninger [27], Carmichael and Pfenninger [28], and Carmichael [29] performed flight experiments on the wing glove of an F-94A airplane. The

modified 652-213 airfoil had 69 suction slots distributed between 41% and 95% chord. They investigated single and multiple sinusoidal waves located at 15%, 28%, and 64% chord. Their results show that the allowable sizes of the waves increase when embedded in the suction region. They found that maintaining laminar flow across the airfoil requires an 8% increase in the suction level over the clear airfoil case. Carmichael [29] established criteria for allowable single and multiple bulges or sinusoidal waviness for both swept and unswept wing surfaces using the results of these experiments, which partially include the influence of compressibility, suction, pressure gradients, multiple imperfections, and wing sweep. Carmichael's criteria are based on experimental results for waves located more than 25% chord downstream of the leading edge and hence they will underpredict allowable imperfections in the leading edge region and overpredict allowable imperfections in regions of unaccelerated flows.

These empirically based criteria are for special cases and geometries, and they do not explain the instability mechanisms enhanced by the imperfections or the physics of ways to control them. To determine the mechanism by which two-dimensional roughness elements induce boundary-layer transition, Klebanoff and Tidstrom [30] carried out an experiment using cylindrical rods attached to the surface of a flat plate. They placed primary emphasis on the nature of disturbances within the recovery zone; that is, the region immediately downstream of the rods where the mean flow was distorted by their presence. They made detailed measurements of the mean-velocity distributions, disturbance spectra, growth, and decay of disturbances at discrete frequencies for a range of Reynolds numbers. They concluded that "the basic mechanism by which a two-dimensional roughness element induces earlier transition is by the destabilizing effect of the flow in the recovery zone on existing disturbances which hasten the downstream development of the instability." Dovgal and Kozlov [31] investigated the influence of two-dimensional humps and forward- and backward-facing steps on the stability of flows over a flat plate. They used a vibrating ribbon to introduce a disturbance with a specific frequency into the boundary layer and measured the

streamwise growth and development of the disturbance as well as its distribution across the boundary layer.

To explain the instability mechanisms enhanced by the imperfection and the physics of ways to control them, Nayfeh, Ragab, and Al-Maaitah [13] investigated the instability of flows around hump and dip imperfections over a flat plate. They computed the mean-flow profiles for incompressible flows using an interacting boundary-layer code which accounts for viscous/inviscid interaction and separation bubbles. They analyzed the two-dimensional linear stability of the flow for several height to width ratios and locations. They correlated the theoretical results with the experimental results of Walker and Greening [23]. They found that separation significantly increases the amplification factor.

Ragab, Nayfeh, and Krishna [41] and Krishna [42] studied compressible boundary layers over a smooth backward-facing step on a flat plate. They compared the mean-flow profiles obtained from the interacting code with a Navier-Stoke solver. They found good agreement. Moreover, they found that compressibility increases the size of separation bubble but overall stabilizes the flow.

Nayfeh, Ragab, and Masad [22] investigated the influence of a two-dimensional hump on the two-dimensional primary and three-dimensional subharmonic secondary instabilities over a flat plate. Again, they calculated the mean-flow profiles for incompressible flow by using interacting boundary layers, thereby accounting for the viscous/inviscid interaction. They found that, in the absence of separation, increasing the height of the hump results in an increase in the amplification factor of the primary and subharmonic waves at all considered frequencies. In the case of separation, they found that the amplification factors are much larger than those obtained for the case of no separation. They concluded that the presence of separation bubbles can be detrimental to the maintenance of laminar flow.

Masad and Nayfeh [21] extended the study of Nayfeh, Ragab, and Masad [22] to the case of compressible flow. Masad and Nayfeh [47] performed stability calculations for the forward- and back-ward facing steps of Dovgal and Kozlov and found good agreement between experimentally and theoretically obtained growth rates. They determined the effect of the

hump height, compressibility, spanwise wavenumber, and frequency on the growth rates and amplification factors of the primary and subharmonic waves. They showed that, although compressibility significantly reduces the amplification factor in the case of a smooth surface, this stabilizing effect decreases as the hump height increases. In the absence of separation, they found that, increasing the hump height results in an increase in the amplification factors of both the primary and subharmonic waves. In the case of separation, they found that the amplification factors are considerably increased.

Al-Maaaitah, Nayfeh, and Ragab [16] investigated the effect of suction on the two-dimensional linear stability of subsonic flows over two-dimensional surface imperfections over a flat plate. They calculated the flow over smooth humps and backward-facing steps with Mach numbers up to 0.8. They found, as expected, that suction considerably reduces the separation region. They showed that continuous suction stabilizes the flow outside the separation bubble, but it destabilizes the flow inside it. They found that the N-factor decreases as the suction level increases. This is due to the considerable reduction in the separation bubble. They found that for the same suction flow rate, properly distributed suction strips stabilize the flow more than continuous suction. They also found that the size of the separation bubble, and hence its effect on the instability, can be considerably reduced by placing strips with high suction velocities in the separation region. They showed that suction does not have much effect on the most dangerous frequency obtained with no suction.

Al-Maaaitah, Nayfeh, and Ragab [15] studied the effect of continuous wall cooling on the two-dimensional linear stability of subsonic flows over two-dimensional surface imperfections over a flat plate. They calculated the flow over smooth humps and backward-facing steps with Mach numbers up to 0.8. They showed that, whereas cooling reduces the viscous instability, it increases the shear-layer instability and hence it increases the growth rates in the separation region.

Masad and Nayfeh [46] investigated the effects of suction and heat-transfer strips on the stability of subsonic boundary layers over a flat plate. They found a reversal in the effect of heating by strips compared with uniform heating. A heating strip located near branch I of the

neutral stability curve very much stabilizes the flow, in contrast with uniform heating, which destabilizes the flow. Also a cooling strip located near branch I of the neutral stability curve destabilizes the flow, in contrast with uniform cooling, which stabilizes the flow. They concluded that a properly placed cooling strip can delay transition in subsonic boundary layers. They determined the optimal locations of heating and cooling strips. Moreover they calculated the influence coefficients for suction strips. These influence coefficients can be used to design "smart" suction configurations.

In this thesis, we extend the work referenced above by investigating the influence of a two-dimensional hump on the stability of compressible boundary layers over an EQH1260 airfoil. We investigate the effects of the height and location of the hump, compressibility, and suction and heat-transfer on the stability of the flow. Continuous suction as well as suction through multiple strips are considered. Moreover, we investigate the effect of heat-transfer through single and multiple strips on controlling the boundary layer. We find that the amplification factor increases as the hump height increases and as the hump is moved downstream. Moreover, we find that compressibility stabilizes the flow and that the most dangerous frequency decreases as the Mach number increases and as the hump is moved downstream. We find that cooling and suction through multiple strips is as effective as continuous cooling and suction. The N-factor decreases as either the suction or cooling rate is increased.

2. Problem Formulation

In conventional boundary layers, one solves for the inviscid flow to determine the slip velocity at the body, which he uses to determine the pressure gradient, and then solves the boundary-layers equations. For smooth surfaces, one can use a conventional boundary-layer formulation to solve for the mean flow over an airfoil. However, conventional boundary-layer solvers cannot account for flows over surfaces with imperfections, such as waviness and bulges, steps and gaps at junctions, three-dimensional roughness elements, suction discontinuities (e.g., suction strips), heat-transfer discontinuities (e.g., cooling or heating strips), and trailing edges, because of the strong viscous/inviscid influence and flow separation.

To account for viscous-inviscid interactions, one needs to use an interacting boundary-layer formulation, a triple-deck formulation, or a Navier-Stokes solver. All of these methods account for the viscous/inviscid interaction as well as separation bubbles, but the Naiver-Stokes solvers are very expensive as compared to the Interacting Boundary-Layer (IBL) solver. Comparison of solutions obtained using IBL with solutions of the Navier-Stokes solvers and/or experiments had shown good agreement. Davis, Carter, and Reshotko [34] developed an interacting boundary-layer technique for the calculation of transitional separation bubbles over infinite swept wings. Veldman [35] developed a quasi-simultaneous interacting-boundary-layer solver for incompressible flow over a flat plate. Gleyzes, Cousteix

and Bonnet [36], Carter and Vasta [37], and Davis and Carter [38] used interacting boundary-layer theory to analyze separation bubbles near the leading edges of airfoils. Davis and Werle [39] used an IBL code to study high Reynolds number flows. Davis [40] solved the compressible interacting boundary layer using an alternating direction explicit method for handling the pressure interaction in supersonic flows past flat plate related bodies.

One approach for carrying out the computations for the case of weak viscous-inviscid interactions starts with an estimate for the displacement surface. Then, the inviscid problem is solved to determine the slip velocity over the new body. The slip velocity is used to compute the pressure gradient and then the boundary layer, which is used to compute the displacement surface. Comparing the estimated and computed displacement surfaces, one can set up an iteration scheme to drive the difference to within a specified tolerance.

In this work, we develop a computer code using an interacting boundary-layer formulation to solve for compressible as well as incompressible flows over airfoils. We solve for the displacement surface and boundary layer simultaneously by using an interaction law, as described next. The analysis follows closely the development which Dr. Saad Ragab gives in his viscous course.

2.1 Boundary-Layer Formulation

The steady boundary-layer equations for a compressible flow consisting of an ideal gas with constant C_p and C_v are:

Conservation of Mass

$$\frac{\partial}{\partial x} (\rho u) + \frac{\partial}{\partial y} (\rho v) = 0 \quad (2.1)$$

x-Momentum Equation

$$\rho u \frac{\partial u}{\partial x} + \rho v \frac{\partial u}{\partial y} = -\frac{\partial p}{\partial x} + \frac{\partial}{\partial y} \left(\mu \frac{\partial u}{\partial y} \right) \quad (2.2)$$

y-Momentum Equation

$$\frac{\partial p}{\partial y} = 0 \quad (2.3)$$

Energy Equation

$$\begin{aligned} \rho u \frac{\partial T}{\partial x} + \rho v \frac{\partial T}{\partial y} &= (\gamma - 1) M_\infty^2 u \frac{\partial p}{\partial x} \\ &+ \frac{1}{Pr} \frac{\partial}{\partial y} \left(\kappa \frac{\partial T}{\partial y} \right) + (\gamma - 1) M_\infty^2 \mu \left(\frac{\partial u}{\partial y} \right)^2 \end{aligned} \quad (2.4)$$

Equation of State

$$\gamma M_\infty^2 p = \rho T \quad (2.5)$$

where x is the distance along the airfoil, y is the distance normal to the airfoil, and the curvature is assumed to be small. All variables are nondimensionalized as follows:

$$x = \frac{x^*}{L^*}, \quad y = \frac{y^*}{L^*} \sqrt{Re}$$

$$u = \frac{u^*}{U_\infty^*}, \quad v = \frac{v^*}{U_\infty^*} \sqrt{Re}$$

$$p = \frac{p^*}{\rho_\infty^* U_\infty^{*2}}, \quad \rho = \frac{\rho^*}{\rho_\infty^*}, \quad T = \frac{T^*}{T_\infty^*}$$

$$\mu = \frac{\mu^*}{\mu_\infty^*}, \quad \kappa = \frac{\kappa^*}{\kappa_\infty^*}, \quad Pr = \frac{\mu_\infty^* C_p^*}{\kappa_\infty^*}$$

$$M_{\infty} = \frac{U_{\infty}^*}{\sqrt{\gamma R^* T_{\infty}^*}}, \quad Re = \frac{\rho_{\infty}^* U_{\infty}^* c^*}{\mu_{\infty}^*}$$

where c^* the airfoil chord. We assume that C_p^* , C_v^* , R^* , and γ are constant.

The wall boundary conditions are

$$u = 0 \quad \text{no-slip condition} \quad (2.6)$$

$$v = \begin{cases} 0 & \text{no-penetration condition} \\ v_w(x) & \text{if there is suction or blowing} \end{cases} \quad (2.7)$$

and

$$T = T_w(x) \quad \text{or} \quad \frac{\partial T}{\partial y} = q(x) \quad (2.8)$$

where T_w is a specified temperature distribution and $q(x)$ is a specified rate of heat transfer.

For an insulated wall, $q(x) = 0$,

$$q^* = \kappa_w^* \frac{\partial T^*}{\partial y^*} = \frac{\kappa_w^* T_{\infty}^* \sqrt{Re}}{L^*} \frac{\partial T}{\partial y}$$

Hence,

$$\frac{\partial T}{\partial y} = \frac{q^* L^*}{\kappa_w^* T_{\infty}^* \sqrt{Re}} = q(x) \quad (2.9)$$

The boundary conditions at infinity are provided by the matching conditions, as $y \rightarrow \infty$,

$$u = u_e(x) \quad \text{and} \quad T = T_e(x) \quad (2.10)$$

where $u_e(x)$ and $T_e(x)$ are the inviscid values of u and T evaluated at the displacement body.

It follows from eq. (2.3) that

$$p = p(x) = p_e(x) \quad (2.11)$$

Because p is independent of y , it follows from eq. (2.5) that

$$\rho T = \rho_e T_e \quad (2.12)$$

or

$$\rho = \frac{\rho_e T_e}{T} \quad (2.13)$$

2.2 Inviscid Flow

To determine $u_e(x)$, $T_e(x)$, and $p_e(x)$, we need to calculate the inviscid flow. We assume it to be isentropic so that

$$\frac{p^*}{p_\infty} = \left(\frac{\rho^*}{\rho_\infty} \right)^\gamma \quad (2.14)$$

It follows from eq. (2.14) that

$$\frac{\rho_\infty^* U_\infty^{*2} p}{R^* \rho_\infty^* T_\infty^*} = \rho^\gamma = \gamma M_\infty^2 p \quad (2.15)$$

Hence,

$$\rho_e^\gamma = \gamma M_\infty^2 p_e \quad (2.16)$$

It follows from eqs. (2.5) and (2.16) that

$$T_e = \rho_e^{\gamma-1} \quad (2.17)$$

Evaluating the inviscid parts of eqs. (2.2) and (2.4) at the wall, we obtain

$$\rho_e u_e \frac{du_e}{dx} = - \frac{dp_e}{dx} \quad (2.18)$$

$$\rho_e u_e \frac{dT_e}{dx} = (\gamma - 1) M_\infty^2 u_e \frac{dp_e}{dx} \quad (2.19)$$

Eliminating p_e from eq. (2.18) and (2.19) yields

$$\frac{dT_e}{dx} + (\gamma - 1) M_\infty^2 u_e \frac{du_e}{dx} = 0 \quad (2.20)$$

which has the integral

$$T_e + \frac{1}{2} (\gamma - 1) M_\infty^2 u_e^2 = \text{constant} \quad (2.21)$$

At the stagnation point, $u_e = 0$ and $T_e = T_0$, where T_0 is the stagnation temperature; thus, evaluating eq. (2.20) at the stagnation point, we have

$$T_e + \frac{1}{2} (\gamma - 1) M_\infty^2 u_e^2 = T_0 \quad (2.22)$$

But the stagnation temperature is given by

$$T_0 = 1 + \frac{1}{2} (\gamma - 1) M_\infty^2 \quad (2.23)$$

Hence,

$$T_e = 1 + \frac{1}{2} (\gamma - 1) M_\infty^2 (1 - u_e^2) \quad (2.24)$$

Consequently, given γ , M_∞ , and one of the four quantities $u_e(x)$, $T_e(x)$, $\rho_e(x)$, and $p_e(x)$, one can calculate the other three from eq. (2.16), (2.17), and (2.24).

Usually, the pressure-coefficient distribution $C_p(x)$ is given, where

$$C_p = \frac{p_e^* - p_\infty^*}{\frac{1}{2} \rho_\infty^* U_\infty^{*2}} \quad (2.25)$$

It follows from eq. (2.25) that

$$C_p = 2 \left(p_e - \frac{R^* \rho_\infty^* T_\infty^*}{\rho_\infty^* U_\infty^{*2}} \right) = 2 \left(p_e - \frac{.1}{\gamma M_\infty^2} \right)$$

Hence,

$$p_e = \frac{1}{\gamma M_\infty^2} + \frac{1}{2} C_p \quad (2.26)$$

Consequently, given $C_p(x)$, one can calculate $p_e(x)$ from eq. (2.26) and then calculate $\rho_e(x)$ from eq. (2.16), $T_e(x)$ from eq. (2.17), and $u_e(x)$ from eq. (2.24).

2.3 Viscosity

Variation of the viscosity coefficient μ^* with temperature T^* is given by the Sutherland formula

$$\frac{\mu^*}{\mu_r^*} = \left(\frac{T^*}{T_r^*} \right)^{3/2} \frac{T_r^* + S^*}{T^* + S^*} \quad (2.27)$$

where μ_r^* is the viscosity coefficient at the reference temperature $T_r^* = 273.1^\circ K$ and $S^* = 110.4^\circ K$. Here,

$$\mu_r^* = 1.716 \times 10^{-7} \frac{g}{cm^3 \sec} = 3.58 \times 10^{-7} \frac{\text{slugs}}{ft^3 \sec}$$

2.4 Initial Conditions

To complete the problem formulation, one needs to specify upstream conditions at some streamwise location x_0 ; that is,

$$u = u_0(y) \quad \text{and} \quad T = T_0(y) \quad \text{at} \quad x = x_0$$

There is no need to specify v at the initial location.

2.5 Levy-Lees Variables

The boundary-layer problem is first transformed by using the Levy-lees variables

$$\xi(x) = \int_0^x \rho_e \mu_e u_e dx \tag{2.28}$$

$$\eta = \frac{u_e}{\sqrt{2\xi}} \int_0^y \rho dy \tag{2.29}$$

$$F(\xi, \eta) = \frac{u(x,y)}{u_e(x)} \tag{2.30}$$

$$Q(\xi, \eta) = \frac{T(x,y)}{T_e(x)} = \frac{\rho_e(x)}{\rho(x,y)} \tag{2.31}$$

$$V = \frac{\sqrt{2\xi}}{\rho_e \mu_e u_e} \left[\rho v + \eta_x \sqrt{2\xi} F \right] \tag{2.32}$$

Using the chain rule, we find that

$$\frac{\partial}{\partial x} = \frac{\partial}{\partial \xi} \frac{\partial \xi}{\partial x} + \frac{\partial}{\partial \eta} \frac{\partial \eta}{\partial x}$$

or

$$\frac{\partial}{\partial x} = \rho_e \mu_e u_e \frac{\partial}{\partial \xi} + \eta_x \frac{\partial}{\partial \eta} \quad (2.33)$$

where $\eta_x = \partial \eta / \partial x$. Similarly,

$$\frac{\partial}{\partial y} = \frac{\partial}{\partial \xi} \frac{\partial \xi}{\partial y} + \frac{\partial}{\partial \eta} \frac{\partial \eta}{\partial y}$$

Because $\xi = \xi(x)$, $\frac{\partial \xi}{\partial y} = 0$, and hence

$$\frac{\partial}{\partial y} = \frac{\rho u_e}{\sqrt{2\xi}} \frac{\partial}{\partial \eta} \quad (2.34)$$

Because $\eta_x = \eta_x(x, y)$,

$$\frac{\partial \eta_x}{\partial y} = \frac{\partial \eta_x}{\partial \xi} \frac{\partial \xi}{\partial y} + \frac{\partial \eta_x}{\partial \eta} \frac{\partial \eta}{\partial y}$$

or

$$\frac{\partial \eta_x}{\partial y} = \frac{\rho u_e}{\sqrt{2\xi}} \frac{\partial \eta_x}{\partial \eta} \quad (2.35)$$

$$\begin{aligned} \frac{\partial \eta_x}{\partial y} &= \frac{\partial}{\partial x} \left(\frac{\partial \eta}{\partial y} \right) = \frac{\partial}{\partial x} \left(\frac{\rho u_e}{\sqrt{2\xi}} \right) \\ &= \frac{u_e}{\sqrt{2\xi}} \frac{\partial \rho}{\partial x} + \rho \frac{\partial}{\partial x} \left(\frac{u_e}{\sqrt{2\xi}} \right) \end{aligned}$$

Hence,

$$\frac{\partial \eta_x}{\partial \eta} = \frac{\sqrt{2\xi}}{\rho u_e} \frac{\partial \eta_x}{\partial y}$$

or

$$\frac{\partial \eta_x}{\partial \eta} = \frac{1}{\rho} \frac{\partial \rho}{\partial x} + \frac{\sqrt{2\xi}}{u_e} \frac{\partial}{\partial x} \left(\frac{u_e}{\sqrt{2\xi}} \right) \quad (2.36)$$

Substituting eq. (2.30) into eq. (2.1) and using eqs. (2.33) and (2.34), we obtain

$$\begin{aligned} & \rho_e \mu_e u_e \left[\rho u_e \frac{\partial F}{\partial \xi} + \rho F \frac{\partial u_e}{\partial \xi} + u_e F \frac{\partial \rho}{\partial \xi} \right] \\ & + u_e \eta_x \left[\rho \frac{\partial F}{\partial \eta} + F \frac{\partial \rho}{\partial \eta} \right] + \frac{\rho u_e}{\sqrt{2\xi}} \frac{\partial}{\partial \eta} (\rho v) = 0 \end{aligned} \quad (2.37)$$

or

$$\begin{aligned} & \rho_e \mu_e u_e \rho \left[u_e \frac{\partial F}{\partial \xi} + F \frac{\partial u_e}{\partial \xi} \right] + u_e \rho \eta_x \frac{\partial F}{\partial \eta} \\ & + \frac{\rho u_e}{\sqrt{2\xi}} \frac{\partial}{\partial \eta} (\rho v) + u_e F \left[\rho_e \mu_e u_e \frac{\partial \rho}{\partial \xi} + \eta_x \frac{\partial \rho}{\partial \eta} \right] = 0 \end{aligned}$$

or

$$\begin{aligned} & \rho_e \mu_e \left[u_e \frac{\partial F}{\partial \xi} + F \frac{\partial u_e}{\partial \xi} \right] + \eta_x \frac{\partial F}{\partial \eta} \\ & + \frac{1}{\sqrt{2\xi}} \frac{\partial}{\partial \eta} (\rho v) + \frac{F}{\rho} \frac{\partial \rho}{\partial x} = 0 \end{aligned} \quad (2.38)$$

on account of eq. (2.33). Differentiating eq. (2.32) with respect to η yields

$$\frac{\partial v}{\partial \eta} = \frac{\sqrt{2\xi}}{\rho_e \mu_e u_e} \left[\frac{\partial}{\partial \eta} (\rho v) + \eta_x \sqrt{2\xi} \frac{\partial F}{\partial \eta} + \sqrt{2\xi} F \frac{\partial}{\partial \eta} (\eta_x) \right]$$

which, upon using eq. (2.36), becomes

$$\begin{aligned} \frac{\partial V}{\partial \eta} = & \frac{\sqrt{2\xi}}{\rho_e \mu_e u_e} \left[\frac{\partial}{\partial \eta} (\rho v) + \eta_x \sqrt{2\xi} \frac{\partial F}{\partial \eta} \right. \\ & \left. + \frac{\sqrt{2\xi} F}{\rho} \frac{\partial \rho}{\partial x} + \frac{2\xi}{u_e} F \frac{\partial}{\partial x} \left(\frac{u_e}{\sqrt{2\xi}} \right) \right] \end{aligned} \quad (2.39)$$

It follows from eq. (2.38) that

$$\begin{aligned} \frac{\partial}{\partial \eta} (\rho v) + \eta_x \sqrt{2\xi} \frac{\partial F}{\partial \eta} + \frac{\sqrt{2\xi} F}{\rho} \frac{\partial \rho}{\partial x} = \\ - \rho_e \mu_e \sqrt{2\xi} \left[u_e \frac{\partial F}{\partial \xi} + F \frac{\partial u_e}{\partial \xi} \right] \end{aligned} \quad (2.40)$$

Substituting eq. (2.40) into eq. (2.39) yields

$$\frac{\partial V}{\partial \eta} = -2\xi \frac{\partial F}{\partial \xi} - \frac{2\xi}{u_e} F \left[\frac{\partial u_e}{\partial \xi} - \frac{\sqrt{2\xi}}{\rho_e \mu_e u_e} \frac{\partial}{\partial x} \left(\frac{u_e}{\sqrt{2\xi}} \right) \right]$$

or

$$\frac{\partial V}{\partial \eta} = -2\xi \frac{\partial F}{\partial \xi} - \frac{2\xi}{u_e} F \left[\frac{\partial u_e}{\partial \xi} - \sqrt{2\xi} \frac{\partial}{\partial \xi} \left(\frac{u_e}{\sqrt{2\xi}} \right) \right]$$

or

$$2\xi F_\xi + V_\eta + F = 0 \quad (2.41)$$

Substituting eqs. (2.18), (2.30)-(2.34) into eq. (2.2), we obtain

$$\begin{aligned} \rho u_e F \left[\rho_e \mu_e u_e \frac{\partial}{\partial \xi} (u_e F) + \eta_x u_e \frac{\partial F}{\partial \eta} \right] \\ + \rho v \frac{\rho u_e^2}{\sqrt{2\xi}} \frac{\partial F}{\partial \eta} = \rho_e^2 \mu_e u_e^2 \frac{du_e}{d\xi} + \frac{\rho u_e^3}{2\xi} \frac{\partial}{\partial \eta} \left(\rho \mu \frac{\partial F}{\partial \eta} \right) \end{aligned}$$

or

$$\begin{aligned}
& F \left[\frac{\partial F}{\partial \xi} + \frac{F}{u_e} \frac{du_e}{d\xi} \right] + \frac{\eta_x}{\rho_e \mu_e u_e} F \frac{\partial F}{\partial \eta} + \frac{\rho v}{\rho_e \mu_e u_e \sqrt{2\xi}} \frac{\partial F}{\partial \eta} \\
& = \frac{\rho_e}{\rho u_e} \frac{du_e}{d\xi} + \frac{1}{2\xi} \frac{\partial}{\partial \eta} \left(\frac{\rho \mu}{\rho_e \mu_e} \frac{\partial F}{\partial \eta} \right)
\end{aligned}$$

which, upon using eq. (2.32), becomes

$$2\xi F F_\xi + v F_\eta - \frac{\partial}{\partial \eta} \left(\theta \frac{\partial F}{\partial \eta} \right) + \beta (F^2 - Q) = 0 \quad (2.42)$$

where

$$\beta = \frac{2\xi}{u_e} \frac{du_e}{d\xi} \quad \text{and} \quad \theta = \frac{\rho \mu}{\rho_e \mu_e} \quad (2.43)$$

Substituting eqs. (2.18), (2.30), (2.31), (2.33), and (2.34) into eq. (2.4), we have

$$\begin{aligned}
& \rho u_e F \left[\rho_e \mu_e u_e \left(T_e \frac{\partial Q}{\partial \xi} + Q \frac{dT_e}{d\xi} \right) + \eta_x T_e \frac{\partial Q}{\partial \eta} \right] \\
& + \rho v \frac{\rho u_e T_e}{\sqrt{2\xi}} \frac{\partial Q}{\partial \eta} = -(\gamma - 1) M_\infty^2 u_e F \rho_e^2 \mu_e u_e^2 \frac{du_e}{d\xi} \\
& + \frac{\rho u_e^2 T_e}{2\xi Pr} \frac{\partial}{\partial \eta} \left(\rho \kappa \frac{\partial Q}{\partial \eta} \right) + (\gamma - 1) M_\infty^2 \mu \frac{u_e^4 \rho^2}{2\xi} \left(\frac{\partial F}{\partial \eta} \right)^2
\end{aligned}$$

or

$$\begin{aligned}
& 2\xi F \frac{\partial Q}{\partial \xi} + \frac{2\xi}{T_e} \left[\frac{dT_e}{d\xi} + (\gamma - 1) M_\infty^2 u_e \frac{du_e}{d\xi} \right] F Q \\
& + \frac{\sqrt{2\xi}}{\rho_e \mu_e u_e} [\rho v + \eta_x \sqrt{2\xi} F] \frac{\partial Q}{\partial \eta} - \frac{\partial}{\partial \eta} \left(\frac{\rho \kappa}{\rho_e \mu_e Pr} \frac{\partial Q}{\partial \eta} \right) - \alpha \theta \left(\frac{\partial F}{\partial \eta} \right)^2 = 0
\end{aligned} \quad (2.44)$$

where

$$\alpha = (\gamma - 1) M_\infty^2 \frac{u_e^2}{T_e} \quad (2.45)$$

Differentiating eq. (2.21) with respect to ξ and using eq. (2.32), we simplify eq. (2.44) into

$$2\xi FQ_\xi + VQ_\eta - \frac{\partial}{\partial \eta} \left(\frac{\theta}{\hat{P}_r} \frac{\partial Q}{\partial \eta} \right) - \alpha \theta \left(\frac{\partial F}{\partial \eta} \right)^2 = 0 \quad (2.46)$$

where

$$\hat{P}_r = \frac{\mu Pr}{\kappa} \quad (2.47)$$

Therefore the boundary-layer equations are summarized as follows :

$$2\xi F_\xi + V_\eta + F = 0 \quad (2.48)$$

$$2\xi FF_\xi + VF_\eta - \frac{\partial}{\partial \eta} \left(\theta \frac{\partial F}{\partial \eta} \right) + \beta(F^2 - Q) = 0 \quad (2.49)$$

$$2\xi FQ_\xi + VQ_\eta - \frac{\partial}{\partial \eta} \left(\frac{\theta}{\hat{P}_r} \frac{\partial Q}{\partial \eta} \right) - \alpha \theta \left(\frac{\partial F}{\partial \eta} \right)^2 = 0 \quad (2.50)$$

where

$$\beta = \frac{2\xi}{u_e} \frac{du_e}{d\xi} \quad \text{and} \quad \theta = \frac{\rho \mu}{\rho_e \mu_e}$$

$$\hat{P}_r = \frac{\mu Pr}{\kappa} \quad \text{and} \quad \alpha = (\gamma - 1) M_\infty^2 \frac{u_e^2}{T_e}$$

For a Newtonian fluid $\frac{\mu}{\kappa} = 1$

We solve eqs. (2.48), (2.49), and (2.50) using an adaptive second-order finite-differencing scheme in η and a three-point backward-differencing scheme in ξ in the form

$$G_{\xi m} = a_{0m}G_m + a_{1m}G_{m-1} + a_{2m}G_{m-2} \quad (2.51)$$

Therefore, F_ξ and Q_ξ are replaced with

$$F_{\xi m} = a_{0m}F_m + a_{1m}F_{m-1} + a_{2m}F_{m-2} \quad (2.52)$$

$$Q_{\xi m} = a_{0m}Q_m + a_{1m}Q_{m-1} + a_{2m}Q_{m-2} \quad (2.53)$$

where

$$a_{0m} = \frac{2\xi_m - \xi_{m-1} - \xi_{m-2}}{(\xi_m - \xi_{m-1})(\xi_m - \xi_{m-2})} \quad (2.54)$$

$$a_{1m} = \frac{\xi_m - \xi_{m-2}}{(\xi_m - \xi_{m-1})(\xi_{m-1} - \xi_{m-2})} \quad (2.55)$$

$$a_{2m} = \frac{\xi_m - \xi_{m-1}}{(\xi_m - \xi_{m-2})(\xi_{m-1} - \xi_{m-2})} \quad (2.56)$$

Equations (2.52) and (2.53) imply that F and Q are known at the previous grid points $m-1$ and $m-2$, which is true for all $m \geq 3$. At $m = 1, \xi_1 = 0$ and hence $\xi F_\xi = 0$ and $\xi Q_\xi = 0$. Thus, we take

$$a_{01} = a_{11} = a_{21} = 0 \quad (2.57)$$

At $m = 2$, we drop the accuracy to first order in $\Delta\xi$, use a two-point backward differencing scheme, and obtain

$$a_{02} = -a_{12} = \frac{1}{\xi_2 - \xi_1} \text{ and } a_{22} = 0 \quad (2.58)$$

2.6 Boundary-Layer Parameters

The friction coefficient C_f is defined by

$$C_f = \frac{\tau_w^*}{\frac{1}{2} \rho_\infty U_\infty^2}$$

But

$$\tau_w^* = \mu_w^* \frac{\partial u^*}{\partial y^*} \Big|_{y^*=0}$$

hence

$$\begin{aligned} C_f &= \frac{2\mu_w^* U_\infty^* \sqrt{Re}}{L^* \rho_\infty^* U_\infty^{*2}} \frac{\partial u}{\partial y} \Big|_{y=0} = \frac{2\mu_w \mu_\infty^* \sqrt{Re} \rho_w u_e^2}{\rho_\infty^* U_\infty^* L^* \sqrt{2\xi}} \frac{\partial F}{\partial \eta} \Big|_{\eta=0} \\ &= 2\mu_e \rho_e u_e^2 \frac{1}{\sqrt{2\xi Re}} \theta_w \frac{\partial F}{\partial \eta} \Big|_{\eta=0} \end{aligned} \quad (2.59)$$

Consequently,

$$C_f \sqrt{Re_x} = 2\mu_e \rho_e u_e^2 \sqrt{\frac{x}{2\xi}} \theta_w \frac{\partial F}{\partial \eta} \Big|_{\eta=0} \quad (2.60)$$

The displacement thickness is defined by

$$\delta^* \rho_e^* u_e^* = \int_0^\infty (\rho_e^* u_e^* - \rho^* u^*) dy^*$$

or

$$\frac{\delta^* \sqrt{Re}}{L^*} = \int_0^\infty \left(1 - \frac{\rho u}{\rho_e u_e} \right) dy \quad (2.61)$$

It follows from eq. (2.29) that

$$dy = \frac{\sqrt{2\xi}}{\rho u_e} d\eta$$

Hence, eq. (2.61) can be rewritten as

$$\delta = \frac{\delta^* \sqrt{Re}}{L^*} = \frac{\sqrt{2\xi}}{\rho_e u_e} \int_0^\infty (Q - F) d\eta \quad (2.62)$$

on account of eqs. (2.30) and (2.31).

2.7 Interacting Law

Because conventional boundary-layer theory fail in the presence of a separation bubble, we use an interacting-boundary-layer formulation to solve for the pressure gradient and boundary layer simultaneously. Using thin airfoil theory, one obtains the following interacting law for the total velocity [41]:

$$u_e = \tilde{u}_e + \frac{1}{\pi \sqrt{Re} \sqrt{1 - M_\infty^2}} \left[\int_{L.E.}^\infty \frac{\frac{d}{dt} (u_e \delta)}{x - t} dt \right] \quad (2.63)$$

where \tilde{u}_e is given by

$$\tilde{u}_e = u_{eo} + \frac{1}{\pi\sqrt{1-M_\infty^2}} \left[\int_{L.E.}^{\infty} \frac{\frac{d}{dt}(u_{eo}f)}{x-t} dt + \int_{L.E.}^{\infty} \frac{\frac{d}{dt}(\ln \rho_e)}{x-t} dt \right] \quad (2.64)$$

Here, u_{eo} is the inviscid velocity in the absence of the the imperfection and $y = f(x)$ is the shape of the imperfection given by

$$y = y^*/L^* = (h^*/L^*)f(\zeta) = hf(\zeta) \quad (2.65)$$

In the present work, we choose $f(\zeta)$ to be

$$f(\zeta) = \begin{cases} 1 - 12\zeta^2 + 16|\zeta|^3 & \text{if } |\zeta| \leq 1 \\ 0 & \text{if } |\zeta| > 1 \end{cases} \quad (2.66)$$

$$\zeta = (x^* - x_m^*)/b^* = (x - x_m)/b \quad (2.67)$$

where h^* is the height of the hump, b^* is the width of the hump, x_m^* is the streamwise distance from the leading edge of the airfoil to the center of the hump, and the star denotes a dimensional quantity.

Equations (2.63) and (2.64) are singular at $t=x$; therefore the principal values of the Cauchy integrals are assumed. To determine the principal values of the singular integrals in eqs. (2.63) and (2.64), we approximate f and δ by piecewise linear functions.

The integrals in eqs. (2.63) and (2.64) have the form

$$I = \int_{L.E.}^{\infty} \frac{\frac{dT}{dt}}{x-t} dt \quad (2.68)$$

We assume that the interaction region extends from x_e to x_r and hence approximate eq. (2.68) as

$$I = \int_{L.E.}^{\infty} \frac{\frac{dT}{dt}}{x-t} dt \approx \int_{x_\ell}^{x_r} \frac{\frac{dT}{dt}}{x-t} dt \quad (2.69)$$

Because the integral in eq. (2.69) is singular at $t=x$, we break the integral into two parts and obtain

$$I = \lim_{\varepsilon \rightarrow 0} \left[\int_{x_\ell}^{x-\varepsilon} \frac{\frac{dT}{dt}}{x-t} dt + \int_{x+\varepsilon}^{x_r} \frac{\frac{dT}{dt}}{x-t} dt \right] \quad (2.70)$$

where ε is a small positive number. Using integration by parts in eq. (2.70), we obtain

$$\begin{aligned} I &= \lim_{\varepsilon \rightarrow 0} \left[\frac{T}{x-t} \Big|_{x_\ell}^{x-\varepsilon} + \frac{T}{x-t} \Big|_{x+\varepsilon}^{x_r} \right. \\ &\quad \left. - \int_{x_\ell}^{x-\varepsilon} \frac{T}{(x-t)^2} dt - \int_{x+\varepsilon}^{x_r} \frac{T}{(x-t)^2} dt \right] \\ &= \frac{T(x_r)}{x-x_r} - \frac{T(x_\ell)}{x-x_\ell} + \lim_{\varepsilon \rightarrow 0} \left[\frac{T(x-\varepsilon)}{\varepsilon} - \frac{T(x+\varepsilon)}{-\varepsilon} \right. \\ &\quad \left. - \int_{x_\ell}^{x-\varepsilon} \frac{T}{(x-t)^2} dt - \int_{x+\varepsilon}^{x_r} \frac{T}{(x-t)^2} dt \right] \end{aligned} \quad (2.71)$$

Now, we evaluate the integrals

$$I_\ell = \int_{x_\ell}^{x-\varepsilon} \frac{T dt}{(x-t)^2} \quad (2.72)$$

and

$$I_r = \int_{x+\varepsilon}^{x_r} \frac{T dt}{(x-t)^2} \quad (2.73)$$

in eq. (2.71) by approximating T by a piecewise linear function. We divide the interval (x_ℓ, x_r) into equally spaced intervals with length Δx . The interacting boundary-layer equations are solved at the midpoints x_1, x_2, \dots, x_m of these equally spaced intervals. In terms of x_1 and x_m , x_ℓ and x_r are given by

$$x_\ell = x_1 - \frac{1}{2} \Delta x \quad (2.74)$$

$$x_r = x_m + \frac{1}{2} \Delta x \quad (2.75)$$

We approximate the variation of T over an interval by a linear function. Thus, over the interval $(x_j - \frac{1}{2} \Delta x, x_j + \frac{1}{2} \Delta x)$ centered at x_j , we have

$$T = T_j + a(t - x_j), \quad x_j - \frac{1}{2} \Delta x \leq t \leq x_j + \frac{1}{2} \Delta x \quad (2.76)$$

where

$$a = \frac{T_{j+1} - T_{j-1}}{2\Delta x} \quad (2.77)$$

is the slope. Letting

$$\tau = \frac{t - x_j}{\Delta x} \quad \text{or} \quad t = \tau \Delta x + x_j \quad (2.78)$$

in eq. (2.76) and using eq. (2.77), we obtain

$$T = T_j + \frac{1}{2} (T_{j+1} - T_{j-1})\tau, \quad -\frac{1}{2} \leq \tau \leq \frac{1}{2} \quad (2.79)$$

Next, we evaluate the integral in eq. (2.72) at $x = x_i$; that is,

$$I_\ell(x_i) = \int_{x_\ell}^{x_i - \epsilon} \frac{T dt}{(x_i - t)^2} \quad (2.80)$$

We isolate the contribution of the part of the interval containing x_i ; that is,

$$l_{\ell}(x_i) = \int_{x_{\ell}}^{x_i} \frac{T dt}{(x_i - t)^2} + \int_{x_i}^{x_i - \varepsilon} \frac{T dt}{(x_i - t)^2} \quad (2.81)$$

where

$$x_i = x_{i-1} + \frac{1}{2} \Delta x \quad (2.82)$$

Next, we determine the contribution of the interval $(x_j - \frac{1}{2} \Delta x, x_j + \frac{1}{2} \Delta x)$ centered at x_j on element x_i . In this interval, we have

$$T = T_j + \frac{1}{2} (T_{j+1} - T_{j-1}) \tau \quad (2.83)$$

$$t = x_j + \tau \Delta x, \quad dt = \Delta x d\tau \quad (2.84)$$

Using eqs. (2.83) and (2.84), we find that the contribution of the interval centered at x_j on element x_i can be evaluated as follows:

$$l_{\ell j}(x_i) = \int_{x_j - \frac{1}{2} \Delta x}^{x_j + \frac{1}{2} \Delta x} \frac{T dt}{(x_i - t)^2} = \int_{-\frac{1}{2}}^{\frac{1}{2}} \frac{T_j + \frac{1}{2} (T_{j+1} - T_{j-1}) \tau}{(x_i - x_j - \tau \Delta x)^2} \Delta x d\tau \quad (2.85)$$

Using the fact that $x_i - x_j = (i - j) \Delta x$, and carrying out the integration in (2.85) yields

$$\begin{aligned}
I_{\ell_j}(x_i) &= \frac{T_j}{\Delta x} \int_{-\frac{1}{2}}^{\frac{1}{2}} \frac{d\tau}{(k-\tau)^2} + \frac{1}{2} \frac{(T_{j+1} - T_{j-1})}{\Delta x} \int_{-\frac{1}{2}}^{\frac{1}{2}} \frac{\tau}{(k-\tau)^2} d\tau \\
&= \frac{T_j}{\Delta x} \left[\frac{1}{k-\tau} \right]_{-\frac{1}{2}}^{\frac{1}{2}} + \frac{1}{2} \frac{(T_{j+1} - T_{j-1})}{\Delta x} \left[\frac{k d\tau}{(k-\tau)^2} - \int \frac{d\tau}{k-\tau} \right] \\
&= \frac{T_j}{\Delta x} \left[\frac{1}{k-\frac{1}{2}} - \frac{1}{k+\frac{1}{2}} \right] + \frac{1}{2} \frac{(T_{j+1} - T_{j-1})}{\Delta x} \left[\frac{k}{k-\tau} + \ln(k-\tau) \right]_{-1/2}^{1/2} \\
&= \frac{4T_j}{\Delta x(4k^2 - 1)} + \frac{1}{2} \frac{(T_{j+1} - T_{j-1})}{\Delta x} \left[\frac{2k}{2k-1} - \frac{2k}{2k+1} + \ln \frac{2k-1}{2k+1} \right] \\
&= -\frac{4T_j}{\Delta x(1-4k^2)} + \frac{(T_{j+1} - T_{j-1})}{\Delta x} \left[\frac{2k}{4k^2-1} + \frac{1}{2} \ln \frac{2k-1}{2k+1} \right]
\end{aligned}$$

or

$$I_{\ell_j}(x_i) = -\frac{4}{\Delta x} [T_j D_k + E_k (T_{j+1} - T_{j-1})] \quad (2.86)$$

where $k = i - j$,

$$D_k = \frac{1}{1-4k^2} \quad (2.87)$$

$$E_k = \frac{k}{2(1-4k^2)} - \frac{1}{8} \ln \frac{2k-1}{2k+1} \quad (2.88)$$

Using eqs. (2.83) and (2.84), we find that the second integral in eq. (2.81) is

$$\begin{aligned}
l_{\ell i} &= \int_{x_i}^{x_i - \varepsilon} \frac{T dt}{(x_i - t)^2} = \int_{x_i - \frac{1}{2} \Delta x}^{x_i - \varepsilon} \frac{T_i + \frac{1}{2} (T_{i+1} - T_{i-1}) \tau}{\tau^2 (\Delta x)^2} \Delta x d\tau \\
&= \frac{T_i}{\Delta x} \int_{-\frac{1}{2}}^{-\frac{\varepsilon}{\Delta x}} \frac{d\tau}{\tau^2} + \frac{T_{i+1} - T_{i-1}}{2 \Delta x} \int_{-\frac{1}{2}}^{-\frac{\varepsilon}{\Delta x}} \frac{d\tau}{\tau} \\
&= \frac{T_i}{\Delta x} \left[-\frac{1}{\tau} \right]_{-\frac{1}{2}}^{-\frac{\varepsilon}{\Delta x}} + \frac{T_{i+1} - T_{i-1}}{2 \Delta x} \ln \tau \Big|_{-\frac{1}{2}}^{-\frac{\varepsilon}{\Delta x}} \\
&= \frac{T_i}{\varepsilon} - \frac{2T_i}{\Delta x} + \frac{T_{i+1} - T_{i-1}}{\Delta x} \ln \left(\frac{2\varepsilon}{\Delta x} \right)
\end{aligned} \tag{2.89}$$

Adding eqs. (2.86) and (2.89), we find that the value of the integral in eq. (2.72) is

$$\begin{aligned}
l_{\ell} &= \int_{x_{\ell}}^{x_i - \varepsilon} \frac{T dt}{(x - t)^2} = \sum_{j=1}^{i-1} -\frac{4}{\Delta x} [T_j D_k + E_k (T_{j+1} - T_{j-1})] \\
&\quad + \frac{T_i}{\varepsilon} - \frac{2T_i}{\Delta x} + \frac{T_{i+1} - T_{i-1}}{\Delta x} \ln \left(\frac{2\varepsilon}{\Delta x} \right)
\end{aligned} \tag{2.90}$$

Following the same procedure, we rewrite the integral in eq. (2.73) as

$$l_r = \int_{x+\varepsilon}^{x_r} \frac{T dt}{(x - t)^2} = \int_{x_i}^{x_r} \frac{T dt}{(x - t)^2} + \int_{x+\varepsilon}^{x_i} \frac{T dt}{(x - t)^2} \tag{2.91}$$

$$x_l = x_i + \frac{1}{2} \Delta x \tag{2.92}$$

The contribution of the j th interval to the first integral in eq. (2.91) is

$$l_{rj}(x_i) = \int_{x_j - \frac{1}{2} \Delta x}^{x_j + \frac{1}{2} \Delta x} \frac{T_j + \frac{1}{2} (T_{j+1} - T_{j-1}) \tau}{(x_i - x_j - \tau \Delta x)^2} \Delta x d\tau$$

or

$$I_{rj}(x_i) = \frac{1}{\Delta x} \int_{-\frac{1}{2}}^{\frac{1}{2}} \frac{T_j + \frac{1}{2}(T_{j+1} - T_{j-1})\tau}{(i-j-\tau)^2} d\tau \quad (2.93)$$

Carrying out the integration in eq. (2.93) yields

$$\begin{aligned} I_{rj} &= \frac{T_j}{\Delta x} \int_{-\frac{1}{2}}^{\frac{1}{2}} \frac{d\tau}{(k+\tau)^2} + \frac{(T_{j+1} - T_{j-1})}{2\Delta x} \int_{-\frac{1}{2}}^{\frac{1}{2}} \frac{\tau}{(k+\tau)^2} d\tau \\ &= \frac{T_j}{\Delta x} \left[-\frac{1}{k+\tau} \right]_{-\frac{1}{2}}^{\frac{1}{2}} + \frac{T_{j+1} - T_{j-1}}{2\Delta x} \int_{-\frac{1}{2}}^{\frac{1}{2}} \left[\frac{d\tau}{k+\tau} - \frac{k d\tau}{(k+\tau)^2} \right] \\ &= \frac{T_j}{\Delta x} \left[\frac{1}{k - \frac{1}{2}} - \frac{1}{k + \frac{1}{2}} \right] + \frac{T_{j+1} - T_{j-1}}{2\Delta x} \left[\ln \frac{k + \frac{1}{2}}{k - \frac{1}{2}} + \frac{k}{k + \tau} \right]_{-1/2}^{1/2} \\ &= \frac{4T_j}{\Delta x(4k^2 - 1)} + \frac{T_{j+1} - T_{j-1}}{2\Delta x} \left[\ln \frac{2k+1}{2k-1} + \frac{4k}{1-4k^2} \right] \\ &= -\frac{4}{\Delta x} \left[D_k T_j - (T_{j+1} - T_{j-1}) \left(\frac{1}{2} k D_k - \frac{1}{8} \ln \frac{2k-1}{2k+1} \right) \right] \end{aligned} \quad (2.94)$$

or

$$I_{rj} = -\frac{4}{\Delta x} [D_k T_j - (T_{j+1} - T_{j-1}) E_k] \quad (2.95)$$

where $k = j - i$ and D_k and E_k are defined in eqs. (2.87) and (2.88).

Substituting eqs. (2.83) and (2.84) into the second integral in eq. (2.91), we have

$$I_{rj} = \int_{x_i + \varepsilon}^{x_i + \frac{1}{2} \Delta x} \frac{T dt}{(x_i - t)^2} = \int_{\frac{\varepsilon}{\Delta x}}^{\frac{1}{2}} \frac{T_i + \frac{1}{2}(T_{i+1} - T_{i-1})\tau}{\tau^2 (\Delta x)^2} \Delta x d\tau \quad (2.96)$$

Carrying out the integration in eq. (2.96) yields

$$I_{ri} = \frac{T_i}{\Delta x} \left[-\frac{1}{\tau} \left| \frac{\frac{1}{2}}{\frac{\varepsilon}{\Delta x}} \right| \right] + \frac{T_{i+1} - T_{i-1}}{2\Delta x} \ln \tau \left| \frac{\frac{1}{2}}{\frac{\varepsilon}{\Delta x}} \right|$$

or

$$I_{ri} = -\frac{2T_i}{\Delta x} + \frac{T_i}{\varepsilon} + \frac{T_{i+1} - T_{i-1}}{2\Delta x} \ln \left(\frac{\Delta x}{2\varepsilon} \right) \quad (2.97)$$

Adding eqs. (2.95) and (2.97), we obtain the following expression for the integral in eq. (2.73):

$$I_r = \int_{x_i + \varepsilon}^{x_r} \frac{T dt}{(x - t)^2} = -\frac{4}{\Delta x} \sum_{j=i+1}^M [T_j D_k - E_k (T_{j+1} - T_{j-1})] - \frac{2T_i}{\Delta x} + \frac{T_i}{\varepsilon} - \frac{T_{i+1} - T_{i-1}}{2\Delta x} \ln \frac{2\varepsilon}{\Delta x} \quad (2.98)$$

Adding eqs. (2.90) and (2.98), we find that the principal value of the singular integral in eq. (2.70) is

$$I(x_i) = \int_{x_\ell}^{x_r} \frac{\frac{dT}{dt} dt}{x_i - t} = \frac{T(x_r)}{x_i - x_r} - \frac{T(x_\ell)}{x_i - x_\ell} + \frac{4}{\Delta x} \sum_{j=1}^{i-1} [T_j D_k + E_k (T_{j+1} - T_{j-1})] + \frac{4}{\Delta x} \sum_{j=i+1}^M T_j D_k - E_k (T_{j+1} - T_{j-1}) + \frac{4T_i}{\Delta x} \quad (2.99)$$

where D_k is given by eq. (2.87), E_k is given by eq. (2.88), and $k = |i - j|$. Equation (2.99) can be rewritten as

$$\int_{x_\ell}^{x_r} \frac{dT}{x-t} dt = \frac{T(x_r)}{x_i - x_r} - \frac{T(x_\ell)}{x_i - x_\ell} + \frac{4}{\Delta x} \left[\sum_{j=1}^M T_j D_k + \text{sgn}(i-j) E_k (T_{j+1} - T_{j-1}) \right] \quad (2.100)$$

where

$$\text{sgn}(i-j) = \begin{cases} 1 & \text{if } i > j \\ 0 & \text{if } i = j \\ -1 & \text{if } i < j \end{cases}$$

Going back to eq. (2.63), we rewrite it as

$$u_e = \tilde{u}_e + \frac{\lambda \Delta x}{4} \int_{L.E.}^{\infty} \frac{d}{dt} \frac{(u_e \delta)}{x-t} dt \quad (2.101)$$

where

$$\lambda = \frac{4}{\Delta x \pi \sqrt{Re(1 - M_\infty^2)}} \quad (2.102)$$

Letting $T = u_e \delta$ in eq. (2.100) and substituting the result into eq. (2.101), we obtain

$$u_{e_i} = \tilde{u}_{e_i} + \frac{\lambda (u_e \delta)_M \Delta x}{4(x_i - x_r)} - \frac{\lambda (u_e \delta)_1 \Delta x}{4(x_i - x_l)} + \lambda \sum_{j=1}^M [(u_e \delta)_j D_k + \text{sgn}(i-j) E_k ((u_e \delta)_{j+1} - (u_e \delta)_{j-1})] \quad (2.103)$$

or in expanded form

$$\begin{aligned}
u_{e_i} = & \tilde{u}_{e_i} + \lambda \left\{ (u_e \delta)_1 g_1(i) + (u_e \delta)_M g_2(i) + (u_e \delta)_i \right. \\
& + \sum_{j=1}^{i-1} [(u_e \delta)_j D_k + E_k((u_e \delta)_{j+1} - (u_e \delta)_{j-1})] \\
& \left. + \sum_{j=i+1}^M [(u_e \delta)_j D_k - E_k((u_e \delta)_{j+1} - (u_e \delta)_{j-1})] \right\}
\end{aligned} \tag{2.104}$$

where

$$g_1(i) = -\frac{\Delta x}{4(x_i - x_l)}$$

$$g_2(i) = \frac{\Delta x}{4(x_i - x_r)}$$

When $i = 1$, the contribution of the first summation in eq. (2.104) is zero and hence

$$\begin{aligned}
u_{e1} = & \tilde{u}_{e1} + \lambda \left\{ (1 + g_1(1))(u_e \delta)_1 + (u_e \delta)_M g_2(1) \right. \\
& \left. + \sum_{j=2}^M [(u_e \delta)_j D_k - E_k((u_e \delta)_{j+1} - (u_e \delta)_{j-1})] \right\}
\end{aligned} \tag{2.105}$$

We expand the summation in eq. (2.105) to $j=3$ and obtain

$$\begin{aligned}
u_{e1} = & \tilde{u}_{e1} + \lambda \left\{ [1 + g_1(1)](u_e \delta)_1 + (u_e \delta)_M g_2(1) \right. \\
& + D_1(u_e \delta)_2 - E_1(u_e \delta)_3 + E_1(u_e \delta)_1 \\
& \left. + \sum_{j=3}^M [(u_e \delta)_j D_k - E_k((u_e \delta)_{j+1} - (u_e \delta)_{j-1})] \right\}
\end{aligned} \tag{2.106}$$

$$u_{e1} = \lambda G_1 + \lambda \Gamma_1 (u_e \delta)_1 \quad (2.107)$$

$$G_1 = \frac{\tilde{u}_{e1}}{\lambda} + (u_e \delta)_M g_2(1) + D_1(u_e \delta)_2 - E_1(u_e \delta)_3 \\ + \sum_{j=3}^M [(u_e \delta)_j D_k - E_k((u_e \delta)_{j+1} - (u_e \delta)_{j-1})] \quad (2.108)$$

$$\Gamma_1 = 1 + g_1(1) + E_1 \quad (2.109)$$

When $i = M$, the contribution of the last summation in eq. (2.104) is zero. Then, we expand the summation to $M-2$ and obtain

$$u_{eM} = \tilde{u}_{eM} + \lambda \left\{ (u_e \delta)_1 g_1(M) + (u_e \delta)_M g_2(M) \right. \\ \left. + (u_e \delta)_M + (u_e \delta)_{M-1} D_1 + E_1(u_e \delta)_M \right. \\ \left. - E_1(u_e \delta)_{M-2} + \sum_{j=1}^{M-2} [(u_e \delta)_j D_k + E_k((u_e \delta)_{j+1} - (u_e \delta)_{j-1})] \right\} \quad (2.110)$$

$$u_{eM} = \lambda G_M + \lambda \Gamma_M (u_e \delta)_M \quad (2.111)$$

$$\Gamma_M = 1 + g_2(M) + E_1 \quad (2.112)$$

$$G_M = g_1(M)(u_e \delta)_1 + \frac{\tilde{u}_{eM}}{\lambda} + D_1(u_e \delta)_{M-1} \\ - E_1(u_e \delta)_{M-2} + \sum_{j=1}^{M-2} [(u_e \delta)_j D_k + E_k((u_e \delta)_{j+1} - (u_e \delta)_{j-1})] \quad (2.113)$$

When $1 < i < M$, eq. (2.104) becomes

$$u_{ei} = \lambda G_i + \lambda \Gamma_i (u_e \delta)_i \quad (2.114)$$

$$\Gamma_i = 1 + 2E_1 \quad (2.115)$$

$$\begin{aligned}
G_i &= (u_e \delta)_1 g_1(i) + (u_e \delta)_M g_2(i) + \frac{\tilde{u}_{e_i}}{\lambda} \\
&+ D_1(u_e \delta)_{i-1} - E_1(u_e \delta)_{i-2} + D_1(u_e \delta)_{i+1} \\
&- E_1(u_e \delta)_{i+2} + \sum_{j=1}^{i-2} [(u_e \delta)_j D_k + E_k((u_e \delta)_{j+1} - (u_e \delta)_{j-1})] \\
&+ \sum_{j=i+2}^M [(u_e \delta)_j D_k - E_k((u_e \delta)_{j+1} - (u_e \delta)_{j-1})]
\end{aligned} \tag{2.116}$$

$$\begin{aligned}
G_i &= (u_e \delta)_1 g_1(i) + (u_e \delta)_M g_2(i) + \frac{\tilde{u}_{e_i}}{\lambda} \\
&+ \sum_{j=1}^{i-1} [(u_e \delta)_j D_k + E_k((u_e \delta)_{j+1} - (u_e \delta)_{j-1})] \\
&+ \sum_{j=i+1}^M [(u_e \delta)_j D_k - E_k((u_e \delta)_{j+1} - (u_e \delta)_{j-1})] \\
&- 2E_1(u_e \delta)_i
\end{aligned} \tag{2.117}$$

2.8 Boundary Conditions

The boundary conditions are

$$F(\xi, \eta) = \frac{u(x, y)}{u_e(x)} = 0 \quad \text{when } \eta = 0$$

$V(0) = V_w$ where $V_w < 0$ for suction and $V_w > 0$ for blowing

$$\frac{\partial Q(\xi, 0)}{\partial \eta} = q_w \quad \text{or} \quad Q(\xi, 0) = C T_{adb}$$

where $q_w = 0$ if the wall is insulated, $C > 1.0$ for heating, $C < 1.0$ for cooling, and $C = 1.0$ for an insulated wall. As $\eta \rightarrow \infty$,

$$F(\xi, \eta) = \frac{u(x,y)}{u_e(x)} = 1 \quad \text{and} \quad Q(\xi, \eta) = \frac{T(x,y)}{T_e(x)} = 1$$

The nonlinear boundary condition on β is derived as follows. We start with eq. (2.48), which is repeated here

$$2\xi F_\xi + V_\eta + F = 0 \quad (2.118)$$

We add $Q + 2\xi Q_\xi$ to both sides of eq. (2.118) and obtain

$$2\xi F_\xi + V_\eta + F + Q + 2\xi Q_\xi = Q + 2\xi Q_\xi$$

or

$$V_\eta + Q + 2\xi Q_\xi = Q - F + 2\xi(Q_\xi - F_\xi) \quad (2.119)$$

Integrating eq. (2.119) from $\eta = 0$ to $\eta = \eta_e$ yields

$$V \Big|_0^{\eta_e} + \int_0^{\eta_e} (Q + 2\xi Q_\xi) d\eta = \int_0^{\eta_e} (Q - F) d\eta + 2\xi \frac{\partial}{\partial \xi} \int_0^{\eta_e} (Q - F) d\eta \quad (2.120)$$

Using eq. (2.62), we find that eq. (2.120) tends to

$$V - V(0) + K(\eta_e) = \frac{\sqrt{Re} \delta \rho_e u_e}{\sqrt{2\xi}} + 2\xi \frac{d}{d\xi} \left[\frac{\sqrt{Re} \delta \rho_e u_e}{\sqrt{2\xi}} \right] \quad (2.121)$$

as $\eta_e \rightarrow \infty$, where

$$K(\eta_e) = \int_0^{\eta_e} (Q + 2\xi Q_\xi) d\eta \quad (2.122)$$

$$V(0) = V_w \quad (2.123)$$

Carrying out the differentiation in eq. (2.121) yields

$$V - V_w + K(\eta_e) = \sqrt{Re} \left[\frac{\delta \rho_e u_e}{\sqrt{2\xi}} + \frac{2\xi}{\sqrt{2\xi}} \frac{d}{d\xi} (\delta \rho_e u_e) - \frac{\xi}{\sqrt{2}} \xi^{-3/2} \delta \rho_e u_e \right] \quad (2.124)$$

which can be rewritten as

$$V + K(\eta_e) = V_w + \sqrt{2\xi} \frac{d}{d\xi} (\rho_e u_e \delta) \quad (2.125)$$

The pressure-gradient parameter β is defined as

$$\beta = \frac{2\xi}{u_e} \frac{du_e}{d\xi} \quad (2.126)$$

Using a three-point backward-differencing scheme, as in eq. (2.51), we rewrite eq. (2.126) as

$$\beta_i u_{e_i} = 2\xi_i [a_0 u_{e_i} + a_1 u_{e_{i-1}} + a_2 u_{e_{i-2}}] \quad (2.127)$$

Solving eq. (2.127) for u_{e_i} , yields

$$u_{e_i} = - \frac{2\xi_i [a_1 u_{e_{i-1}} + a_2 u_{e_{i-2}}]}{2\xi_i a_0 - \beta_i} = \lambda G_i + \lambda \Gamma_i (u_e \delta)_i \quad (2.128)$$

on account of eq. (2.114). Solving eq. (2.128) for $(u_e \delta)_i$ yields

$$(u_e \delta)_i = - \frac{G_i}{\Gamma_i} - \frac{2\xi_i [a_1 u_{e_{i-1}} + a_2 u_{e_{i-2}}]}{\lambda (2\xi_i a_0 - \beta_i) \Gamma_i} \quad (2.129)$$

Using the three-point backward-differencing scheme defined in eq. (2.51), we rewrite eq. (2.125) as

$$V + K(\eta_e) - V_w = \sqrt{2\xi_i} [(\rho_e u_e \delta)_i a_0 + a_1(\rho_e u_e \delta)_{i-1} + a_2(\rho_e u_e \delta)_{i-2}] \quad (2.130)$$

Substituting eq. (2.129) into eq. (2.130), we obtain

$$V + K(\eta_e) - V_w = \sqrt{2\xi_i} a_0 \rho_{e_i} \left[-\frac{G_i}{\Gamma_i} - \frac{2\xi_i(a_1 u_{e_{i-1}} + a_2 u_{e_{i-2}})}{\lambda \Gamma_i (2\xi_i a_0 - \beta_i)} \right] + \sqrt{2\xi_i} [a_1(\rho_e u_e \delta)_{i-1} + a_2(\rho_e u_e \delta)_{i-2}] \quad (2.131)$$

which can be rewritten as

$$V + \phi_1 + \frac{\phi_2}{2\xi_i a_0 - \beta_i} = 0 \quad (2.132)$$

where

$$\phi_1 = K(\eta_e) - V_w + \frac{\sqrt{2\xi_i} a_0 \rho_{e_i} G_i}{\Gamma_i} - \sqrt{2\xi_i} [a_1(\rho_e u_e \delta)_{i-1} + a_2(\rho_e u_e \delta)_{i-2}] \quad (2.133)$$

$$\phi_2 = \frac{(2\xi_i)^{3/2} a_0 (a_1 u_{e_{i-1}} + a_2 u_{e_{i-2}}) \rho_{e_i}}{\lambda \Gamma_i} \quad (2.134)$$

Finally, we rewrite eq. (2.132) as

$$V(2\xi_i a_0 - \beta_i) + \phi_1(2\xi_i a_0 - \beta_i) + \phi_2 = 0 \quad (2.135)$$

or

$$V\beta_i + \phi_1\beta_i - 2\xi_i a_0 V - \phi_2 - 2\xi_i a_0 \phi_1 = 0 \quad (2.136)$$

2.9 Stability Problem

We consider the linear two-dimensional quasiparallel stability of the mean flow calculated by using the interacting boundary-layer formulation. We assume that the specific heats and Prandtl number are constant. Because we are limiting the calculations to subsonic flows, this assumption has a small effect on the accuracy of the stability results. Moreover, the viscosity and thermal conductivity coefficients μ and κ are assumed to be functions of temperature only. Because Pr and C_p^* are constant, $\kappa = \mu$.

To derive the stability equations, we superimpose two-dimensional disturbances on the mean flow calculated by using the interacting boundary-layer formulation to obtain the total-flow quantities

$$\bar{\rho} = \rho_m(y) + \rho(x,y,t) \quad (2.137)$$

$$\bar{u} = u_m(y) + u(x,y,t) \quad (2.138)$$

$$\bar{v} = v(x,y,t) \quad (2.139)$$

$$\bar{p} = p_m(y) + p(x,y,t) \quad (2.140)$$

$$\bar{\mu} = \mu_m(y) + \mu(x,y,t) \quad (2.141)$$

$$\bar{\lambda} = \lambda_m(y) + \lambda(x,y,t) \quad (2.142)$$

$$\bar{T} = T_m(y) + T(x,y,t) \quad (2.143)$$

where λ and μ appear in the definition of the bulk-viscosity coefficient k as

$$k = \lambda + \frac{2}{3} \mu$$

The subscript m refers to mean-flow quantities and the overbar refers to total-flow quantities.

Since $\bar{\mu}$ and $\bar{\lambda}$ are functions of temperature only, we have

$$\lambda = \frac{d\lambda_m}{dT_m} T = \lambda'_m(T_m)T \quad \text{and} \quad \mu = \frac{d\mu_m}{dT_m} T = \mu'_m(T_m)T \quad (2.144)$$

Substituting eqs. (2.137)-(2.144) into the two-dimensional compressible Navier-Stokes equations, subtracting the mean-flow quantities, and linearizing the resulting equations, we obtain

$$\frac{\partial \rho}{\partial t} + u_m \frac{\partial \rho}{\partial x} + \frac{d\rho_m}{dy} v + \rho_m \left(\frac{\partial u}{\partial x} + \frac{\partial v}{\partial y} \right) = 0 \quad (2.145)$$

$$\begin{aligned} \rho_m \left(\frac{\partial u}{\partial t} + u_m \frac{\partial u}{\partial x} + \frac{du_m}{dy} v \right) + \frac{\partial p}{\partial x} \\ - \frac{1}{R} \frac{\partial}{\partial x} \left[r\mu_m \frac{\partial u}{\partial x} + m\mu_m \frac{\partial v}{\partial y} \right] \\ - \frac{1}{R} \frac{\partial}{\partial y} \left[\mu_m \left(\frac{\partial u}{\partial y} + \frac{\partial v}{\partial x} \right) + \mu \frac{du_m}{dy} \right] = 0 \end{aligned} \quad (2.146)$$

$$\begin{aligned} \rho_m \left(\frac{\partial v}{\partial t} + u_m \frac{\partial v}{\partial x} \right) + \frac{\partial p}{\partial y} - \frac{1}{R} \frac{\partial}{\partial y} \left[r\mu_m \frac{\partial v}{\partial y} + m\mu_m \frac{\partial u}{\partial x} \right] \\ - \frac{1}{R} \frac{\partial}{\partial x} \left[\mu_m \left(\frac{\partial v}{\partial x} + \frac{\partial u}{\partial y} \right) + \mu \frac{du_m}{dy} \right] = 0 \end{aligned} \quad (2.147)$$

$$\begin{aligned} \rho_m \left(\frac{\partial T}{\partial t} + u_m \frac{\partial T}{\partial x} + \frac{dT_m}{dy} v \right) - (\gamma - 1)M_\infty^2 \left(\frac{\partial p}{\partial t} + u_m \frac{\partial p}{\partial x} \right) \\ = \frac{\mu_m}{RPr} \left(\frac{\partial^2 T}{\partial x^2} + \frac{\partial^2 T}{\partial y^2} \right) + \frac{1}{RPr} \frac{\partial \mu}{\partial y} \frac{dT_m}{dy} \\ + \frac{1}{RPr} \frac{d\mu_m}{dy} \frac{dT}{dy} + \frac{(\gamma - 1)M_\infty^2 \phi}{R} + \frac{\mu}{RPr} \frac{d^2 T_m}{dy^2} \end{aligned} \quad (2.148)$$

where

$$\phi = 2\mu_m \left[\left(\frac{\partial u}{\partial y} + \frac{\partial v}{\partial x} \right) \frac{du_m}{dy} \right] + \mu \left(\frac{du_m}{dy} \right)^2 \quad (2.149)$$

$$m = \frac{\lambda_m}{\mu_m}, r = 2 + m, \quad (2.150)$$

$$R = \frac{U_\infty^* \delta_0^*}{v_\infty^*}, \quad \delta_0^* = \sqrt{\frac{v_\infty^* x^*}{U_\infty^*}}. \quad (2.151)$$

The linearized equation of state for a perfect gas is

$$\gamma M_\infty^2 p = \rho_m T + \rho T_m$$

or

$$\rho = (\gamma M_\infty^2 p - \rho_m T) / T_m \quad (2.152)$$

The boundary conditions are

$$u = v = 0, T = 0 \quad \text{at } y = 0 \quad (2.153)$$

$$u, v, p, T \rightarrow 0 \quad \text{as } y \rightarrow \infty \quad (2.154)$$

We seek a quasiparallel solution of eqs. (2.145)-(2.148), (2.153), and (2.154) in the normal-mode form

$$q = \hat{q}(y) \exp\{i \int \alpha dx - i\omega t\} + \text{complex conjugate} \quad (2.155)$$

where q stands for (u, v, p, T) , α is the complex wavenumber, and ω is the frequency. For a spatial-stability analysis, α is complex and ω is real, whereas for a temporal-stability analysis ω is complex and α is real. Here, we present results for the spatial-stability case and determine ω from the nondimensional frequency F as $\omega = FR$.

Dropping the hat from \hat{q} for convenience and defining

$$\Omega = \omega - \alpha u_m \quad (2.156)$$

we find that α is governed by the eigenvalue problem

$$Dv = -i\alpha u + \frac{DT_m}{T_m} v + \frac{i\Omega p}{\rho_m} - \frac{i\Omega T}{T_m} \quad (2.157)$$

$$\begin{aligned} D^2 u = & \left(\frac{-i\rho_m \Omega R}{\mu_m} + r\alpha^2 \right) u - \left(\frac{\mu'_m DT_m}{\mu_m} Du \right) \\ & + \left[\frac{\rho_m R Du_m}{\mu_m} - i\alpha \frac{\mu'_m DT_m}{\mu_m} \right] v - i(1+m)\alpha Dv \\ & + \frac{iR\alpha}{\mu_m} p - \left[\frac{Du_m}{\mu_m} D(\mu'_m) + \frac{D^2 u_m}{\mu_m} \mu'_m \right] T - \frac{\mu'_m}{\mu_m} Du_m DT \end{aligned} \quad (2.158)$$

$$\begin{aligned} \chi_0 Dp = & -i\alpha \left(r \frac{DT_m}{T_m} + \frac{2\mu'_m DT_m}{\mu_m} \right) u - i\alpha Du \\ & + \left(\frac{iR\Omega}{\mu_m T_m} - \alpha^2 + r \frac{D^2 T_m}{T_m} + \frac{r\mu'_m (DT_m)^2}{\mu_m T_m} \right) v \\ & + i \frac{r}{\rho_m} \left[\Omega \left(\frac{DT_m}{T_m} + \frac{\mu'_m}{\mu_m} DT_m \right) - \alpha Du_m \right] p \\ & + \left[i(\alpha Du_m) \left(\frac{\mu'_m}{\mu_m} + \frac{r}{T_m} \right) - \frac{ir\Omega \mu_m}{\mu_m T_m} DT_m \right] T - \frac{ir\Omega}{T_m} DT \end{aligned} \quad (2.159)$$

$$\begin{aligned} D^2 T = & -2(\gamma-1)M_\infty^2 Pr Du_m Du + \left[RPr \frac{\rho_m DT_m}{\mu_m} - 2i(\gamma-1)M_\infty^2 Pr \alpha Du_m \right] v \\ & + i(\gamma-1)M_\infty^2 Pr R \frac{\Omega}{\mu_m} p + \left[-iRPr \Omega \frac{\rho_m}{\mu_m} + \alpha^2 - \frac{(DT_m)^2 \mu_m''}{\mu_m} \right. \\ & \left. - \mu'_m \frac{D^2 T_m}{\mu_m} - (\gamma-1) M_\infty^2 Pr \frac{\mu'_m}{\mu_m} (Du_m)^2 \right] T - 2 \frac{\mu'_m DT_m}{\mu_m} DT \end{aligned} \quad (2.160)$$

$$u = v = T = 0 \quad \text{at } y = 0 \quad (2.161)$$

$$u, v, p, T, \rightarrow 0 \quad \text{as } y \rightarrow \infty \quad (2.162)$$

where

$$D = \frac{d}{dy}, \chi_0 = \frac{R}{\mu_m} - ir \frac{\Omega}{p_m}, \text{ and } p_m = \frac{1}{\gamma M_\infty^2} \quad (2.163)$$

For a given mean flow, ω , and R , we solve for the eigenvalue α and the eigenfunctions, and then determine the amplification factor from

$$N = - \int_{R_0}^R 2\alpha_i dR \quad (2.164)$$

where R_0 corresponds to the location where the disturbance starts first to grow and α_i is the imaginary part of α . The eigenvalue problem is solved by using the IMSL second-order finite-difference subroutine DBVPFD [43]. In all cases, unless otherwise specified, the results are for the most dangerous frequency, defined to be the one that results in an N factor of 9.0 in the shortest distance.

3. Results and Discussion

A parametric study of the effect of a hump on the stability of laminar boundary layers over an airfoil was performed for different Mach numbers and heights and locations of the hump. The airfoil used in this study is EQH1260 (Fig. 1), which was extensively studied in the United Kingdom in the forties. The Reynolds number based on the chord is 6.5×10^6 . The pressure-coefficient distributions over the clean airfoil were calculated using an Euler code for different Mach numbers. In Fig. 2, we show the pressure distributions for the Mach numbers 0.14, 0.50, and 0.65, respectively. We note that the minimum pressure is located at approximately 75% of the chord. The cubic hump shown in Fig. 3 was added to the airfoil. Then, thin airfoil theory was used to calculate the total inviscid velocity over the modified airfoil.

In this work, we use linear stability theory to identify the characteristics of permissible disturbances, including the eigenfunctions (disturbance waveforms), wavelengths, frequencies, orientations, amplification rates, and amplification factors. The amplification factor is defined as the natural logarithm of the ratio of the disturbance amplitude at any point in the boundary layer to the disturbance amplitude A_0 at the neutral stability point. It can be computed by integrating the local amplification rates along a prescribed path.

When correlated with experimental transition data, linear stability may play an important role as a transition prediction method in the design of laminar-flow wings. A

transition-prediction method, now known as the “exp(N) method”, was first proposed, independently, by Smith and Gamberoni [32] and Van Ingen [33] in 1956. The basis of the method is the premise that transition is caused by a certain amount of amplification of initially small disturbances as they propagate downstream in the boundary layer. For low-speed two-dimensional flows on smooth surfaces, Smith found that the calculated N factor is near 9 (an amplification of about 8000) at the onset of transition. Nayfeh, Ragab and Al-Maaitah [13] studied the stability of the flow around hump and dip imperfections. They correlated their results with the experimental data of Walker and Greening [23]. The observed transition locations correspond to amplification factors varying between 7.4 and 10, consistent with previous results for flat plates. Therefore, the “exp(n) method” can be used for correlating transition and evaluating natural laminar flow and laminar flow control over smooth surfaces as well as surfaces with imperfections.

In this work, an N-factor of 9 was used to correlate transition from laminar to turbulent flow over an airfoil with a hump. We refer to the frequency that produces an N-factor of 9 in the shortest distance as the most dangerous frequency. If the N-factor does not reach 9, we refer to the frequency that produces the largest N-factor as the most dangerous frequency.

In this thesis, the following abbreviations are used:

1. Considered heights of the hump: h_0 no hump, $h_1 = \frac{h_1^*}{c^*} = 5.0 \times 10^{-4}$, $h_2 = \frac{h_2^*}{c^*} = 7.5 \times 10^{-4}$, $h_3 = \frac{h_3^*}{c^*} = 8.0 \times 10^{-4}$, $h_4 = \frac{h_4^*}{c^*} = 9.0 \times 10^{-4}$, $h_5 = \frac{h_5^*}{c^*} = 1.0 \times 10^{-3}$, and $h_6 = \frac{h_6^*}{c^*} = 1.2 \times 10^{-3}$,
2. Considered locations of the hump: L1 for $x_e = 0.2$ to $x_r = 0.3$, L2 for $x_e = 0.3$ to $x_r = 0.4$, and L3 for $x_e = 0.4$ to $x_r = 0.5$.

3.1 Clean Airfoil

We calculated the mean flow for the clean airfoil using the given pressure distributions for the different Mach numbers and a conventional boundary-layer solver. The solution breaks down near $x = 0.75$ because the boundary layer separates there. Reported experimental data [26] indicate that transition occurs at this point of minimum pressure and the flow is turbulent beyond this point. Then, we fed the calculated mean-flow profiles into a two-dimensional compressible spatial stability code. We swept the frequency from $F = 25 \times 10^{-6}$ to $F = 55 \times 10^{-6}$. In Figs. 4-6, we show the variation of the amplification factor with the streamwise position for several frequencies for the Mach numbers 0.14, 0.50, and 0.65, respectively. In all cases, the N-factor remains below 9 up to $x = 0.75$, then it increases dramatically, indicating that the boundary layer undergoes transition to turbulent flow as indicated by the experiments. We note that, for each Mach number, the peak of the N-factor moves upstream as the frequency increases. When $M = 0.14$, the maximum value of the N-factor increases as F increases from 25×10^{-6} to 30×10^{-6} and then it decreases as the frequency increases further. For $M = 0.50$ and 0.65, the maximum value of the N-factor decreases as the the frequency increases from 25×10^{-6} to 55×10^{-6} . The maximum N-factor for the Mach number 0.14 is 7.21, and it corresponds to $F = 30 \times 10^{-6}$. The maximum N-factors for the Mach numbers 0.50 and 0.65 are 5.41 and 3.97, respectively, and they correspond to $F = 25 \times 10^{-6}$. Moreover, we note that compressibility has a stabilizing influence on the flow in that, for a given frequency and streamwise position, the amplification factor decreases as the Mach number increases.

3.2 Influence of the Hump

3.2.1 Mean-Flow Characteristics

In Fig. 7, we show the displacement thickness for a clean airfoil when $M = 0.14$, $M = 0.50$, and $M = 0.65$. The hump should not be large so as to produce a breakaway separation. In such a case, one needs to use a Navier-Stokes solver. In this work, we consider only hump heights of the order of the displacement thickness so that we can calculate the mean flow using interacting boundary layers.

The mean flow was calculated for different heights and locations of the hump and different Mach numbers. In Fig. 8, we show variation of the skin-friction coefficient C_f with streamwise position for three humps when $M = 0.14$, $Re = 6.5 \times 10^6$, $x_c = 0.20$ and $x_r = 0.30$. Humps h_3 and h_4 do not produce any separation while hump h_5 corresponds to incipient separation. In Fig. 9, we show variation of C_f with streamwise position for the same three humps and the same location when $M = 0.50$. At this Mach number, hump h_5 produces a small separation bubble, while hump h_4 corresponds to incipient separation. In Fig. 10, we show variation of C_f with streamwise position for the same three humps and the same location when $M = 0.65$. In this case, humps h_4 and h_5 produce separation bubbles, while hump h_3 corresponds to incipient separation. It is clear from Figs. 8-10 that the size of the separation bubble increases when the hump height increases and/or the Mach number increases. In other words, increasing either the hump height or the Mach number increases the size of the separation bubble.

Moving the hump downstream to location L2 (i.e., $x_c = 0.30$ and $x_r = 0.40$), we calculated C_f for the same three heights and Mach numbers. In Fig. 11, we show variation of C_f with streamwise position. Then, we moved the hump to location L3 (i.e., $x_c = 0.40$ and $x_r = 0.50$) and repeated the calculations. The resulting variation of C_f with streamwise position is shown in Fig. 12. Comparing Figs. 11 and 12, we conclude that moving the hump downstream, while

keeping both the hump height and width and the Mach number fixed, increases the size of the separation bubble.

It is clear from Figs. 8-12 that separation occurs after the center of the hump. One might expect that moving the hump downstream, without changing its height and the Mach number, reduces the separation bubble and therefore the interaction effects due to the fact that the hump is embedded in a thicker boundary layer. This is true for a uniform flow over a flat plate, as shown by Al-Maatiah [17]. In our results, it is not the case because of variations in the pressure. In fact, transition occurs on the clean airfoil very close to the location of minimum pressure, which is located downstream close to the trailing edge. Therefore, placing the hump downstream increases the size of the separation bubble and in turn results in premature transition.

The upstream influence of the hump is weaker than the downstream influence. In fact, the upstream influence decays exponentially, while the downstream influence decays algebraically as shown by Smith [44] for small humps. In Fig. 13, we show variation of C_f with streamwise position for the clean airfoil and hump h_5 located at L1 when $M = 0.50$.

3.2.2 Stability Characteristics

The effect of the hump height and Mach number for a fixed hump location on the growth rates and therefore on the amplification factors of two-dimensional waves was studied for several nondimensionless frequencies $F = \frac{\omega^* v^*}{U^*}$. The hump increases the growth rate up to x_e , decreases the growth rate in the interval $(x_e, x_e + \frac{1}{2}b)$, increases the growth rate again in the interval $(x_e + \frac{1}{2}b, x_r)$, where b is the width of the hump (i.e., $b = x_r - x_e$).

3.2.2.1 Location L1

For a given Mach number and hump height and location, we performed the calculations for several frequencies and found the most dangerous frequency. In Table 1, we list the most dangerous frequency for each Mach number and hump location. It is clear that the most dangerous frequency decreases as the Mach number is increased for a fixed location.

In Fig. 14, we show variation of the N-factor for the most dangerous frequency with streamwise position for h_3 at $M = 0.14$, $M = 0.50$, and $M = 0.65$. It is clear that compressibility stabilizes the flow; the amplification factor of the most dangerous frequency decreases at each streamwise position as the Mach number increases. Assuming that $N = 9$ corresponds to transition, we conclude from Fig. 14 that h_3 produces transition at $x = 0.308$ when $M = 0.14$. Note that when $M = 0.50$ and $M = 0.65$ transition is not produced upstream of the minimum-pressure location at $x = 0.75$.

In Fig. 15, we show variation of the N-factor for the most dangerous frequency with streamwise position for h_4 at the same Mach numbers. This hump produces transition approximately at $x = 0.300$ when $M = 0.14$ and at $x = 0.313$ when $M = 0.50$ but does not produce transition upstream of the minimum pressure location when $M = 0.65$. For the larger hump h_5 , it follows from Fig. 16 that transition occurs upstream of the location of minimum pressure at all three Mach numbers considered. Comparing Figs. 14-16, we conclude that the transition location moves upstream as the hump height increases. These results are consistent with the empirical correlations of Fage [26] and the theoretical calculations of Masad and Nayfeh [21] for a hump mounted on a flat plate.

In Figs. 17-19, we show variation of the N-factor for the most dangerous frequency with streamwise position for several heights at location L1 and for the same three Mach numbers. We note that the critical heights for transition are $h = 7.5 \times 10^{-4}$ when $M = 0.14$, $h = 9.0 \times 10^{-4}$ when $M = 0.50$, and $h = 1.0 \times 10^{-3}$ when $M = 0.65$. It is clear that increasing the hump height results in an increase in the N-factor for all three Mach numbers. We note that, at the same location, the hump height that produces transition increases as the Mach number increases,

which reflects the overall stabilizing influence of compressibility. Above a hump height of approximately 1.0×10^{-3} , the transition location is within 0.03 of the chord for all three Mach numbers, indicating that compressibility has a negligible influence on the transition location for large humps.

3.2.2.2 Location L2

In Fig. 20, we show variation of the N-factor with streamwise position for the same three Mach numbers for h_3 located at L2. Again compressibility is stabilizing. Whereas this hump produces premature transition when $M = 0.14$ and 0.5 , it does not produce premature transition for $M = 0.65$. Moreover, transition moves slightly downstream as M increases from 0.14 to 0.50 . Comparing Figs. 14 and 20, we find that the transition location when $M = 0.14$ has moved to $x = 0.390$ and the most dangerous frequency has decreased from $F = 45 \times 10^{-6}$ to $F = 40 \times 10^{-6}$. The decrease in the most dangerous frequency as the hump is moved downstream is consistent with the results in Table 1. Furthermore, we note from Table 1 that this most dangerous frequency decreases as the Mach number increases. It follows from Figs. 14 and 20 that, when $M = 0.50$, whereas hump h_3 does not produce transition upstream of the minimum pressure location when placed at L1, it does so when placed at L2. Thus, a certain height that does not produce transition when placed at one location might produce transition when placed at a downstream location. In other words, the critical height for transition decreases as the hump is moved downstream. In Figs. 21 and 22, we show variation of the N-factor for the same three considered Mach numbers for humps h_4 and h_5 , respectively. It follows from these figures and Table 3 that h_4 and h_5 produce premature transition at all Mach numbers and that above $h_4 = 9.0 \times 10^{-4}$, transition occurs at all three Mach numbers considered. In all cases, the transition location moves downstream as the Mach number increases.

3.2.2.3 Location L3

In Figs. 23-25, we show variation of the N-factor for the same three Mach numbers and same three heights. The most dangerous frequency decreases as the hump is moved further downstream and/or the Mach number is increased. Moreover, we note that compressibility is stabilizing. It is clear from these figures that the transition locations are downstream of those corresponding to location L2. Above $h_4 = 9.0 \times 10^{-4}$, transition occurs at all three Mach numbers, $M = 0.14, 50$, and 0.65 . Again, transition moves downstream as the Mach number increases, as shown in Table 4. It is also clear from Table 4 that, at a given Mach number, the transition location moves upstream as the hump height increases.

Comparing Figs. 23-25 with Figs. 20-22 and Figs. 17-19, we conclude that for a given hump height and Mach number, the peak amplification factor increases and moves further downstream as the hump location moves downstream.

3.3 Boundary-Layer Control with Suction

It has long been recognized that application of suction to laminar boundary layers is an effective tool for delaying transition and hence reducing drag. Suction influences the stability of laminar boundary layers through two important effects. First, it reduces the boundary-layer thickness which makes the boundary layer less prone to becoming turbulent. Second, it changes the shape of the velocity profiles by making them fuller and hence increases the critical Reynolds number, decreases the growth rates which results in smaller N-factors, and narrows the band of frequencies receiving amplification.

For the case of continuous suction, the resulting surfaces may not be sufficiently rigid to carry the aerodynamics loads. Hence, application of suction through multiple strips, although more difficult to analyze, is more attractive for structural considerations. Reed and Nayfeh

[45], Nayfeh and Reed [48-49], Reynolds and Saric [50], and Masad and Nayfeh [46] showed that, for the case of smooth flat-plate boundary layers, suction applied through multiple discrete strips can be as effective as suction applied continuously through a much wider surface. In this work, we show that this conclusion is true for boundary-layer flows over an airfoil with imperfections.

To account for the upstream influence of suction strips, we calculated the mean flow by using interacting boundary layers. Conventional (parabolic) boundary layers fail to account for this influence. Reed and Nayfeh [45] showed that, for incompressible flow, the growth rates calculated using profiles obtained with conventional boundary layers are different from those calculated using profiles obtained with interacting boundary layers. The difference between these growth rates increases with increasing suction level. Masad and Nayfeh [46] compared the growth rates for both incompressible and compressible flows for a single strip. They showed that the growth rates drop sharply at the upstream left end of the strip when the mean flow is calculated using conventional boundary layers, whereas they vary smoothly when the mean flow is calculated using interacting boundary layers. Moreover they showed that conventional boundary layers underpredict the minimum. Far downstream of the strip, the growth rates corresponding to both mean-flow profiles approach each other. Although the differences between the growth rates calculated using the conventional and interacting boundary-layer formulations are significant near the suction strips, the difference between the N-factors calculated using both approaches is small.

We considered the flow over the airfoil for hump h_5 located at L3 when $M = 0.14$. We chose this location because it produces N-factors that are larger than those of the other locations. The calculations were performed by using the following steps:

1. We chose a suction strip that extends from $x = 0.37$ to $x = 0.54$ and selected a suction level of $C_q = 1.5 \times 10^{-4}$. Then, we calculated the mean flow using interacting boundary layers.

2. We fed the mean-flow profiles into the stability code and swept the frequency from $F = 25 \times 10^{-6}$ to $F = 55 \times 10^{-6}$. In Fig. 26, we show variation of the N-factor with streamwise position for several frequencies. It is clear that this suction configuration delays transition to the location of minimum pressure because none of the amplification factors reaches $N = 9$. The frequency that produces the largest N-factor is $F = 35 \times 10^{-6}$, which is the same as the most dangerous frequency in the absence of suction. This might not be the case for other locations and Mach numbers.

3. After determining the most dangerous frequency, we varied the location of the suction strip while we kept its width and suction level fixed (i.e., $\Delta x = 0.17$ and $C_q = 1.5 \times 10^{-4}$). The locations we considered for the upstream end of the strip were $x = 0.27$, $x = 0.37$, and $x = 0.42$. In Fig. 27, we show variation of the N-factor with streamwise position for the three locations of the suction strip. It is clear that all three strips delay transition to the location of minimum pressure. Moving the suction strip upstream reduces the first local maximum but increases the second local maximum. Moreover, configuration S_3 is the optimum one because it produces the smallest global maximum. In fact, it eliminates the second local maximum. Because the N-factor is brought down to zero, one can reduce the suction level or strip width and hence the total flow rate and yet control the boundary layer.

4. We reduced the strip width to $\Delta x = 0.08$, located its upstream end at $x = 0.45$, and studied the effect of the suction level on the N-factor. In Fig. 28, we show variation of the N-factor with streamwise position for the three suction levels $C_q = 1.5 \times 10^{-4}$, $C_q = 3.0 \times 10^{-4}$, and $C_q = 4.5 \times 10^{-4}$. Comparing curve b of Fig. 27 with curve b of Fig. 28, we conclude that decreasing the strip width to about one-half and keeping $C_q = 1.5 \times 10^{-4}$ is not a good idea because the flow will undergo premature transition. It is clear that increasing the suction level at this location does not affect the first peak but drastically reduces the second peak.

5. We kept the width of the suction strip equal to $\Delta x = 0.08$, chose a suction level of $C_q = 4.5 \times 10^{-4}$, and varied the location of the strip. The locations considered for the upstream end of the strip are $x = 0.34$, $x = 0.37$, $x = 0.40$, $x = 0.45$, and $x = 0.49$. In Fig 29, we show variation of the N-factor with streamwise position for these suction configurations. Strips S_2 , S_3 , and S_4 delay transition to the location of minimum pressure, whereas strips S_1 and S_5 do not. Strip S_5 is placed almost downstream of the hump and consequently it has a negligible effect on the upstream local maximum and a small effect on the second local maximum, which is decreased only to $N = 12.3$. On the other hand, strip S_1 is placed almost upstream of the hump and consequently it reduces the first local maximum significantly but does not decrease the second local maximum below $N = 9$. Strip S_4 , which starts at the middle of the hump, has a negligible effect on the first local maximum but reduces significantly the second local maximum. On the other hand, strip S_2 , which starts ahead of the hump and extends to its middle, reduces significantly both maxima. Finally, strip S_3 , which almost coincides with the hump, reduces slightly the first maximum and eliminates the second maximum. Therefore, it appears that the optimum location would extend slightly upstream of the hump and cover a large portion of the hump.

6. We divided the suction strip into two equal strips, while keeping the total width fixed (i.e., $\Delta x = 0.08$). The first strip extends from $x = 0.34$ to $x = 0.38$, while the second strip extends from either $x = 0.44$ to $x = 0.48$ or $x = 0.45$ to $x = 0.49$. In Fig. 30, we show variation of the N-factor with streamwise position for different suction levels and the two locations of the second strip. Configuration S_1 consists of one strip which starts upstream of the hump and ends slightly downstream of x_c , the start of the hump. This configuration reduces significantly the first maximum but does not reduce the second maximum below $N = 9$. We divided this strip into two, kept the suction level at $C_q = 4.5 \times 10^{-4}$, moved the second half downstream so that its upstream end coincides with the middle of the hump. The result is dramatic: all maxima decreased significantly, as evident from curve f . Consequently, multiple strips can be more effective than a single strip, in agreement with

the results of Masad and Nayfeh [46]. Then, we decreased the suction level in both strips from 4.5×10^{-4} to 3.0×10^{-4} and repeated the calculations. For this S_3 configuration, the maximum amplification factor is below 6. Next, we kept the suction level at 3.0×10^{-4} in both strips and moved the upstream end of the second strip slightly upstream from $x = 0.45$ to $x = 0.44$. As a result, the maximum amplification factor decreased from $N = 6.19$ to $N = 5.57$. Finally, we fixed the location of the second strip ($x = 0.44$ to $x = 0.48$) and decreased its suction level from 3×10^{-4} to 2×10^{-4} . The maximum amplification factor increased from $N = 5.57$ to $N = 7.48$, which is below $N = 9$. Therefore, it appears that configuration S_2 is near an optimum one.

3.4 Boundary-Layer Control with Heat Transfer

As do suction strips, a cooling strip has an upstream as well as a downstream influence. This influence is due to the abrupt change in the thermal boundary condition. Because conventional boundary layers are modeled by parabolic equations, they are not expected to account for the upstream influence and hence they are not expected to produce accurate mean flows and consequently growth rates. Masad and Nayfeh [46] compared growth rates for incompressible and compressible flows obtained using conventional and interacting boundary layers. They showed that the growth rates drop sharply at the upstream end of the strip when the mean flow is calculated using conventional boundary layers, whereas they vary smoothly when the mean flow is calculated using interacting boundary layers. Moreover, conventional boundary layers underpredict the minimum and overpredict the maximum of the growth rate. Far downstream of the strip, the growth rates corresponding to both mean-flow profiles approach each other. Although the differences between the growth rates calculated using conventional and interacting boundary-layer formulations are significant near the cooling strips, the differences between the N-factors calculated using both approaches are

small. In this work, we used interacting boundary layers to solve for the mean flow. For the same total energy the results show that, application of cooling through multiple strips with a higher wall temperature can be as effective as continuous cooling with a lower wall temperature.

We considered the flow over hump h_5 located at L3 for $M = 0.14$ as follows:

1. We chose a cooling strip extending from $x = 0.45$ to $x = 0.49$, chose the wall temperature $T_w/T_{ad} = 0.6$, and calculated the mean flow using interacting boundary layers.
2. We fed the mean-flow profiles into the stability code and swept the frequency from $F = 25 \times 10^{-6}$ to $F = 55 \times 10^{-6}$. In Fig. 31, we show variation of the N-factor with streamwise position for seven frequencies. It is clear that the chosen cooling strip delays transition to the location of minimum pressure. The maximum amplification factor is 7.95, corresponding to $F = 35 \times 10^{-6}$, which is the most dangerous frequency in the absence of cooling. This might not be the case for other locations and Mach numbers.
3. After determining the most dangerous frequency, we raised the temperature of the cooling strip from $T_w/T_{ad} = 0.6$ to $T_w/T_{ad} = 0.8$, kept its width fixed (i.e., $\Delta x = 0.04$), and varied its location. The locations considered for the upstream end are $x = 0.30$, $x = 0.34$, and $x = 0.38$. In Fig. 32, we show the effect of the cooling strip location on the N-factor. It is clear that the farther upstream the cooling strip is placed, the larger the decrease in the first local maximum is. The second local maximum is slightly affected. We note that all of these cooling strips are upstream of the hump.
4. We kept the width of the cooling strip $\Delta x_{cooling} = 0.04$, located its upstream end at $x = 0.34$, and raised its temperature T_w/T_{ad} from 0.8 to 0.9. In Fig. 33, we show variation of the N-factor with streamwise position. As expected, decreasing the cooling level increases the N-factor.

5. Having lowered the first local maximum, we added a second cooling strip of width $\Delta x = 0.04$, set its temperature at $T_w/T_{ad} = 0.8$, and varied its location. In Fig. 34, we show variation of the N-factor with streamwise position for five configurations. Configurations C_1 and C_2 reduce the second local maximum to $N = 6.10$ and $N = 5.85$, respectively, and hence delay transition to the location of minimum pressure. On the other hand, configurations C_3 , C_4 , and C_5 reduce the second local maximum but not enough to prevent premature transition. Clearly, the optimum location for the second strip is close to the start of the hump. In fact, configuration C_2 is the optimum of the five considered configurations; the strip starts at $x = 0.422$, which is slightly downstream of the upstream end ($x_e = 0.40$) of the hump.

6. Finally, we considered a heating strip with wall temperature $T_w/T_{ad} = 1.3$ and width $= 0.04$. Then, we varied the location of the strip: $x = 0.09$ to $x = 0.143$ and $x = 0.34$ to $x = 0.38$. We swept the frequency from $F = 25 \times 10^{-6}$ to $F = 55 \times 10^{-6}$. The most dangerous frequency is $F = 30 \times 10^{-6}$. In Fig. 35, we show the effect of heating on variation of the N-factor with streamwise position. It is clear that in the presence of an imperfection, a heating strip destabilizes the flow and results in premature transition.

4. Conclusions and Recommendations

4.1 Conclusions

The effect of surface imperfections in the form of a cubic hump on the stability of compressible and incompressible flows over the EQH1260 airfoil was analyzed. The mean flow was calculated using interacting-boundary-layer theory. Linear quasiparallel spatial stability theory was used to calculate the growth rates and mode shapes of two-dimensional disturbances. Then, the amplification factor was computed. A search for the most dangerous frequency for each Mach number and location of the imperfection was conducted (i.e., the frequency that produces an amplification factor of 9 in the shortest distance).

Based on the present investigations, we conclude that

1. The geometrical factors of the imperfection that govern the instability are its height, location, and width.
2. Increasing the imperfection height increases the growth rates and amplification factors for each hump location and Mach number.

3. Compressibility is stabilizing for all hump heights and locations.
4. Moving the imperfection downstream increases the amplification factor.
5. A hump height that does not produce transition at one location might produce transition at a downstream location.
6. For a given Mach number and hump location, the most dangerous frequency might change with suction.
7. For a given Mach number and hump location, the most dangerous frequency might change with heat transfer.
8. Application of cooling through multiple cooling strips with a higher wall temperature can be more efficient than cooling through a single strip with a lower wall temperature.
9. Application of suction through multiple strips with a lower suction level can be more efficient than suction through a single strip with a higher suction level.
10. Heating strips have a destabilizing effect on the whole mean flow in the presence of imperfections.

4.2 Recommendations

The present study needs to be extended so it accounts for:

1. Nonlinear effects (in view of the large growth rates encountered in separation regions).

2. Nonparallel effects.
3. Influence of imperfection shapes.
4. Influence of free-stream Reynolds number.
5. Receptivity to acoustic and free-stream disturbances.
6. Interaction between the instability mechanisms.

Experiments need to be conducted to provide detailed measurements of the pressure distributions, mean profiles, mode shapes, and growth rates that can be used to validate the theoretical results.

5. References

1. Schiller, L., Handbuch der Experimentel-Physik 4, Part 4, 1-207, Leipzig, 1932.
2. Tani, I., Hama, R., and Mituisi, S., "On the Permissible Roughness in the Laminar Boundary Layer," Aero. Res. Inst., Tokyo, Imp Univ. Rep. 199, 1940.
3. Goldstein, S., "A Note on Roughness," ARC RM 1763, 1936.
4. Fage, A. and Preston, J. H., "On Transition from Laminar to Turbulent Flow in the Boundary Layer," Proceedings of the Royal Society A 178, 1941, 201-227.
5. Aircraft Engineering, "First Laminar Flow Flight Tests Prove Drag Reduction Potential," 1992.
6. Holmes, B. J., O'bara, C. J., and Yip, L. P., "Natural Laminar Flow Flight Experiments on Modern Airplane Surface," NASA TP 2256, 1984.
7. O'bara, C. J. and Holmes, B. J., "Flight Measured Laminar Boundary-Layer Transition Phenomena Including Stability Theory Analysis," NASA TP 2417, 1985.

8. Holmes, B. J., O'bara C. J., Martin, G. L., and Domack, C. S., "Manufacturing Tolerances for Natural Laminar Flow Air Frame Surfaces," NASA CP 2413, 1986.
9. Van Dam, C. P. and Holmes, B. J., "Boundary-Layer Transition Effects on Airplane Stability and Control," *Journal of Aircraft* 25, 1988, 702-709.
10. Goldstein, M. E. and Hultgren, L. S., "Boundary-Layer Receptivity to Long-Wave Free-Stream Disturbances," *Annual Review of Fluid Mechanics* 21, 1989, 137-166.
11. Kerschen, E. J., "Boundary Layer Receptivity," AIAA Paper No. 89-1109, 1989.
12. Choudhari, M. and Street, C. L., "A Finite-Reynolds Number Approach for the Prediction of Boundary Layer Receptivity in Localized Regions," NASA Technical Memo No. 102781, 1991.
13. Nayfeh, A. H., Ragab, S. A., and Al-Maaitah, A. A., "Effect of Bulges on the Stability of Boundary Layers," *Physics of Fluids* 31, 1988, 796-806.
14. Cebeci, T. and Egan, D. A., "Prediction of Transition Due to Isolated Roughness," *AIAA Journal* 27, 1989, 870-875.
15. Al-Maaitah, A. A., Nayfeh, A. H., and Ragab, S. A., "Effect of Wall Cooling on the Stability of Compressible Subsonic Flows Over Smooth Two-Dimensional Backward-Facing Steps," *Physics of Fluids A2*, 1990, 381-389.
16. Al-Maaitah, A. A., Nayfeh, A. H., and Ragab, S. A., "Effect of Suction on the Stability of Subsonic Flows over Smooth Backward-Facing Steps," *AIAA Journal* 28, 1990, 1916-1924.
17. Al-Maaitah, A. A., "Effect of Suction and Cooling on the Stability of Subsonic and Supersonic Boundary Layers," Ph.D. Thesis, Virginia Polytechnic Institute and State University, Blacksburg, VA, 1989.

18. Bestek, H., Gruber, K. and Fasel, H., "Numerical Investigation of Unsteady Laminar Boundary Layer Flows Over Backward-Facing Steps," The Fourth Asian Congress of Fluid Mechanics, Hong Kong, August 19-23, 1989.
19. Elli, S. and van Dam, C. P., "The Influence of a Laminar Separation Bubble on Boundary-Layer Instability," AIAA Paper No. 92-3294, 1991.
20. Masad, J. A. and Nayfeh, A. H., "The Influence of Imperfections on the Stability of Subsonic Boundary Layers," Symposium in Honor of Eli Reshotko, Newport News, VA, July 28, 1991.
21. Masad, J. A. and Nayfeh, A. H., "Stability of Separating Boundary Layers," Fourth International Congress of Fluid Mechanics, Cairo, Egypt, April 28-30, 1992.
22. Nayfeh, A. H., Ragab, S. A., and Masad, J. A., "Effect of a Bulge on the Subharmonic Instability of Boundary Layers," Physics of Fluids A2, 1990, 937-948.
23. Walker, W. S. and Greening, J. R., R&M No. 5950, A.R.C., July 1942.
24. Hislop, G. S., R&M No. 6443, January 1943.
25. Walker, W. S. and Cox, R. J., R&M No. 6126, A.R.C., September 1942.
26. Fage, A., "The Smallest Size of Spanwise Surface Corrugation which Affect Boundary Layer Transition on an Airfoil," British Aeronautical Research Council 2120, 1943.
27. Carmichael, B. H., Whites, R. C., and Pfenninger, W., "Low Drag Boundary Layer Suction Experiment in Flight on the Wing Glove of a F-94A Airplane," Northrup Aircraft Rpt. No. NAI-57-1163 (BLC-101), 1957.

28. Carmichael, B. H. and Pfenninger, W., "Surface Imperfection Experiments on a Swept Laminar Suction Wing," Northrup Aircraft Rpt. No. NOR-59-454 (BLC-124), 1959.
29. Carmichael, B. H., "Surface Waviness Criteria for Swept and Unswept Laminar Suction Wings," Northrup Aircraft Rpt. No. NOR-59-438 (BLC-123), 1957.
30. Klebanoff, P. S. and Tidstrom, K. R., "Mechanism by which a Two-Dimensional Roughness Element Induces Boundary-Layer Transition," *Physics of Fluids* 15, 1972, 1173-1188.
31. Dovgal, A. V. and Kozlov, V. V., "Hydrodynamic Instability and Receptivity of Small Scale Separation Regions," in *Laminar-Turbulent Transition*, edited by D. Arnal and R. Michel, Springer-Verlag, Berlin, 1990, 523-431.
32. Smith, A. M. O. and Gamberoni, N., "Transition, Pressure Gradient and Stability Theory," Douglas Aircraft Co., El Segundo, CA, Rept. ES 26388, 1956.
33. Van Ingen, J. L., "A Suggested Semi-Empirical Method for the Calculation of the Boundary Layer Transition Region," Department of Aeronautical Engineering, University of Technology, Delft, The Netherlands, Rpt. VTH-74, 1956.
34. Davis, R. L., Carter, J. E., and Reshotko, E., "Analysis of Transitional Separation Bubbles on Infinite Swept Wings," *AIAA Journal* 3, 1987, 421-427.
35. Veldman, A. E. P., "New, Quasi-Simultaneous Method to Calculate Interacting Boundary Layers," *AIAA Paper No. 81-4010*, 1981.
36. Gleyzes, C., Cousteix, J., and Bonnet, J. L., "A Calculation Method of Leading Edge Separation bubbles," *Proceedings of the Second Symposium on Numerical and Physical Aspects of Aerodynamic Flows*, Springer-Verlag, January 1983,

37. Carter, J. E. and Vasta, V. N., "Analysis of Airfoil Leading Edge Separation Bubbles," NASA CR 165937, May 1982.
38. Davis, R. L. and Carter, J. E., "Analysis of Airfoil Transitional Separation Bubbles," AIAA Paper No. 84-1613, 1984.
39. Davis, R. T. and Werle, M. J., "Progress on Interacting Boundary-Layer Computations at High Reynolds Number," in Numerical and Physical Aspects of Aerodynamic Flows, edited by T. Cebeci, Springer-Verlag, Berlin, 1982, 187-192.
40. Davis, R. T., "A Procedure for Solving the Compressible Interacting Boundary-Layer Equations for Subsonic and Supersonic Flows," AIAA Paper No. 84-1614, 1984.
41. Ragab, S. A., Nayfeh, A. H., and Krishna, R. C., "Stability of Compressible Boundary Layers over a Smooth Backward-Facing Step," AIAA Paper No. 90-1449, 1990.
42. Krishna, R. C., "Effect of Surface Imperfections on the Stability of Laminar Boundary Layers," M.S. Thesis, Virginia Polytechnic Institute and State University, Blacksburg, VA, 1988.
43. Pereyra, V., "PASAV3: An Adaptive Finite Difference Fortran Program for First Order Nonlinear Ordinary Boundary Value Problems," in Lecture Notes in Computer Science, 76, edited by B. Childs, M. Scott, J. W. Daniel, E. Denman, and P. Nelson, Springer-Verlag, Berlin, 1976, 67-88.
44. Smith, F. T., "The Laminar Separation of an Incompressible Fluid Streaming Past a Smooth Surface," Proceedings of the Royal Society of London A 356, 1977, 443-463.
45. Reed, H. L. and Nayfeh, A. H., "Numerical-Perturbation Technique for Stability of Flat-Plate Boundary Layers with Suction," AIAA Journal 24, 1986, 208-214.

46. Masad, J. A. and Nayfeh, A. H., "Laminar Flow Control of Subsonic Boundary Layers by Suction and Heat-Transfer Strips," *Physics of Fluids A*4, 1992, 1259-1271.
47. Masad, J. A. and Nayfeh, A. H., "Effect of a Bulge on the Subharmonic Instability of Compressible Boundary Layers," *AIAA Paper No. 90-1526*, 1990.
48. Nayfeh, A. H. and Reed, H. L., "Stability of Flow over Axisymmetric Bodies with Porous Suction Strip," *Physics of Fluids* 28, 1985, 2990-2998.
49. Nayfeh, A. H., Reed, H. L., and Ragab, S. A., "Flow over Bodies with Suction Through Porous Strip," *AIAA Paper No. 80-1416*, 1980.
50. Reynolds, G. A. and Saric, W. S., "Experiments on the Stability of Flat-Plate Boundary Layers with Suction," *AIAA Journal* 24, 1986, 202-207.

Tables and Figures

Table 1. Variation of the most dangerous frequency with Mach number and hump location for all considered humps

	L1	L2	L3
Mach #	F	F	F
0.14	45×10^{-6}	40×10^{-6}	35×10^{-6}
0.50	45×10^{-6}	35×10^{-6}	30×10^{-6}
0.65	40×10^{-6}	35×10^{-6}	30×10^{-6}

Table 2. Transition location (i.e., $N = 9$) for different hump heights and different Mach numbers at location L1

Hump height	$M = 0.14$	$M = 0.50$	$M = 0.65$
	x	x	x
7.5×10^{-4}	0.320	--	--
8.0×10^{-4}	0.308	--	--
9.0×10^{-4}	0.300	0.313	--
1.0×10^{-3}	0.293	0.301	0.315

Table 3. Transition location (i.e., $N = 9$) for different hump heights and different Mach numbers at location L2

Hump height	$M = 0.14$	$M = 0.50$	$M = 0.65$
	x	x	x
7.5×10^{-4}	0.400	0.420	--
8.0×10^{-4}	0.394	0.410	--
9.0×10^{-4}	0.391	0.401	0.417
1.0×10^{-3}	0.388	0.395	0.405

Table 4. Transition location (i.e., $N = 9$) for different hump heights and different Mach numbers at location L3

Hump height	$M = 0.14$	$M = 0.50$	$M = 0.65$
	x	x	x
7.5×10^{-4}	0.492	0.510	--
8.0×10^{-4}	0.490	0.503	--
9.0×10^{-4}	0.487	0.496	0.516
1.0×10^{-3}	0.485	0.491	0.505

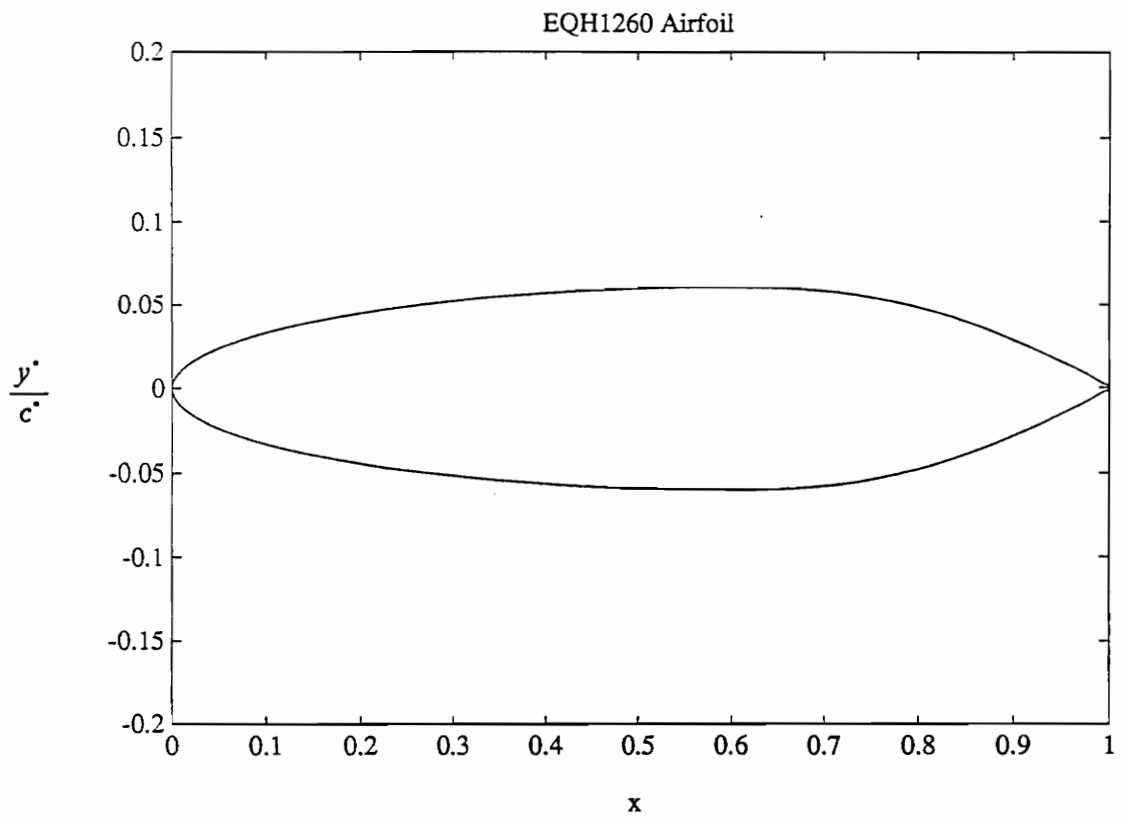


Figure 1. EQH1260 airfoil: chord = 70.4 in.

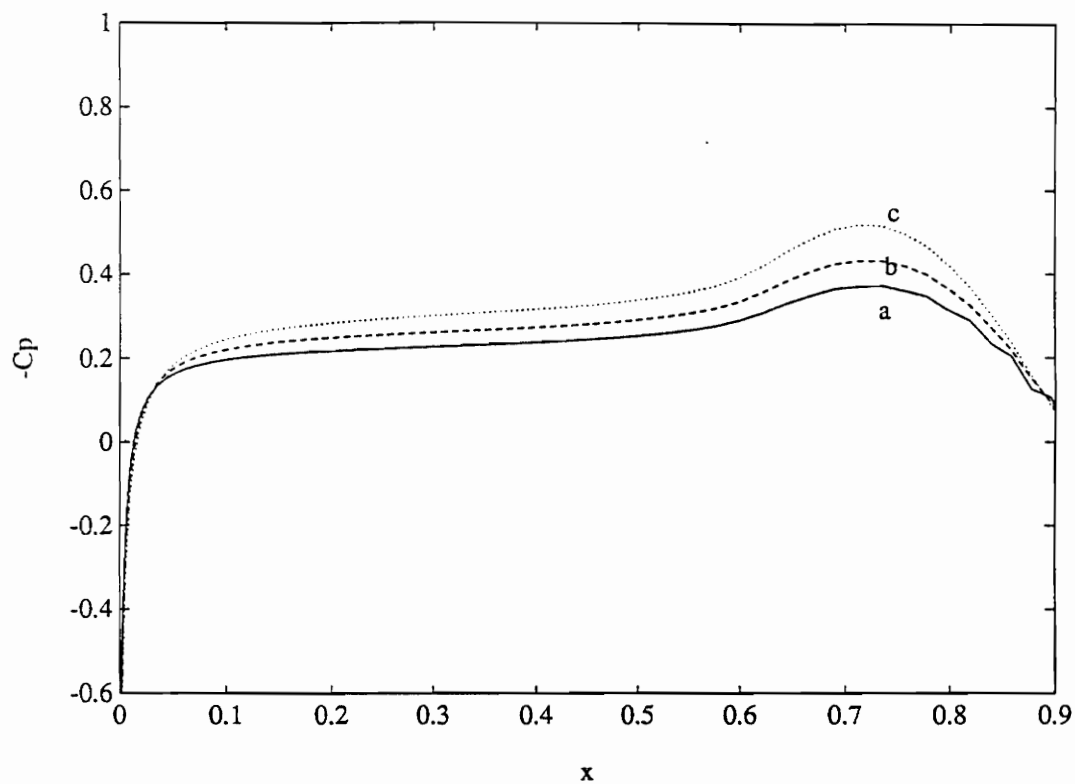


Figure 2. Pressure distributions for the EQH1260 airfoil calculated by using an Euler code: a) $M = 0.14$, b) $M = 0.50$, and c) $M = 0.65$.

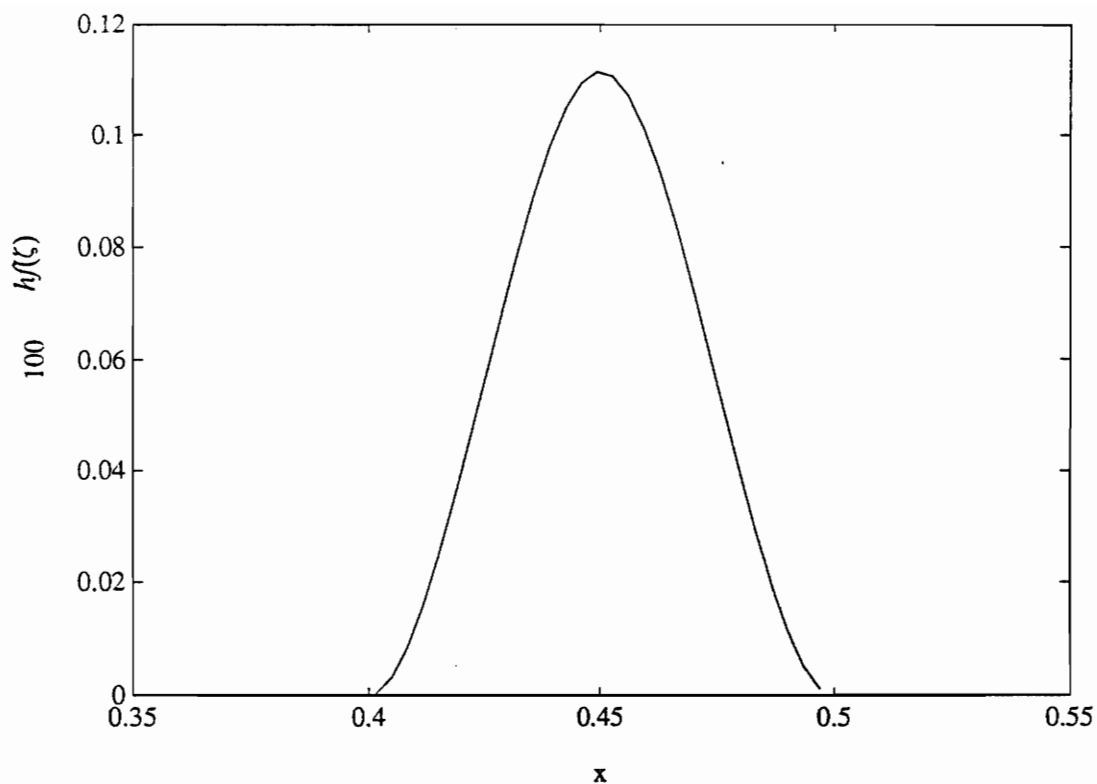


Figure 3. Shape of the considered cubic hump located at L3: $h_5 = 1.0 \times 10^{-3}$ and L3 ($x_l = 0.40$ and $x_r = 0.50$).

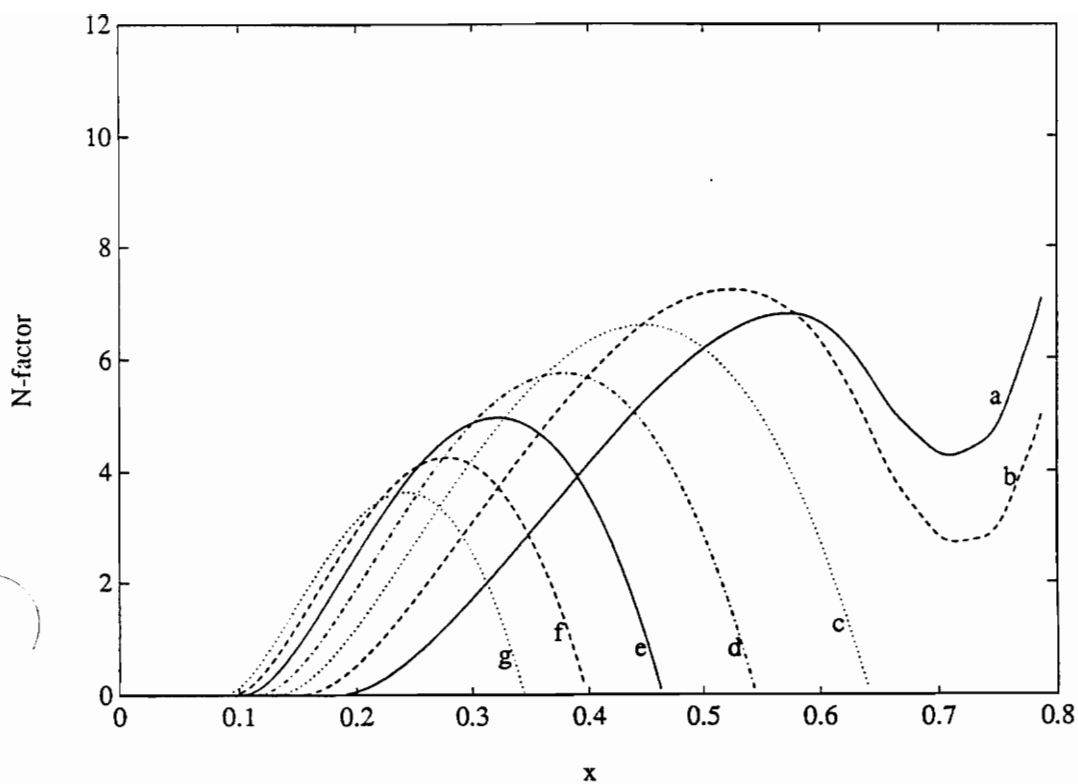


Figure 4. Variation of the N-factor with streamwise position for the clean airfoil when $M = 0.14$ for several frequencies: a) $F = 25 \times 10^{-6}$, b) $F = 30 \times 10^{-6}$, c) $F = 35 \times 10^{-6}$, d) $F = 40 \times 10^{-6}$, e) $F = 45 \times 10^{-6}$, f) $F = 50 \times 10^{-6}$, and g) $F = 55 \times 10^{-6}$.

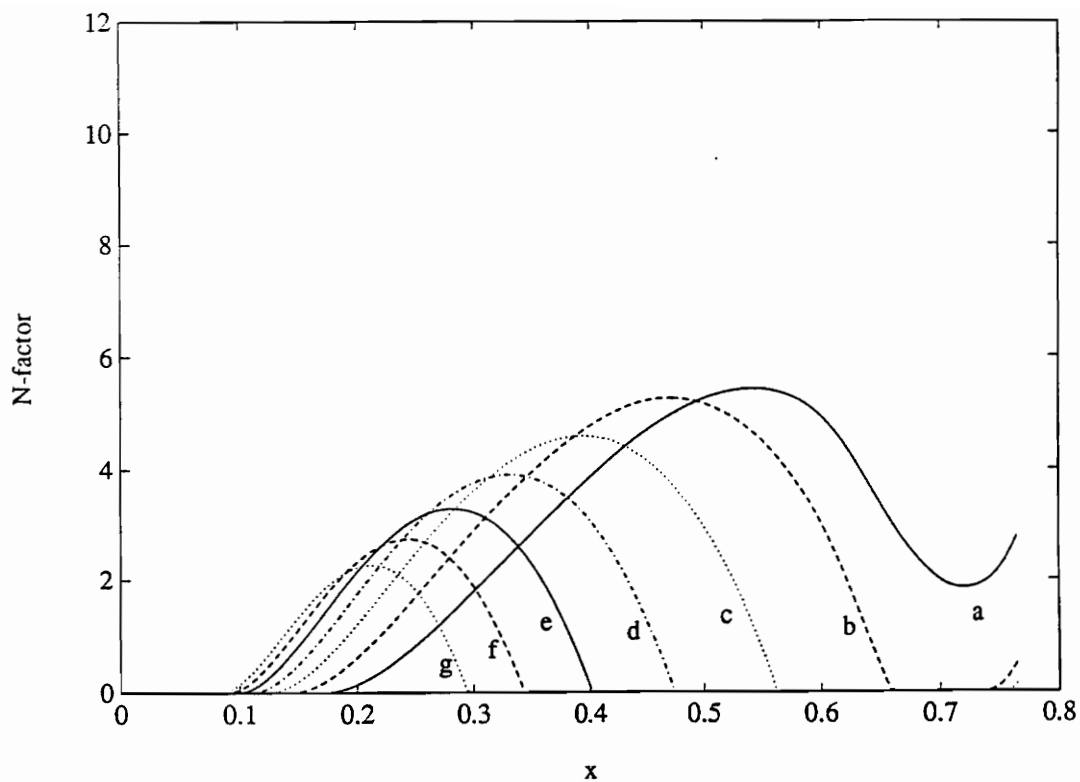


Figure 5. Variation of the N-factor with streamwise position for the clean airfoil when $M = 0.50$ for several frequencies: a) $F = 25 \times 10^{-6}$, b) $F = 30 \times 10^{-6}$, c) $F = 35 \times 10^{-6}$, d) $F = 40 \times 10^{-6}$, e) $F = 45 \times 10^{-6}$, f) $F = 50 \times 10^{-6}$, and g) $F = 55 \times 10^{-6}$.

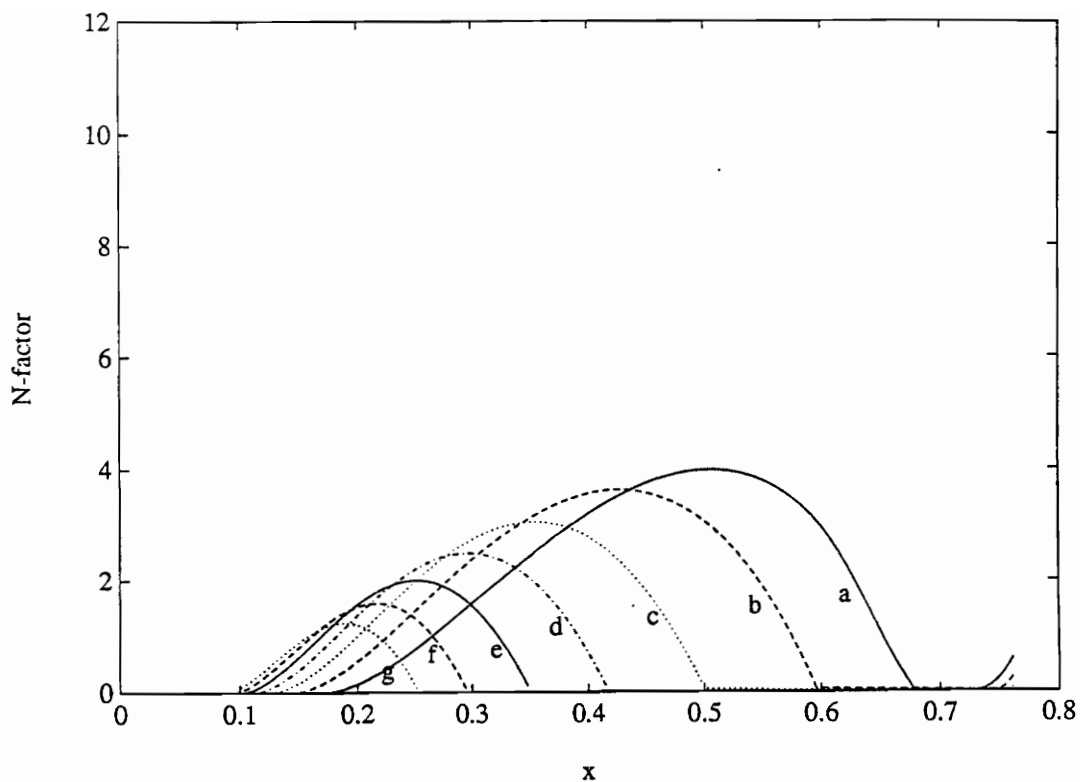


Figure 6. Variation of the N-factor with streamwise position for the clean airfoil when $M = 0.65$ for several frequencies: a) $F = 25 \times 10^{-6}$, b) $F = 30 \times 10^{-6}$, c) $F = 35 \times 10^{-6}$, d) $F = 40 \times 10^{-6}$, e) $F = 45 \times 10^{-6}$, f) $F = 50 \times 10^{-6}$, and g) $F = 55 \times 10^{-6}$.

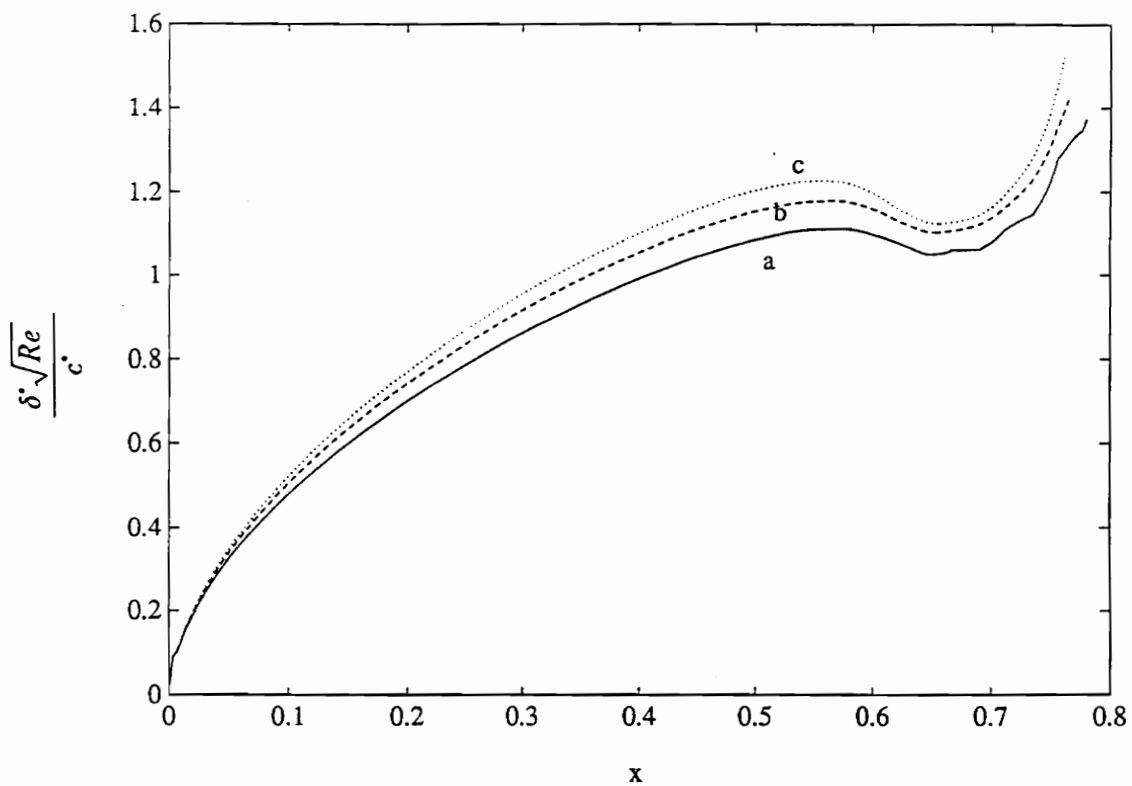


Figure 7. Variation of the displacement thickness with streamwise position for the clean airfoil at three Mach numbers: a) $M = 0.14$, b) $M = 0.50$, and c) $M = 0.65$.

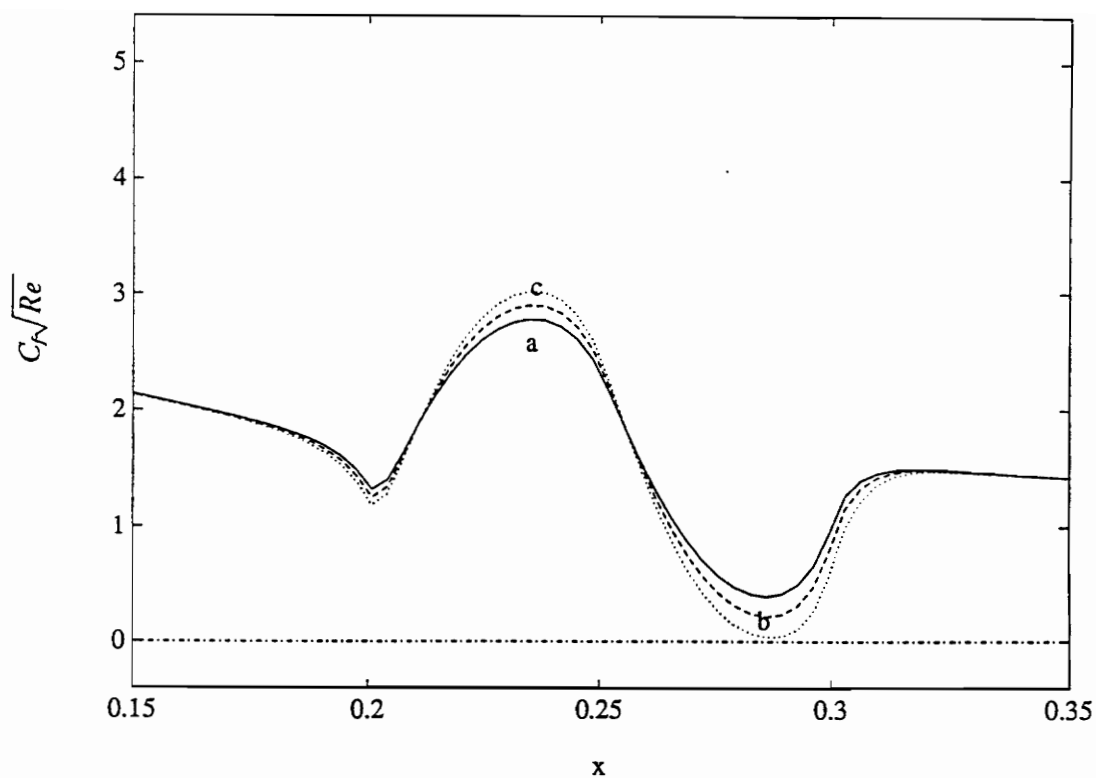


Figure 8. Variation of the skin-friction coefficient with streamwise position for humps # 3,4,5 located at L1 when $M = 0.14$: a) $h_3 = 8.0 \times 10^{-4}$, b) $h_4 = 9.0 \times 10^{-4}$, and c) $h_5 = 1.0 \times 10^{-3}$; L1 ($x_e = 0.20$ and $x_r = 0.30$).

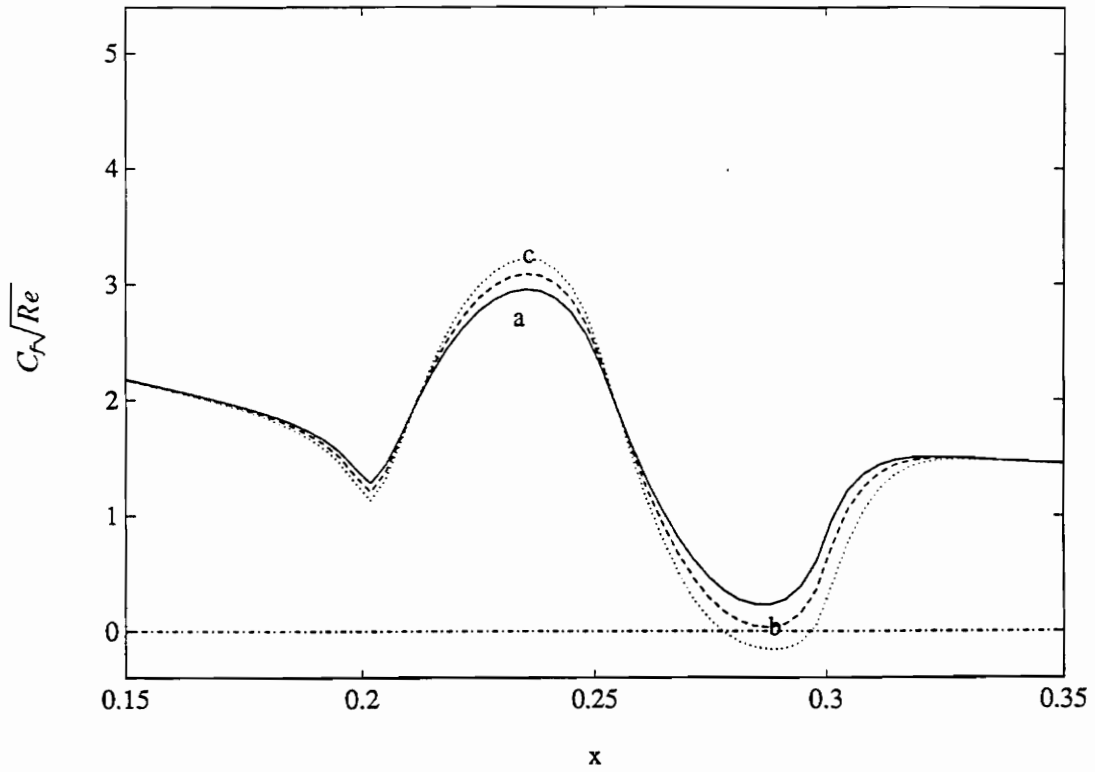


Figure 9. Variation of the skin-friction coefficient with streamwise position for humps # 3,4,5 located at L1 when $M = 0.50$: a) $h_3 = 8.0 \times 10^{-4}$, b) $h_4 = 9.0 \times 10^{-4}$, and c) $h_5 = 1.0 \times 10^{-3}$; L1 ($x_e = 0.20$ and $x_r = 0.30$).

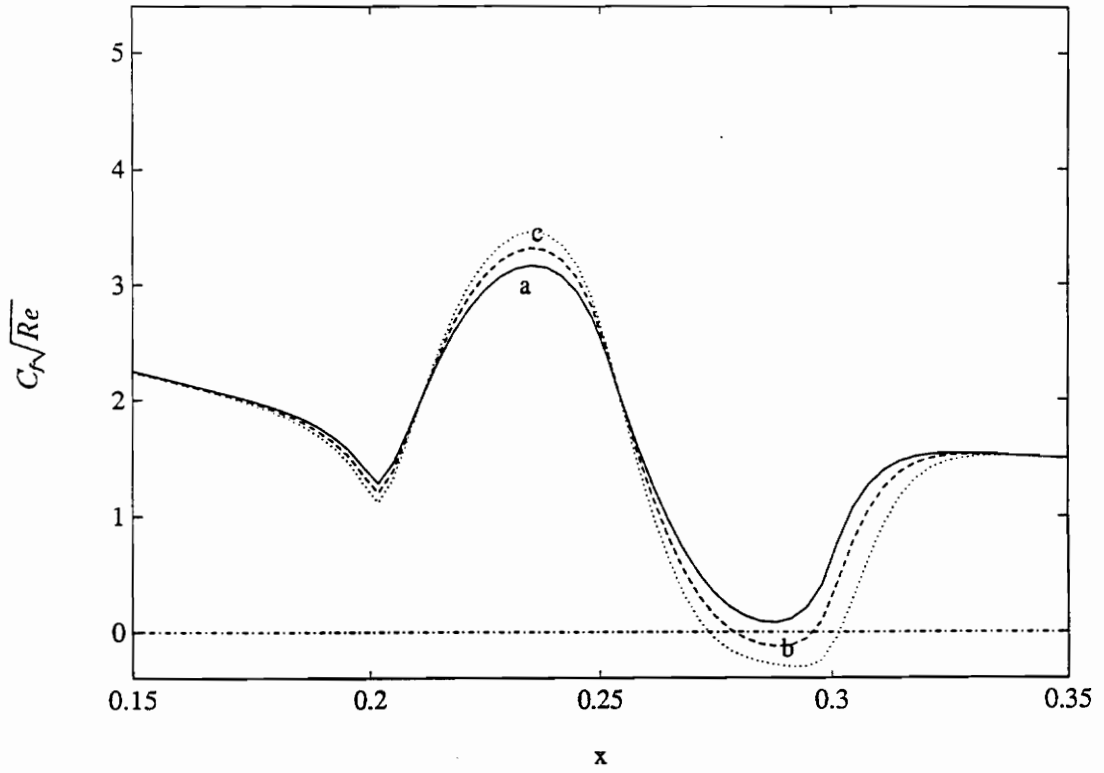


Figure 10. Variation of the skin-friction coefficient with streamwise position for humps # 3,4,5 located at L1 when $M = 0.65$: a) $h_3 = 8.0 \times 10^{-4}$, b) $h_4 = 9.0 \times 10^{-4}$, and c) $h_5 = 1.0 \times 10^{-3}$; L1 ($x_\ell = 0.20$ and $x_r = 0.30$).

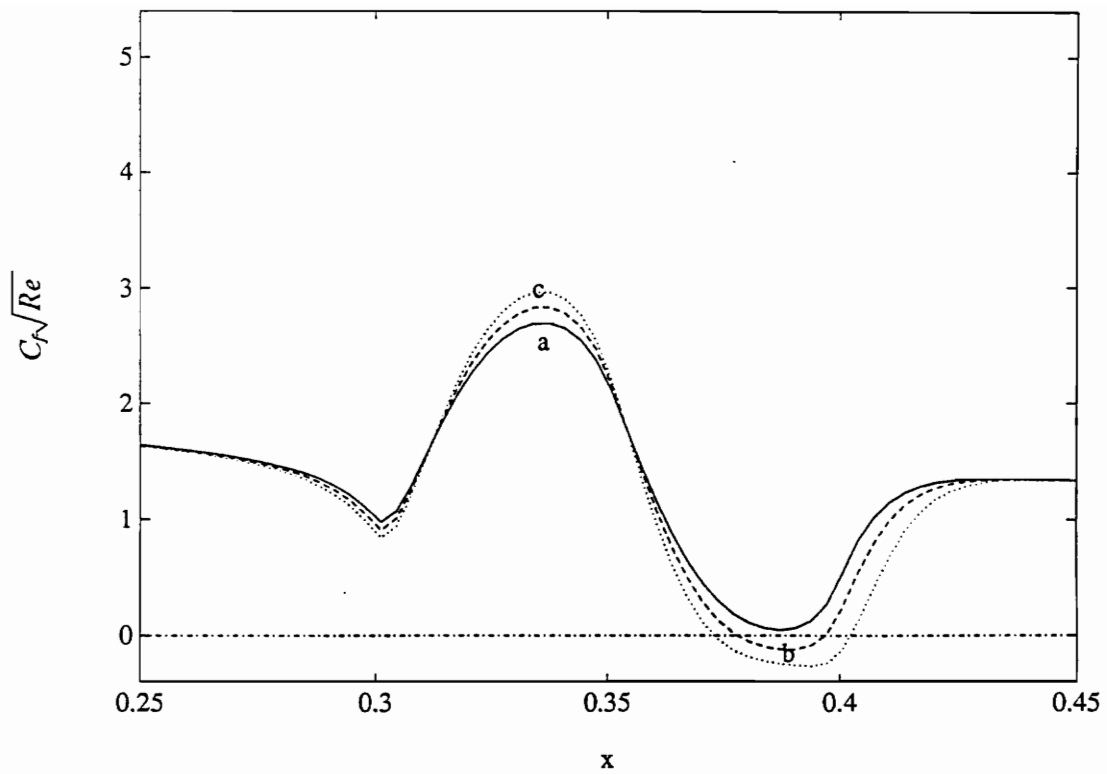


Figure 11. Variation of the skin-friction coefficient with streamwise position for humps # 3,4,5 located at L2 when $M = 0.50$: a) $h_3 = 8.0 \times 10^{-4}$, b) $h_4 = 9.0 \times 10^{-4}$, and c) $h_5 = 1.0 \times 10^{-3}$; L2 ($x_e = 0.3$ and $x_r = 0.4$).

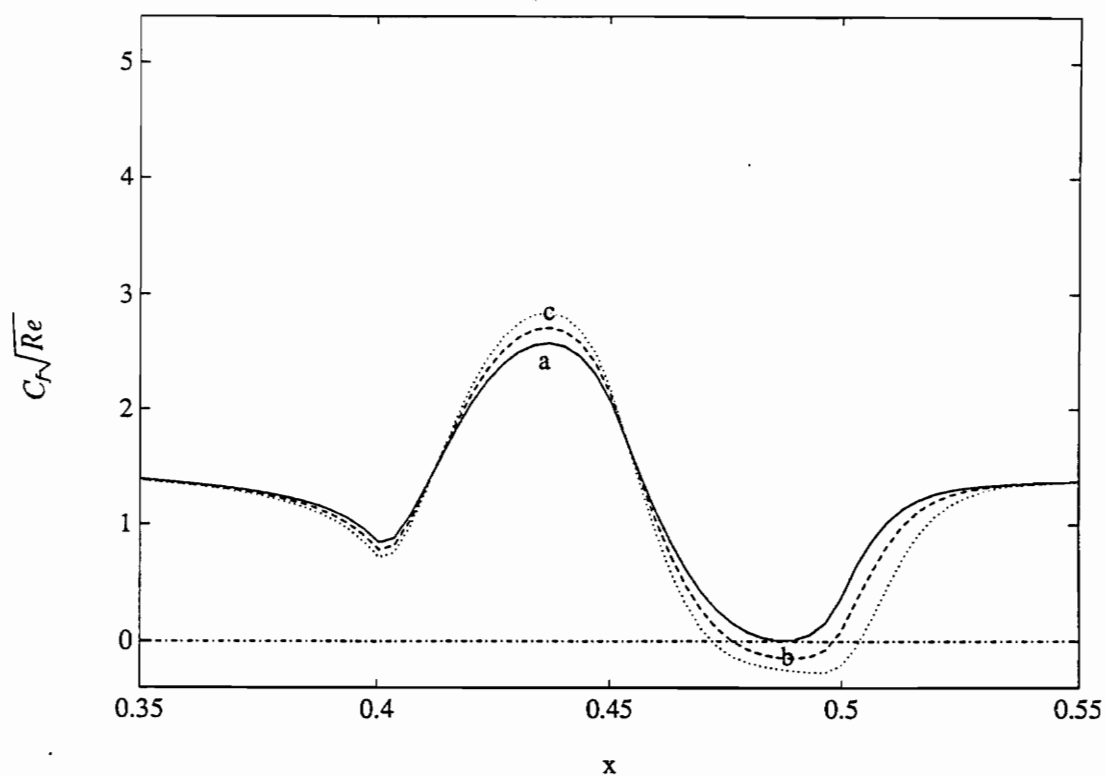


Figure 12. Variation of the skin-friction coefficient with streamwise position for humps # 3,4,5 located at L3 when $M = 0.50$: a) $h_3 = 8.0 \times 10^{-4}$, b) $h_4 = 9.0 \times 10^{-4}$, and c) $h_5 = 1.0 \times 10^{-3}$; L3 ($x_l = 0.40$ and $x_r = 0.50$).

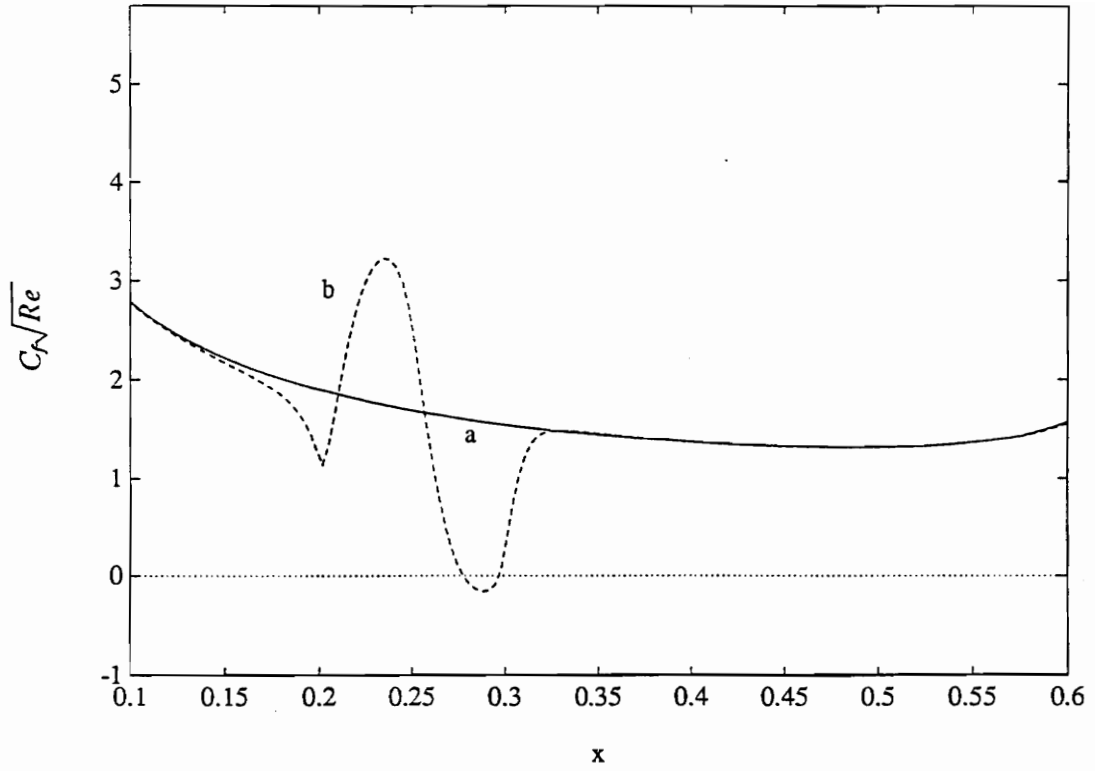


Figure 13. Variation of the skin-friction coefficient with streamwise position for the clean airfoil and hump # 5 located at L1: a) clean airfoil, b) $h_3 = 1.0 \times 10^{-3}$; $M = 0.50$ and L1 ($x_e = 0.20$ and $x_r = 0.30$).

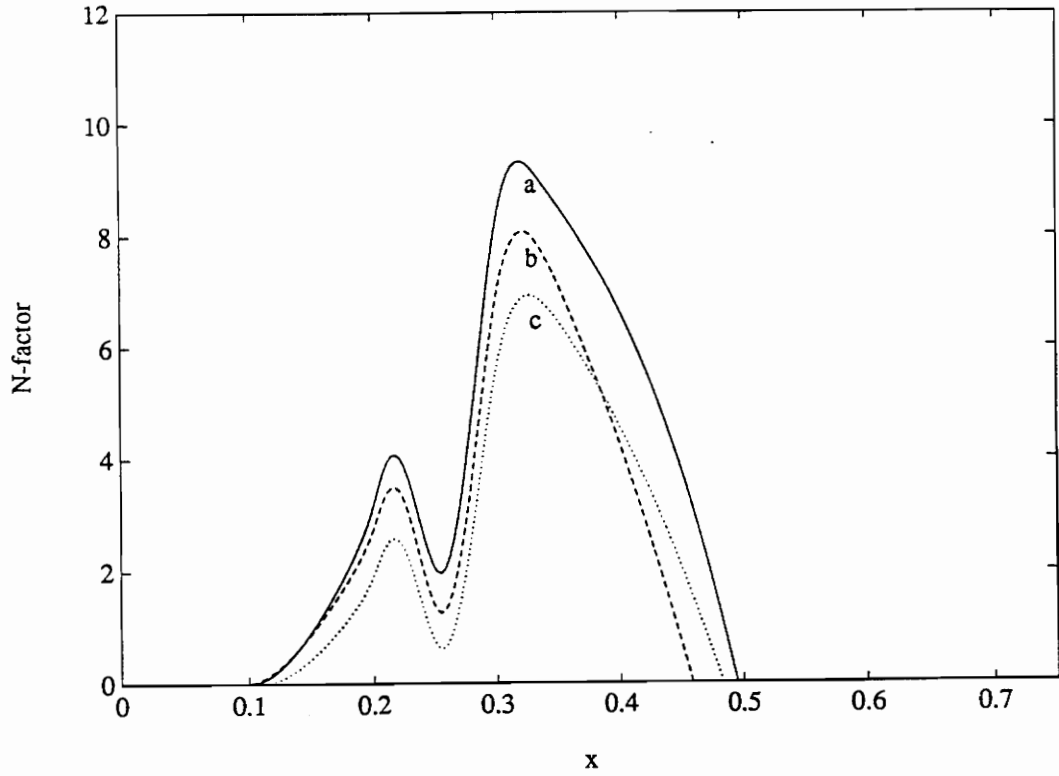


Figure 14. Variation of the N-factor for the most dangerous frequency with streamwise position for hump # 3 located at L1 and all three Mach numbers: a) $F = 45 \times 10^{-6}$ when $M = 0.14$, b) $F = 45 \times 10^{-6}$ when $M = 0.50$, and c) $F = 40 \times 10^{-6}$ when $M = 0.65$; $h_3 = 8.0 \times 10^{-4}$ and L1 ($x_\ell = 0.2$ and $x_r = 0.3$).

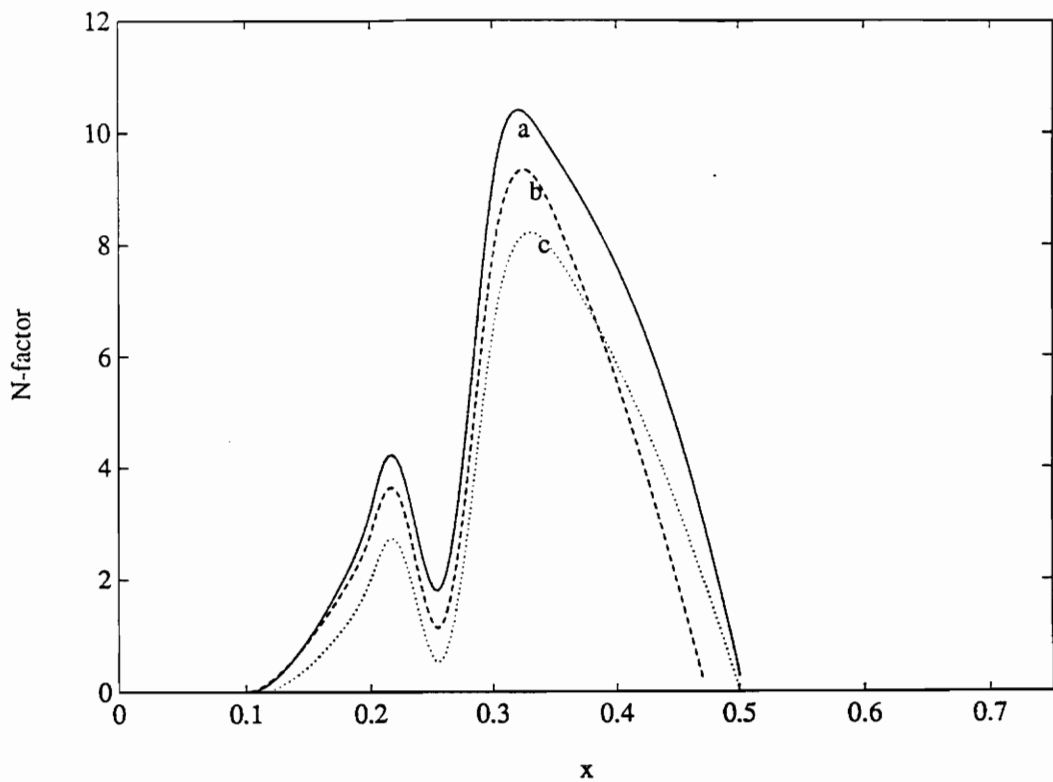


Figure 15. Variation of the N-factor for the most dangerous frequency with streamwise position for hump # 4 located at L1 and all three Mach numbers: a) $F = 45 \times 10^{-6}$ when $M = 0.14$, b) $F = 45 \times 10^{-6}$ when $M = 0.50$, and c) $F = 40 \times 10^{-6}$ when $M = 0.65$; $h_4 = 9.0 \times 10^{-4}$ and L1 ($x_l = 0.20$ and $x_r = 0.30$).

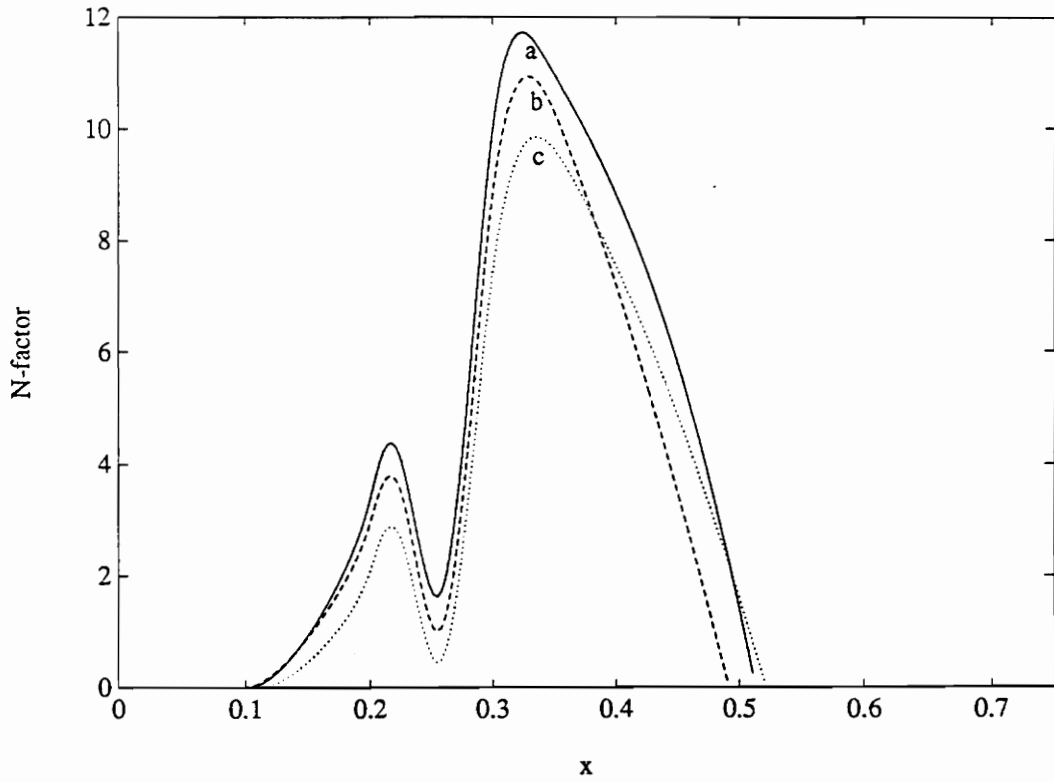


Figure 16. Variation of the N-factor for the most dangerous frequency with streamwise position for hump # 5 located at L1 and all three Mach numbers: a) $F = 45 \times 10^{-6}$ when $M = 0.14$, b) $F = 45 \times 10^{-6}$ when $M = 0.50$, and c) $F = 40 \times 10^{-6}$ when $M = 0.65$; $h_5 = 1.0 \times 10^{-3}$ and L1 ($x_l = 0.20$ and $x_r = 0.30$).

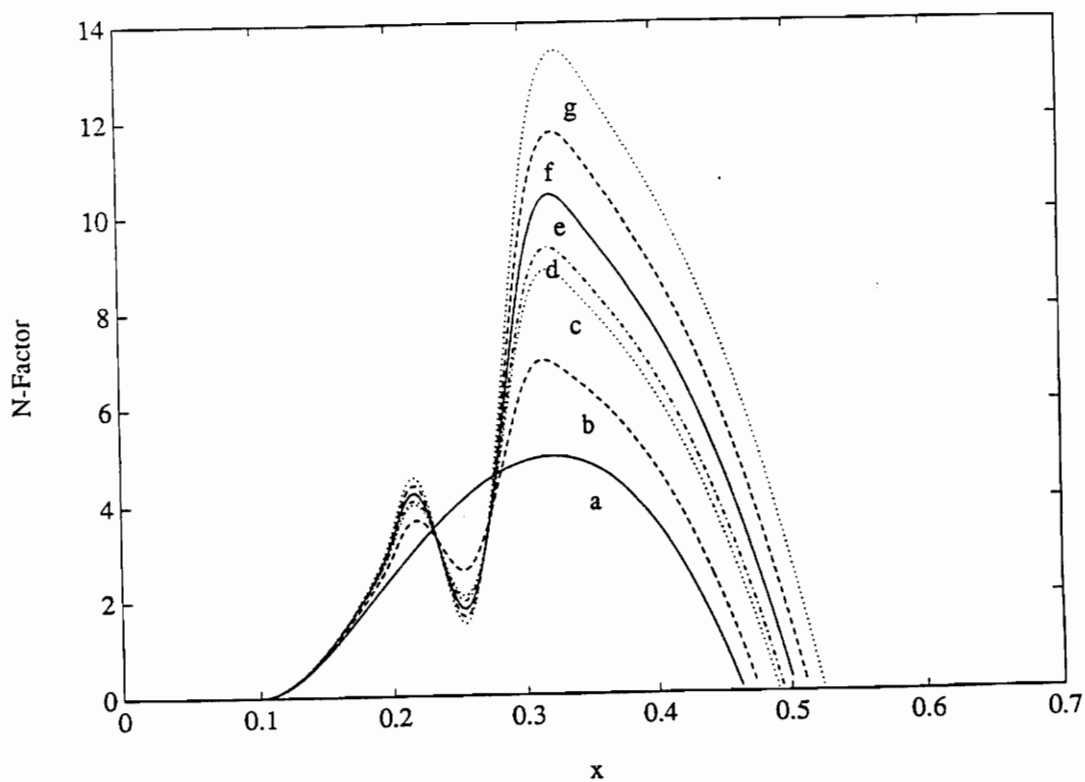


Figure 17. Variation of the N-factor for the most dangerous frequency with streamwise position when $M=0.14$ for seven heights at location L1: a) h_0 clean airfoil, b) $h_1 = 5.0 \times 10^{-4}$, c) $h_2 = 7.5 \times 10^{-4}$, d) $h_3 = 8.0 \times 10^{-4}$, e) $h_4 = 9.0 \times 10^{-4}$, f) $h_5 = 1.0 \times 10^{-3}$, and g) $h_6 = 1.2 \times 10^{-3}$; $F = 45 \times 10^{-6}$ and L1 ($x_e = 0.20$ and $x_r = 0.30$).

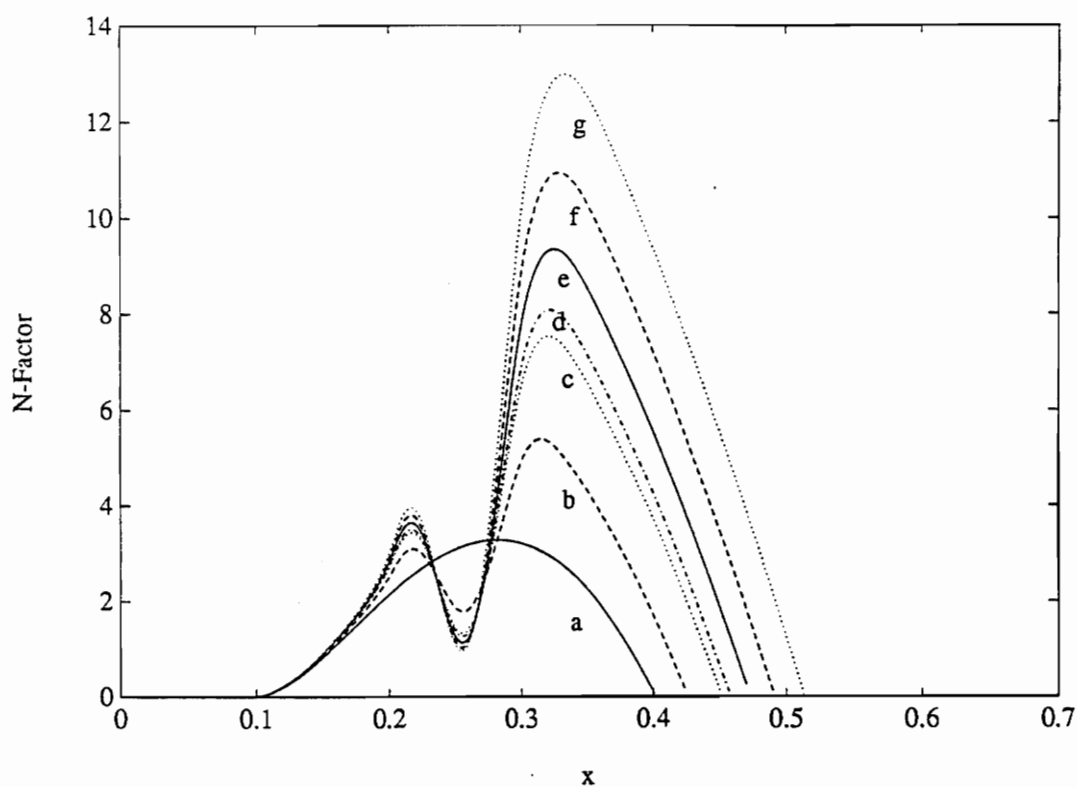


Figure 18. Variation of the N-factor for the most dangerous frequency with streamwise position when $M=0.50$ for seven heights at location L1: a) h_0 clean airfoil, b) $h_1 = 5.0 \times 10^{-4}$, c) $h_2 = 7.5 \times 10^{-4}$, d) $h_3 = 8.0 \times 10^{-4}$, e) $h_4 = 9.0 \times 10^{-4}$, f) $h_5 = 1.0 \times 10^{-3}$, g) $h_6 = 1.2 \times 10^{-3}$; and $F = 45 \times 10^{-6}$ and L1 ($x_\ell = 0.20$ and $x_r = 0.30$).

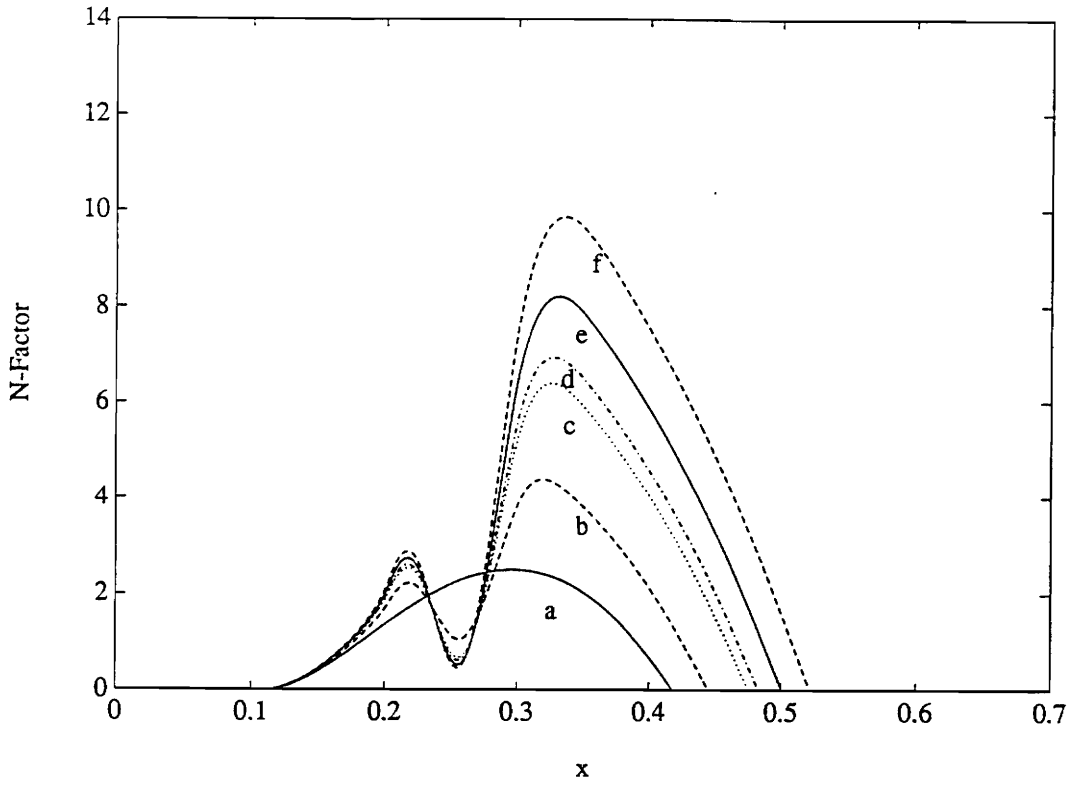


Figure 19. Variation of the N-factor for the most dangerous frequency with streamwise position when $M=0.65$ for six heights at location L1: a) h_0 clean airfoil, b) $h_1 = 5.0 \times 10^{-4}$, c) $h_2 = 7.5 \times 10^{-4}$, d) $h_3 = 8.0 \times 10^{-4}$, e) $h_4 = 9.0 \times 10^{-4}$, and f) $h_5 = 1.0 \times 10^{-3}$; $F = 40 \times 10^{-6}$ and L1 ($x_\ell = 0.20$ and $x_r = 0.30$).

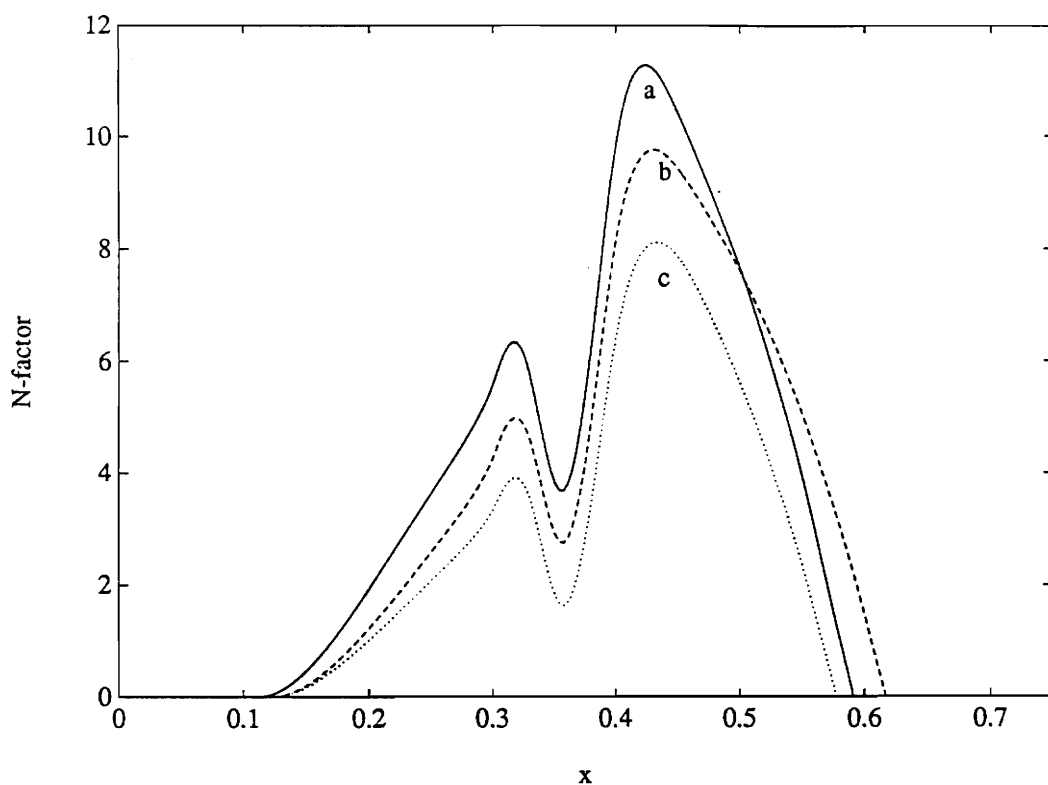


Figure 20. Variation of the N-factor for the most dangerous frequency with streamwise position for hump # 3 located at L2 and all three Mach numbers: a) $F = 40 \times 10^{-6}$ when $M = 0.14$, b) $F = 40 \times 10^{-6}$ when $M = 0.50$, and c) $F = 35 \times 10^{-6}$ when $M = 0.65$; $h_3 = 8.0 \times 10^{-4}$ and L2 ($x_\ell = 0.30$ and $x_r = 0.40$).

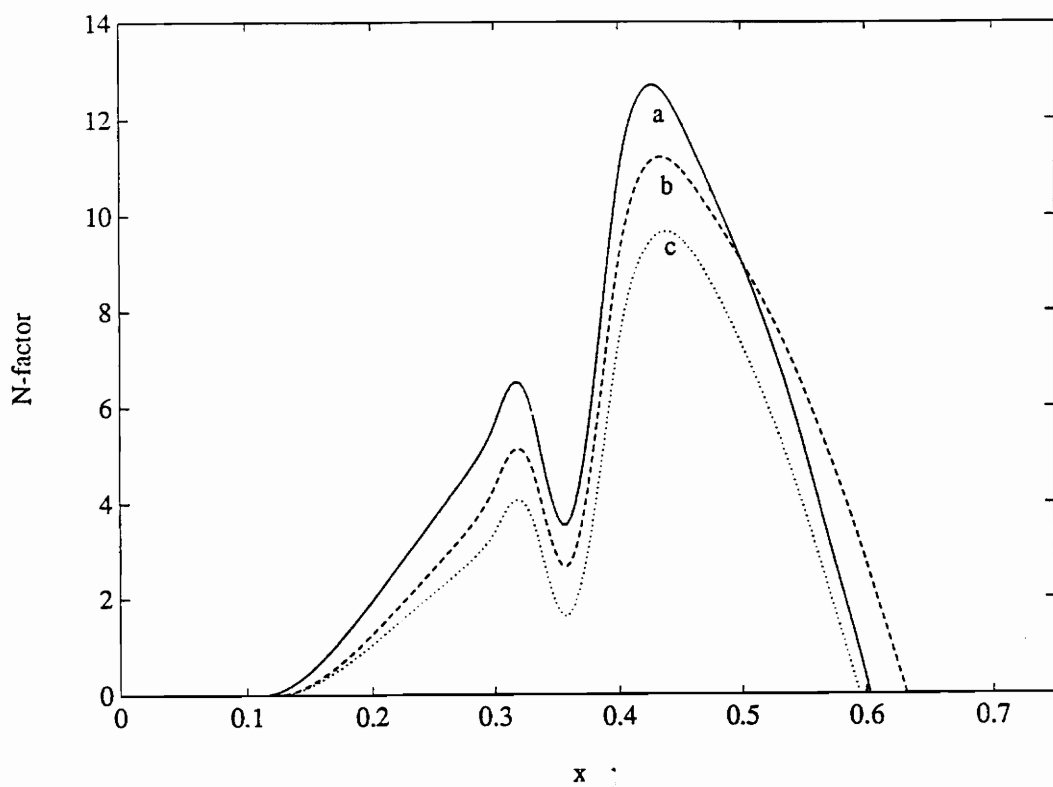


Figure 21. Variation of the N-factor for the most dangerous frequency with streamwise position for hump # 4 located at L2 and all three Mach numbers: a) $F = 40 \times 10^{-6}$ when $M = 0.14$, b) $F = 40 \times 10^{-6}$ when $M = 0.50$, and c) $F = 35 \times 10^{-6}$ when $M = 0.65$; $h_4 = 9.0 \times 10^{-4}$ and L2 ($x_l = 0.30$ and $x_r = 0.40$).

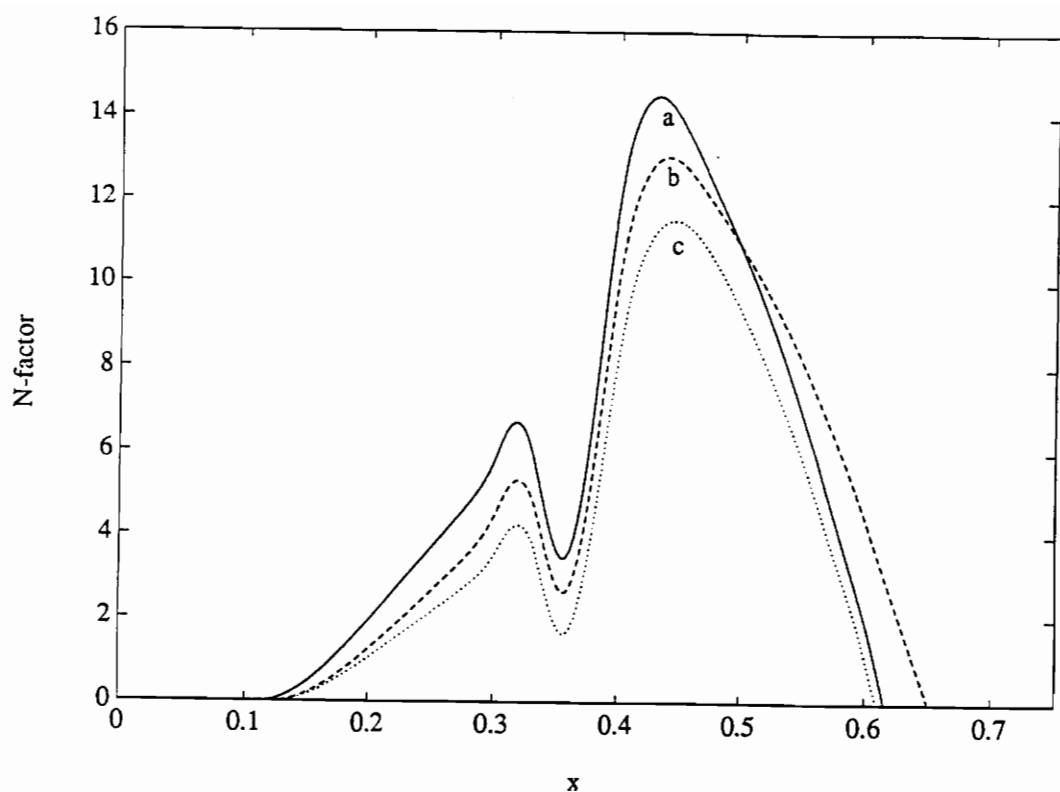


Figure 22. Variation of the N-factor for the most dangerous frequency with streamwise position for hump # 5 located at L2 and all three Mach numbers: a) $F = 40 \times 10^{-6}$ when $M = 0.14$, b) $F = 40 \times 10^{-6}$ when $M = 0.50$, and c) $F = 35 \times 10^{-6}$ when $M = 0.65$; $h_5 = 1.0 \times 10^{-3}$ and L2 ($x_l = 0.30$ and $x_r = 0.4$).

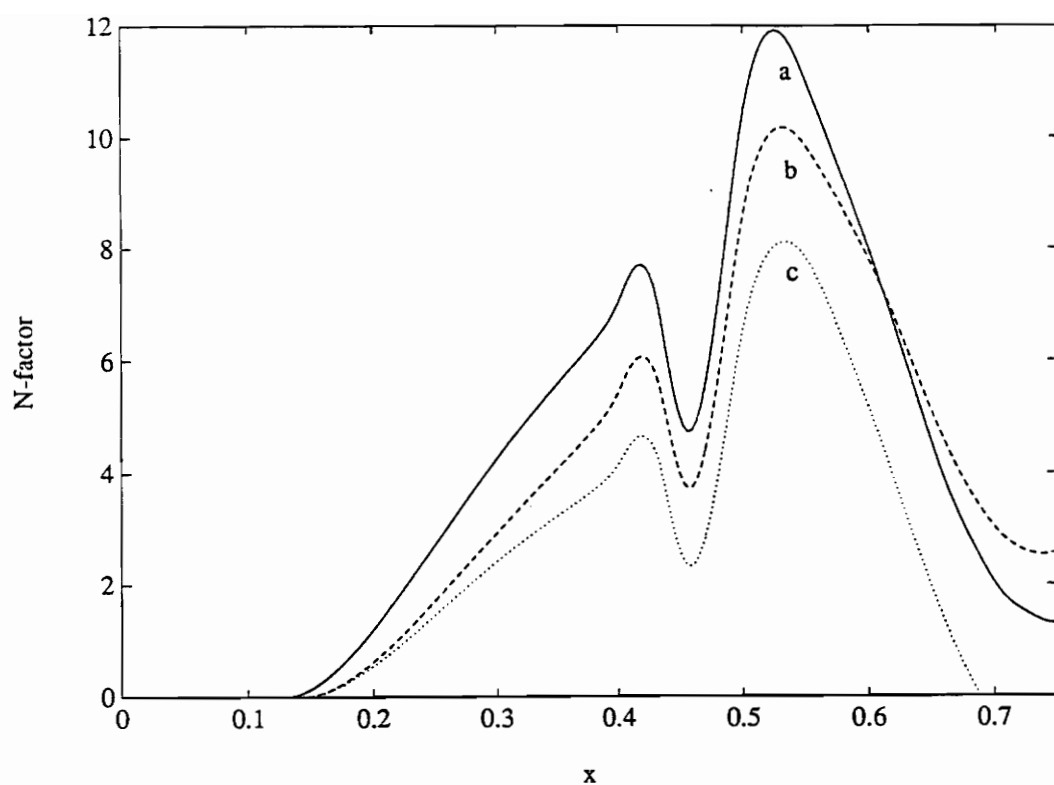


Figure 23. Variation of the N-factor for the most dangerous frequency with streamwise position for hump # 3 located at L3 and all three Mach numbers: a) $F = 35 \times 10^{-6}$ when $M = 0.14$, b) $F = 30 \times 10^{-6}$ when $M = 0.50$, and c) $F = 30 \times 10^{-6}$ when $M = 0.65$; $h_3 = 8.0 \times 10^{-4}$ and L3 ($x_l = 0.40$ and $x_r = 0.50$).

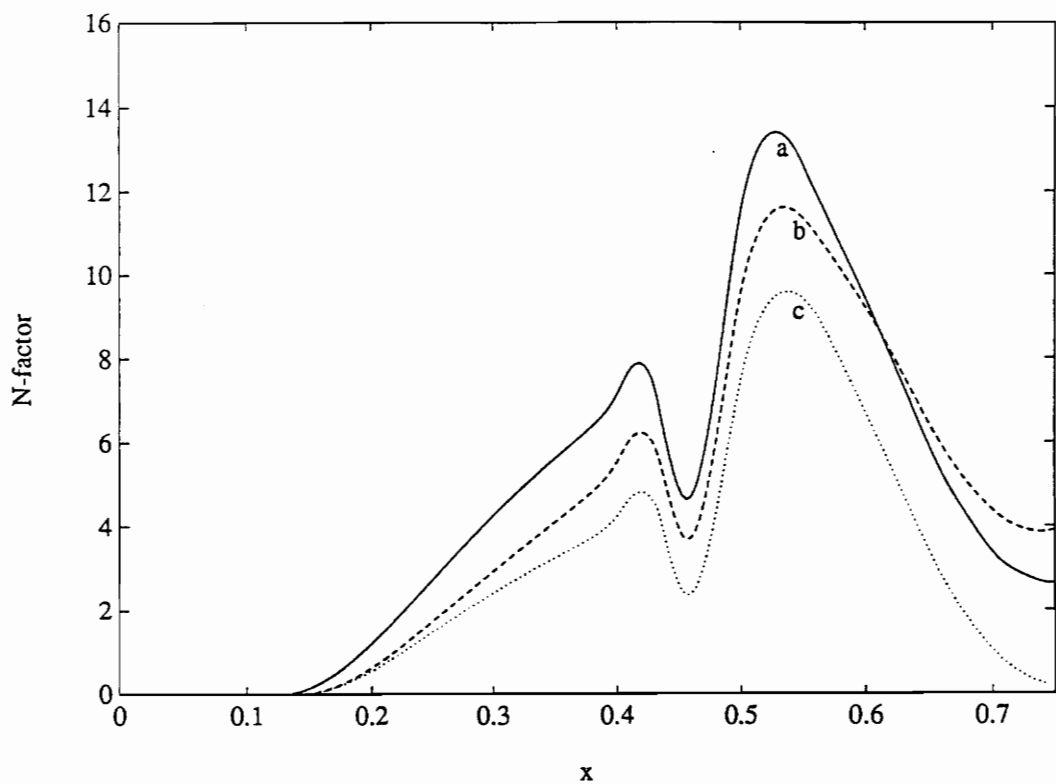


Figure 24. Variation of the N-factor for the most dangerous frequency with streamwise position for hump # 4 located at L3 and all three Mach numbers: a) $F = 35 \times 10^{-6}$ when $M = 0.14$, b) $F = 30 \times 10^{-6}$ when $M = 0.50$, and c) $F = 30 \times 10^{-6}$ when $M = 0.65$; $h_4 = 9.0 \times 10^{-4}$ and L3 ($x_l = 0.30$ and $x_r = 0.40$).

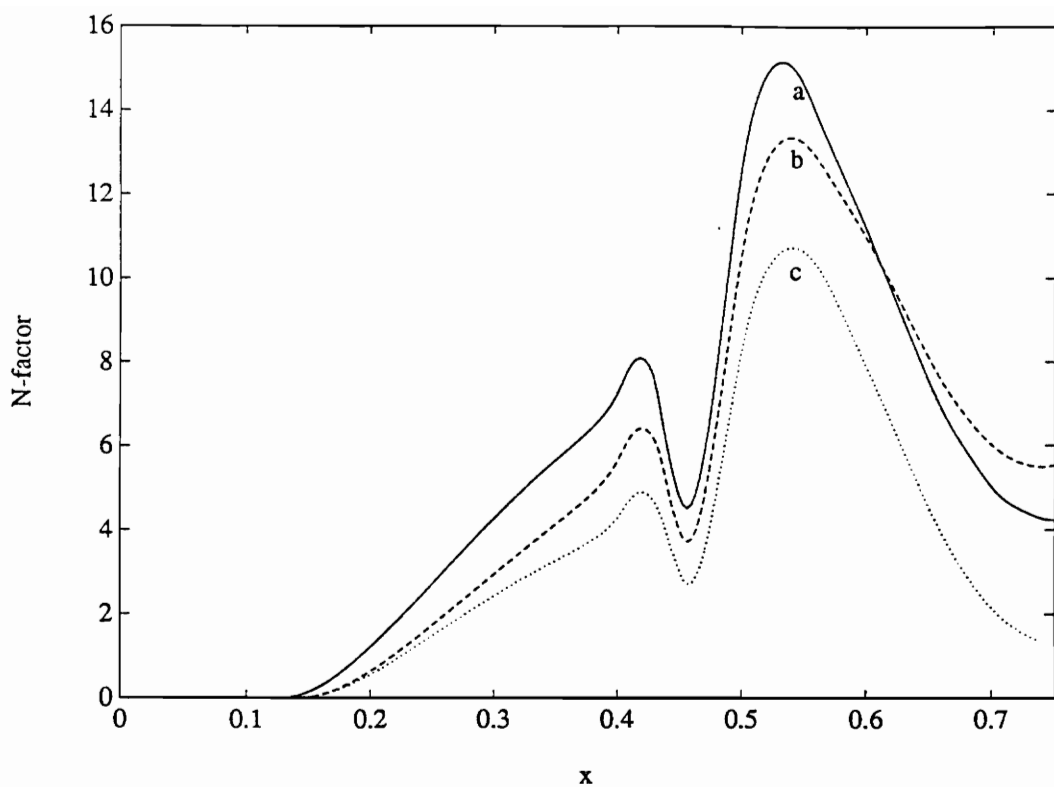


Figure 25. Variation of the N-factor for the most dangerous frequency with streamwise position for hump # 5 located at L3 and all three Mach numbers: a) $F = 35 \times 10^{-6}$ when $M = 0.14$, b) $F = 30 \times 10^{-6}$ when $M = 0.50$, and c) $F = 30 \times 10^{-6}$ when $M = 0.65$; $h_5 = 1.0 \times 10^{-3}$ and L3 ($x_l = 0.30$ and $x_r = 0.40$).

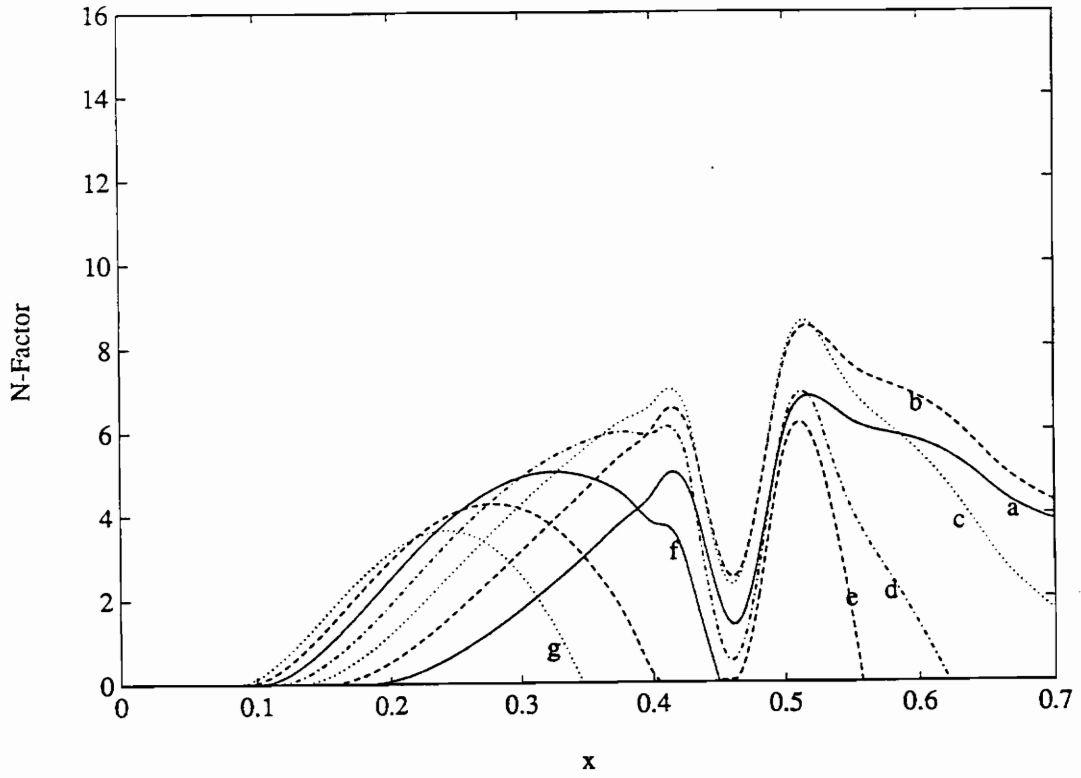


Figure 26. Variation of the N-factor with streamwise position for several frequencies with suction for hump # 5 located at L3 when $M = 0.14$: a) $F = 25 \times 10^{-6}$, b) $F = 30 \times 10^{-6}$, c) $F = 35 \times 10^{-6}$, d) $F = 40 \times 10^{-6}$, e) $F = 45 \times 10^{-6}$, f) $F = 50 \times 10^{-6}$, and g) $F = 55 \times 10^{-6}$; $\Delta x_{suction} = 0.37$ to 0.54 , $C_q = 1.5 \times 10^{-4}$, $h_5 = 1.0 \times 10^{-3}$, and L3 ($x_\ell = 0.40$ to $x_r = 0.50$).

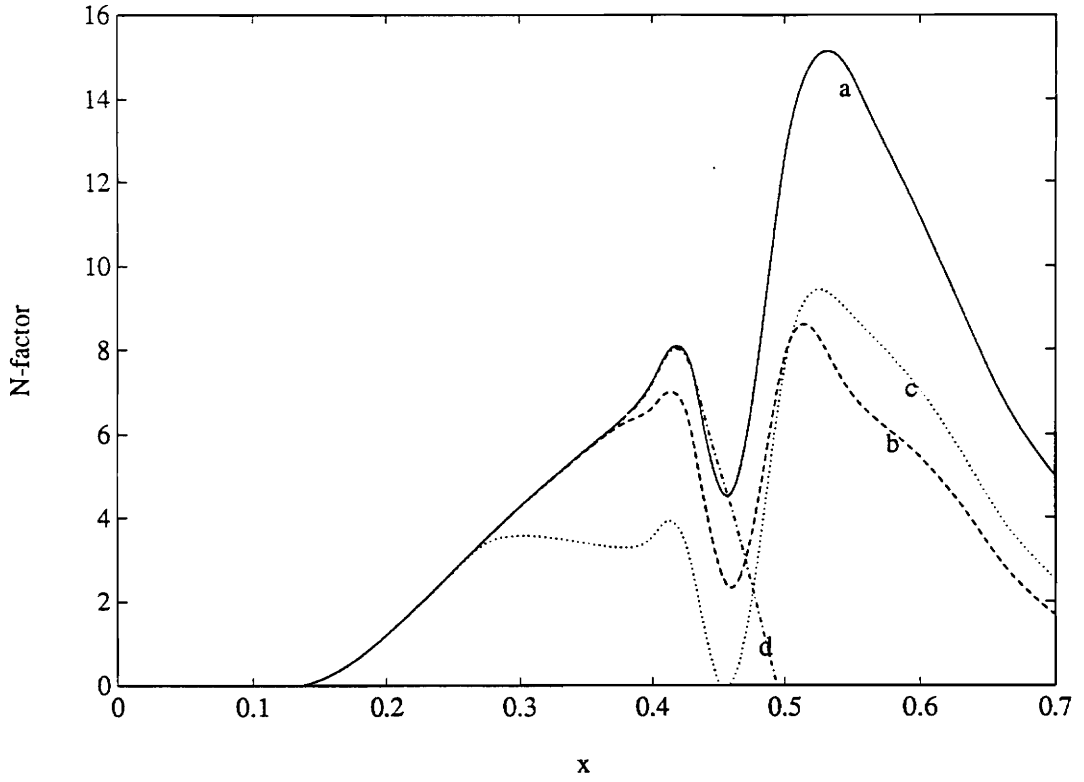


Figure 27. Variation of the N-factor for the most dangerous frequency with streamwise position for three suction location when $M = 0.14$ a) no suction, b) $S_1 : x = 0.34$ to 0.54 , c) $S_2 : x = 0.27$ to 0.44 , and d) $S_3 : x = 0.42$ to 0.59 ; $F = 35 \times 10^{-6}$, $C_q = 1.5 \times 10^{-4}$, $h_5 = 1.0 \times 10^{-3}$, and L3 ($x_\ell = 0.40$ and $x_r = 0.50$).

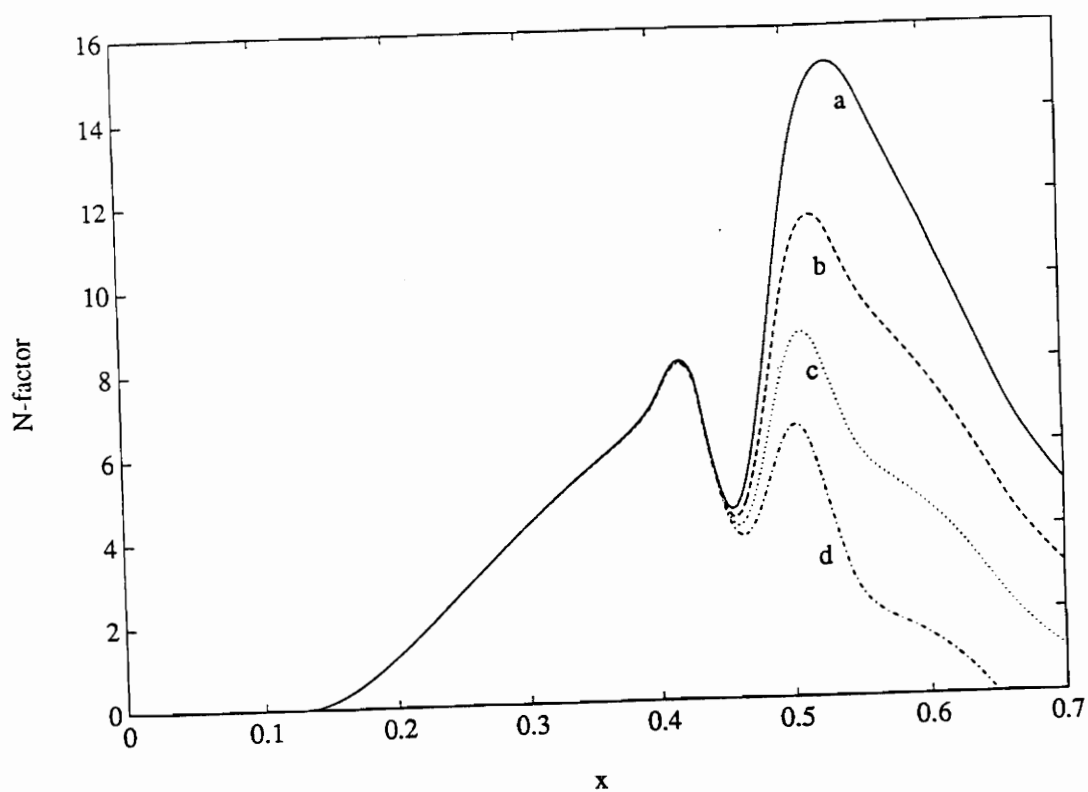


Figure 28. Influence of a suction strip on the variation of the N-factor for the most dangerous frequency with streamwise position for three suction levels when $M = 0.14$ a) no suction, b) $C_q = 1.5 \times 10^{-4}$, c) $C_q = 3.0 \times 10^{-4}$, and d) $C_q = 4.5 \times 10^{-4}$; $F = 35 \times 10^{-6}$, suction strip extends from $x = 0.45$ to 0.53 , $h_s = 1.0 \times 10^{-3}$, and $L3$ ($x_l = 0.40$ and $x_r = 0.50$).

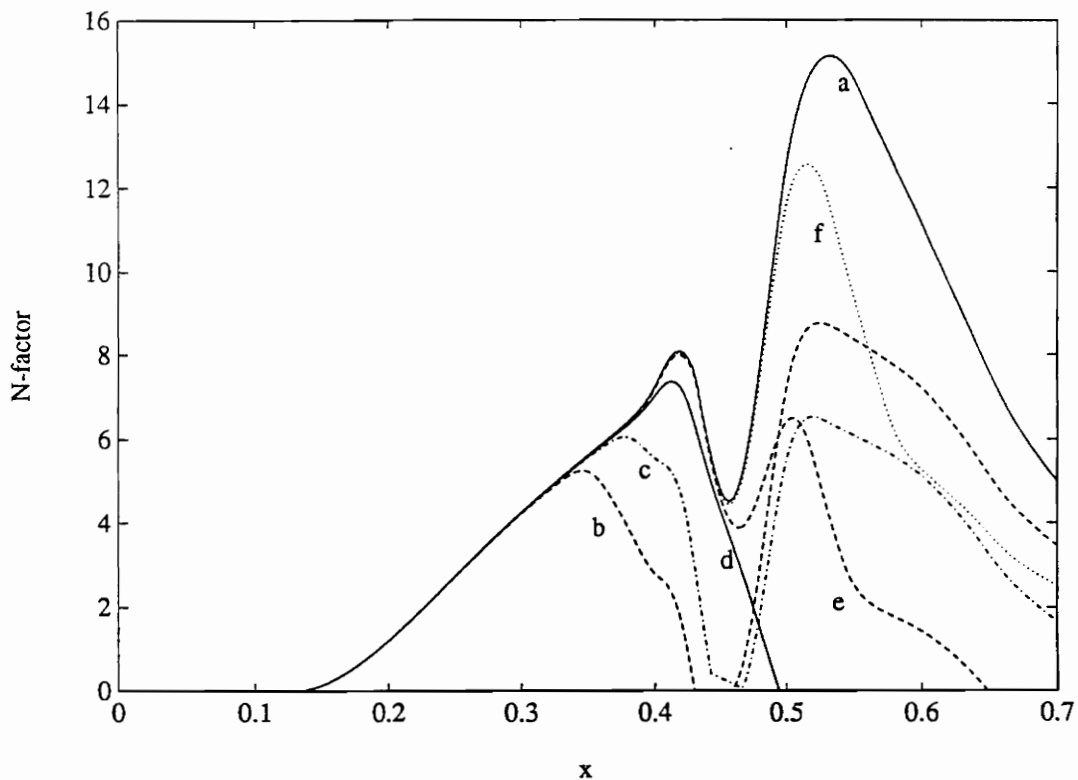


Figure 29. Variation of the N-factor for the most dangerous frequency with streamwise position for different locations of a suction strip of width 0.08: a) no suction, b) $S_1: x = 0.34$ to 0.42 , c) $S_2: x = 0.37$ to 0.45 , d) $S_3: x = 0.40$ to 0.48 , e) $S_4: x = 0.45$ to 0.53 , and f) $S_5: x = 0.49$ to 0.57 ; $F = 35 \times 10^{-6}$, $C_q = 4.5 \times 10^{-4}$, $M = 0.14$, and L3 ($x_\ell = 0.40$ and $x_r = 0.50$)..

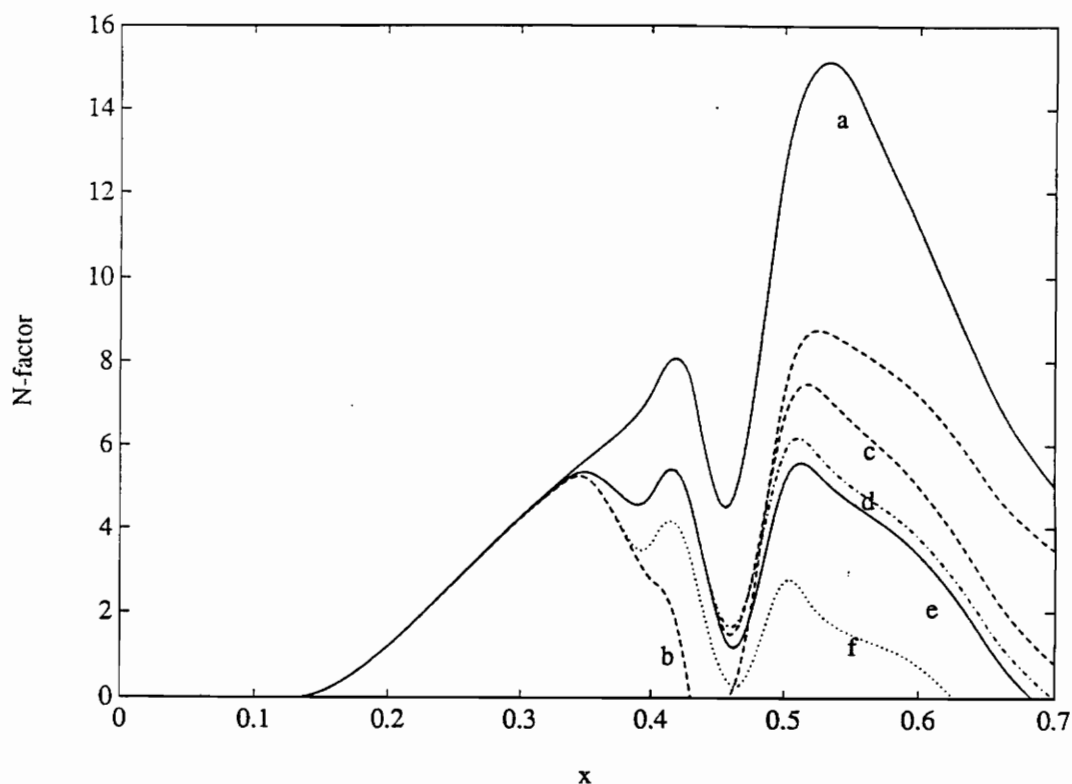


Figure 30. Variation of the N-factor for the most dangerous frequency with streamwise position for two-suction-strip configurations and different suction levels: a) no suction, b) S_1 : $x = 0.34$ to 0.42 with $C_q = 4.5 \times 10^{-4}$, c) S_2 : $x = 0.34$ to 0.38 with $C_q = 3.0 \times 10^{-4}$ and $x = 0.44$ to 0.48 with $C_q = 2.0 \times 10^{-4}$, d) S_3 : $x = 0.34$ to 0.38 with $C_q = 3.0 \times 10^{-4}$ and $x = 0.45$ to 0.49 with $C_q = 3.0 \times 10^{-4}$, e) S_4 : $x = 0.34$ to 0.38 with $C_q = 3.0 \times 10^{-4}$ and $x = 0.44$ to 0.48 with $C_q = 3.0 \times 10^{-4}$, and f) S_5 : $x = 0.34$ to 0.38 with $C_q = 4.5 \times 10^{-4}$ and $x = 0.45$ to 0.49 with $C_q = 4.5 \times 10^{-4}$; $F = 35 \times 10^{-6}$, $M = 0.14$, and $L3$ ($x_c = 0.40$ and $x_r = 0.50$).

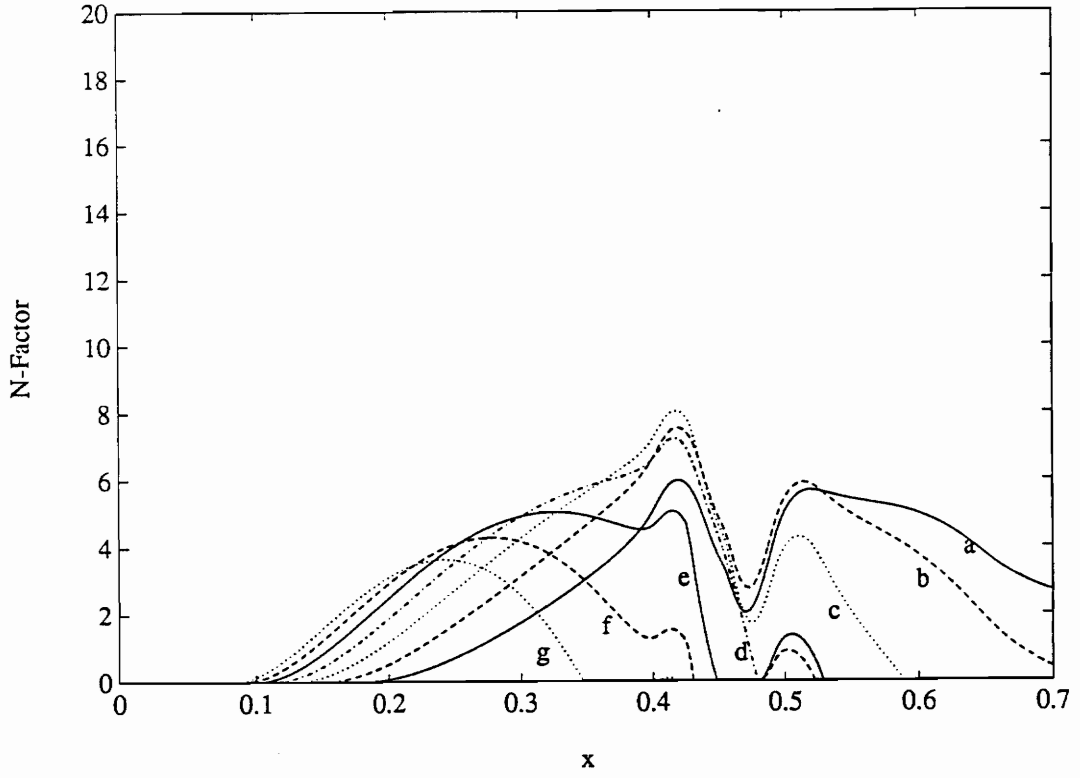


Figure 31. Variation of the N-factor with streamwise position for several frequencies with cooling for hump # 5 located at L3 when $M = 0.14$: a) $F = 25 \times 10^{-6}$, b) $F = 30 \times 10^{-6}$, c) $F = 35 \times 10^{-6}$, d) $F = 40 \times 10^{-6}$, e) $F = 45 \times 10^{-6}$, f) $F = 50 \times 10^{-6}$, and g) $F = 55 \times 10^{-6}$; $\Delta x_{cooling} = 0.45$ to 0.49 , $T_w/T_{ad} = 0.60$, $h_5 = 1.0 \times 10^{-3}$, and L3 ($x_e = 0.40$ and $x_r = 0.50$).

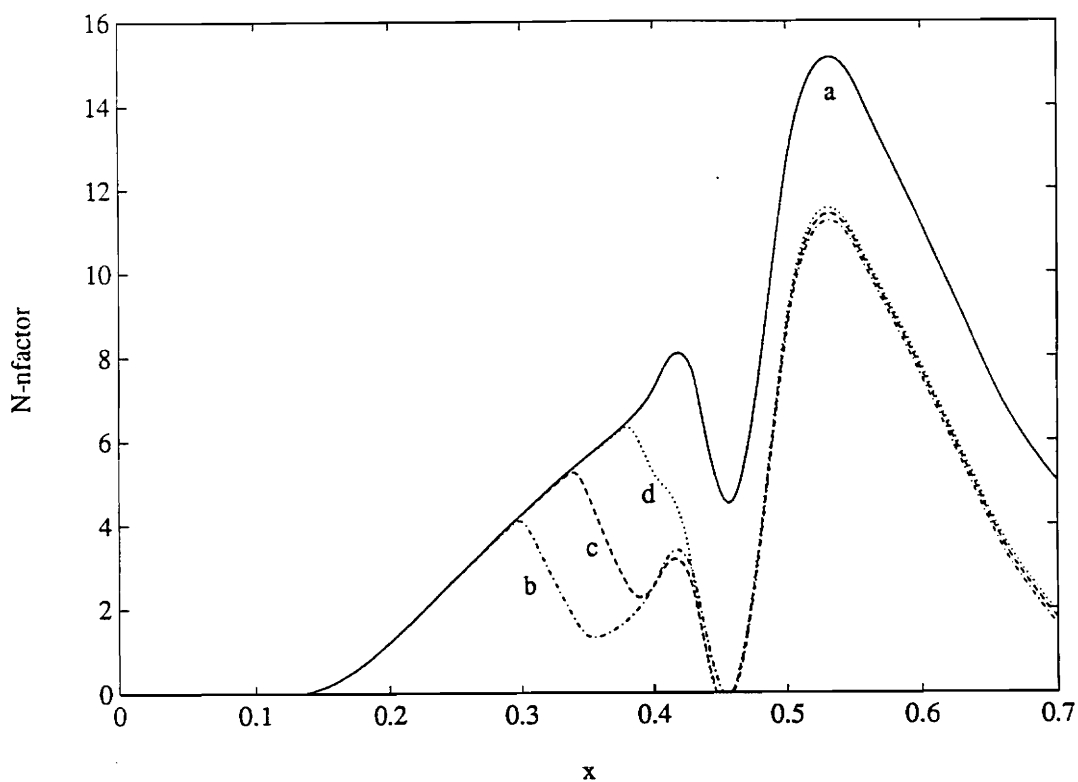


Figure 32. Variation of the N-factor for the most dangerous frequency with streamwise position for three cooling-strip locations when $M = 0.14$: a) no cooling, b) C_1 : $x = 0.30$ and 0.34 , c) C_2 : $x = 0.34$ to 0.38 , and d) C_3 : $x = 0.38$ to 0.42 ; $F = 35 \times 10^{-6}$, $T_w/T_{ad} = 0.8$, $h_5 = 1.0 \times 10^{-3}$, and L3 ($x_\ell = 0.40$ and $x_r = 0.50$).

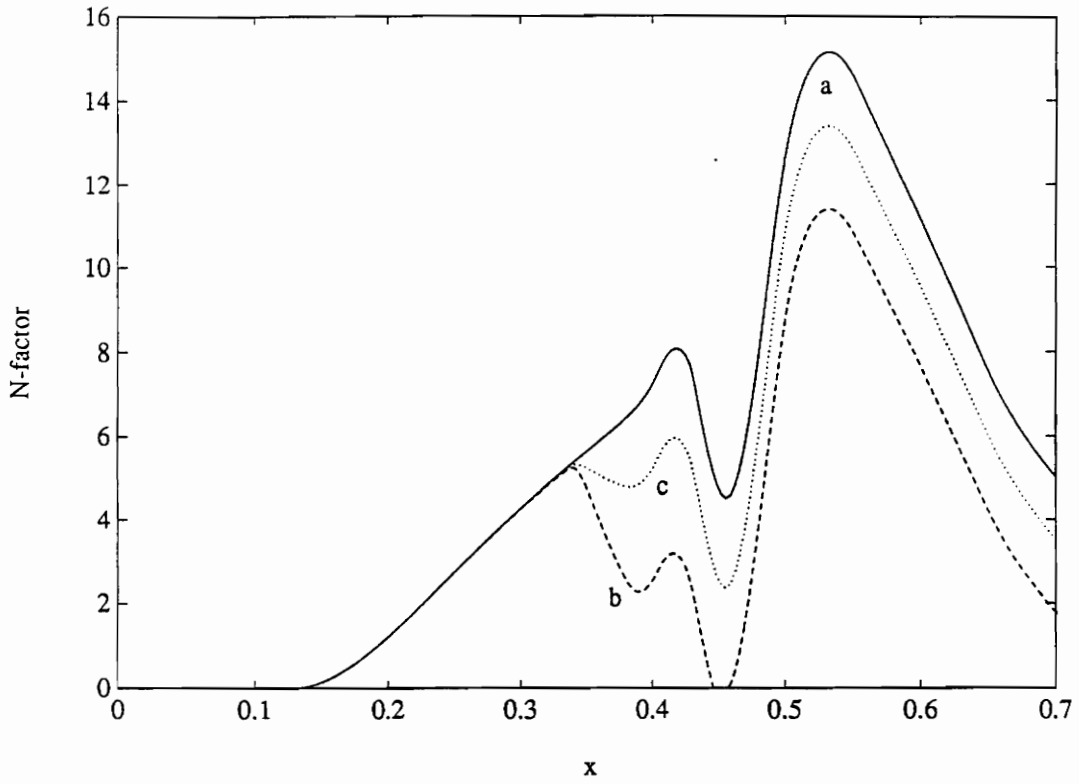


Figure 33. Variation of the N-factor for the most dangerous frequency with streamwise position for three cooling levels when $M = 0.14$: a) no cooling, b) $T_w/T_{ad} = 0.8$, and c) $T_w/T_{ad} = 0.9$; $F = 35 \times 10^{-6}$, cooling extends from $x = 0.34$ to 0.38 , $h_5 = 1.0 \times 10^{-3}$, and L3 ($x_e = 0.40$ and $x_r = 0.50$).

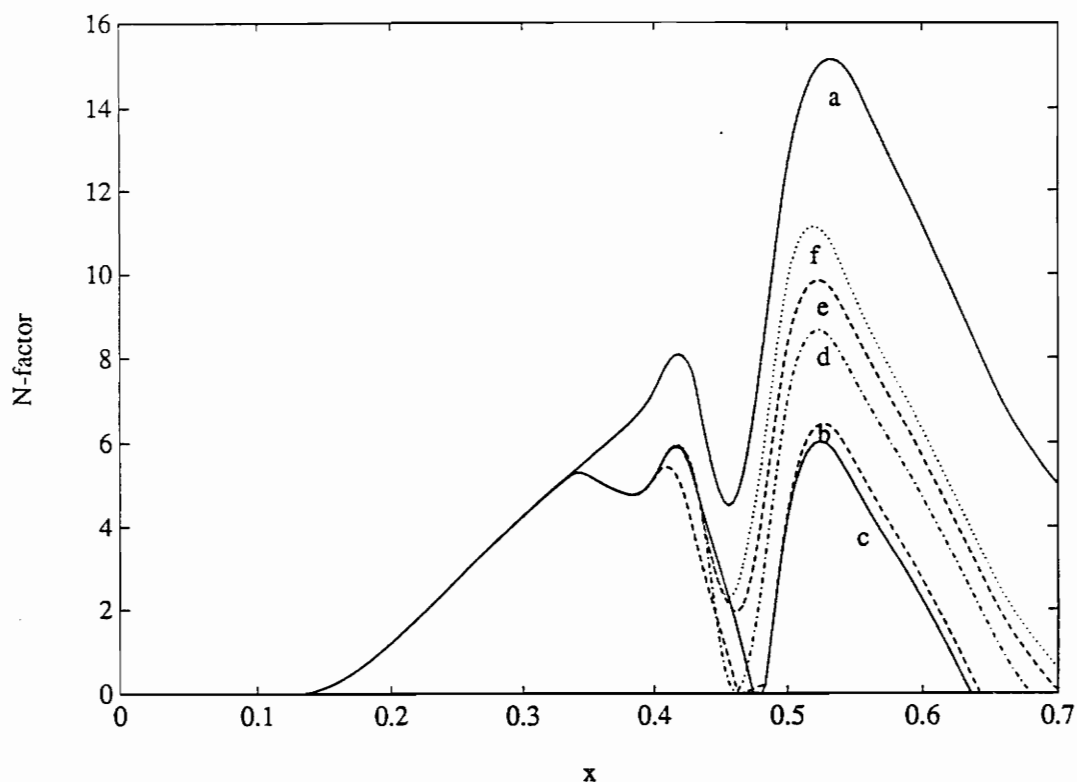


Figure 34. Variation the of N-factor with streamwise position for the most dangerous frequency and five two-cooling-strip configurations: One of the strips extends from $x = 0.34$ to $x = 0.38$ with $T_w/T_{ad} = 0.9$, and the second strip was varied but its temperature was kept at $T_w/T_{ad} = 0.80$. a) no cooling b) $C_1: x = 0.405$ to 0.445 , c) $C_2: x = 0.422$ to 0.462 , d) $C_3: x = 0.440$ to 0.480 , e) $C_4: x = 0.455$ to 0.495 , and f) $C_5: x = 0.475$ to 0.515 ; $F = 35 \times 10^{-6}$, $h_5 = 1.0 \times 10^{-3}$, $M = 0.14$, and L3 ($x_e = 0.40$ and $x_r = 0.50$).

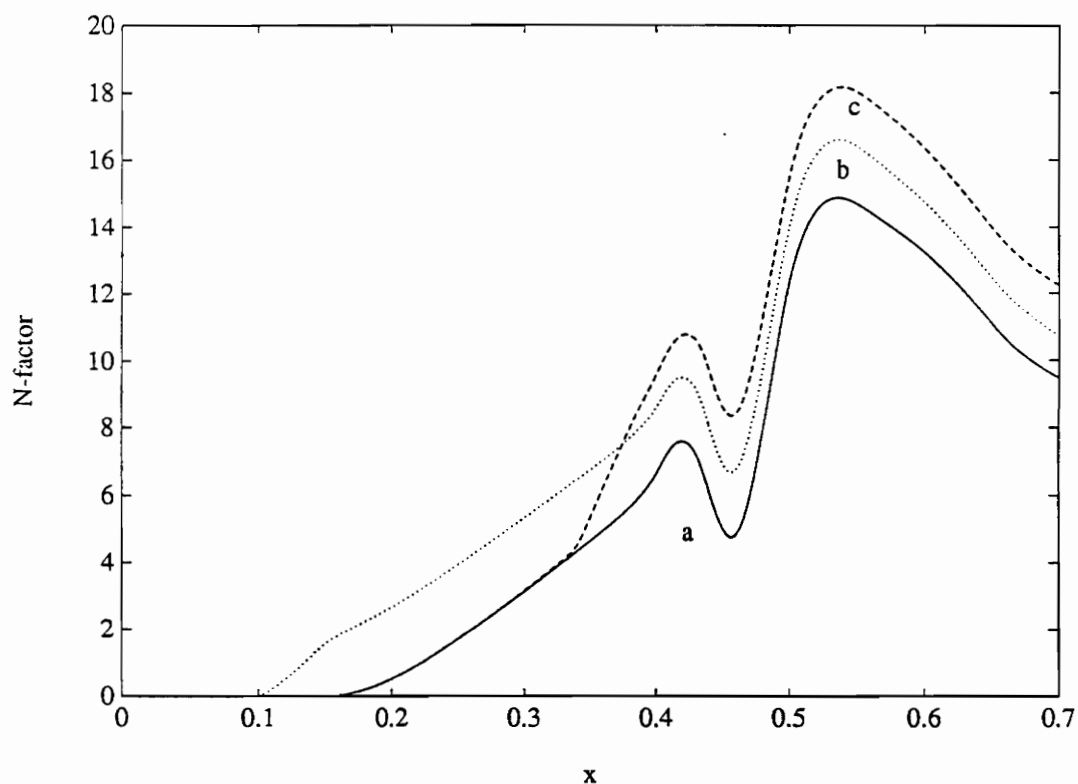


Figure 35. Variation of the N-factor for the most dangerous frequency with streamwise position for hump # 5 located at L3 and two heating strips: a) no heating, b) $x = 0.09$ to 0.140 , and c) $x = 0.34$ to 0.38 ; $F = 30 \times 10^{-6}$, $T_w/T_{ad} = 1.3$, $h_5 = 1.0 \times 10^{-3}$, $M = 0.14$, and L3 ($x_e = 0.40$ and $x_r = 0.50$).

Hasan T. Abu Khajeel was born in June 26, 1969 in Amman, Jordan. He finished his high school in June 1987. In January 1988, he came to the U.S.A.. In April 1991, he obtained his Bachelor of Science in Aeronautical Engineering from Embry-Riddle Aeronautical University in Daytona Beach, Florida. He graduated with CUM LAUDE and was first in his class. In September 1991, he joined the Department of Engineering Science and Mechanics at Virginia Polytechnic Institute and State University, and got his Master of Science in April 1993. He is a member of Sigma Gamma Tau, The National Honor Society in Aerospace Engineering. He is a member of PADI, The Open Water Diver Club and he is a student pilot for private pilot licence.

A handwritten signature in black ink, appearing to read 'HASAN', followed by a long, horizontal, wavy line that tapers to the right.